Order Number 9432366

A study of intraseasonal variability in a one-dimensional version of the Goddard atmospheric global climate model

Pabón-Ortiz, Carlos U., Ph.D.

City University of New York, 1994

U·M·I
300 N. Zeeb Rd.
Ann Arbor, MI 48106

A Study of Intraseasonal Variability in a One-Dimensional Version of the Goddard Atmospheric Global Climate Model

by

Carlos U. Pabón-Ortiz

A dissertation submitted to the Graduate Faculty in Physics
in partial fulfillment of the requirements
for the degree of Doctor of Philosophy,
The City University of New York

1994

This manuscript has been read and accepted for the
Graduate Faculty in Physics in satisfaction of the
dissertation requirement for the degree of
Doctor of Philosophy

May 4, 1994
Date

Melvin Lax
Chairman of Examining Committee

May 6, 1994
Date

Edward P. Tryon
Executive Officer

Edward Hundman
Wai Yee Ting
Chi Yuan
William Pierson
Supervisory Committee

THE CITY UNIVERSITY OF NEW YORK

Abstract

A Study of Intraseasonal Variability in a One-Dimensional Version of the Goddard Atmospheric Global Climate Model

by

Carlos U. Pabón-Ortiz

Advisers: Prof. Willard J. Pierson and Dr. William K.-M. Lau

A series of numerical experiments using the Goddard Laboratory for Atmospheres Global Climate Model (GLA-AGCM) are designed to study intraseasonal variabilities of the Madden-Julian (1972) type for an idealized tropical oceanic-atmospheric environment. A commentary on the GLA-AGCM parameterizations is presented as a means to justify the adaptation of the full three dimensional AGCM to a simpler model of a dynamically isolated vertical column. The remaining portions of the model include physical parameterizations for cumulus convection (Arakawa and Schubert, 1974), turbulent fluxes at the planetary boundary layer (Helfand and Labraga, 1988), and short and longwave radiative interactions (Harshvardhan *et al.*, 1987). The set of model experiments use prescribed values for the sea surface temperature and the upper air wind profile, over an assumed warm and uncoupled tropical ocean.

The predominant time scales and the structure of the most noticeable fluctuations are dependent on the vertically integrated water vapor mass. Under low surface evaporation, a convective fast time scale of about 42 hours dominates the lower half of the troposphere and the transport of moisture to the upper layers. This convective regime tends to be warmer and moist all through-

out, with a longer residence time. As the upper layers moisten, the absorption of shortwave radiation by water vapor aloft, and a reduced cooling due to longwave radiation emission, induce an overturning of the layers at the top of the troposphere, and a sudden transition to a colder and drier climate regime. The entire column is convectively active for a sustained period of time.

For larger amounts of precipitable water the system fluctuates non-periodically between two similarly defined regimes, but in time scales of about 20 to 60 days. In this case the drier regime has a longer residence time. A comparison of experiments with and without diurnal and seasonal solar cycles reveals that the predominant fluctuations and transitions occur even in the absence of the cyclic solar forcing. As opposed to the case of the real tropical atmosphere where moisture is provided mainly by evaporation and horizontal advection, these experiments suggest that the necessary conditions for the local enhancement of the intraseasonal variabilities are the availability of surface moisture and the residual accumulation of it in the upper troposphere.

Dedication

I dedicate this thesis presentation to my mother,

who showed me how to dream about it,

and to the Bills,

who showed me how to think about it.

Acknowledgements

The author wishes to express his gratitude to a large number of persons, whose invaluable help in unforeseen ways made this work possible. In the first place, my eternal gratitude to my mentor, Prof. Willard J. Pierson, whose tireless academic and scientific guidance opened a door for me to the atmospheric sciences. Many insightful and critical discussions with him guided this research effort to a better understanding of its implications and results. Secondly, my deepest gratitude to Dr. William K.-M. Lau, from the Laboratory for Atmospheres at NASA/Goddard Space Flight Center, whose advice on the execution of numerical modelling experiments, the analysis of data and informative discussions on tropical climate variability, illuminated my way through the development of this work. I must thank them both for their patience and support even when positive developments were not occuring at our desired pace.

The faculties of the Physics Department, the Earth and Planetary Sciences Department, and the Remote Sensing Laboratory (formerly the Institute of Marine and Atmospheric Sciences), at The City College of C.U.N.Y., helped on many an occasion whenever an answer to a problem or a question elluded me. At the Climate and Radiation Branch and at the Modeling and Simulation Branch of NASA/GSFC I held some interesting and critical discussions with Drs. Li Peng, Y. C. Sud, C.-H. Sui, and J. C. Jusem. My classmates M. Artoni, R. Blake and D. C. Ziskin provided a never faltering support, and many discussions of context and procedure. Not the least of them all, my relatives who provided accomodation and a very important moral support whenever the circumstances obliged. To all of them, and to many more anonymous hands, I convey my sincere gratitude for their kindness.

The research was financially supported by the Graduate Student Researchers Program of NASA, under grant number NGT–70098.

Contents

List of Tables

List of Illustrations

Chapter 2. Description of the GLA-AGCM

Chapter 3. The numerical experiments

Chapter 4. Spectral analysis of the time series

Chapter 5. Physical processes and the transitions between regimes

Chapter 1.

Introduction

1.0 Introduction

The purpose of this study is to identify possible mechanisms for the generation of intraseasonal variability in the convective activity in an Atmospheric Global Climate Model (refered to as AGCM). The focus of this work is in the local processes that can enhance convective activity over a simulated warm tropical oceanic area, and not on the processes induced or modified by the simulated horizontal transport of the general circulation of the atmosphere.

Some work has appeared in the literature on identifying the surface conditions for which the intraseasonal time scales of convective activity have the largest amplitudes (see for example the works of Madden and Julian, 1971; Yasunari, 1979; Hu and Randall, 1991a,b). Based on some of the ideas reported in previous investigations, in this work, the oceanic boundary serves as an infinite heat and moisture reservoir at a constant temperature of 30°C, with no momentum exchange between the atmosphere and the ocean surface. These prescriptions seem to be reasonable since the intraseasonal variability of tropical convection has been associated with warmer oceanic waters, and with fluctuations in the upper air wind, rather than with surface wind variations.

Some work has been done to identify spatial patterns and geographically localized enhancements of the intraseasonal variability (as examples, see the works of Yasunari 1979, 1980, 1981; Lau and Chan, 1985, 1986; Knutson and Weickmann, 1987; Lau and Peng, 1987; Hsu *et al.*1990). Some other modelling studies of the large scale effects that can induce intraseasonal variability have been performed to identify properties of the propagation of such waves along the tropical latitudes, but have not fully represented the propagational characteristics or the vertical structure properties of the observed intraseasonal variability. The existence of a localized enhancement, as reported in the literature, of the variability of the convective activity over the Indian and Western Pacific Oceans is a motivation for this work. In particular, the interest is in the general atmospheric conditions of moisture availability, temperature profiles, and cloud cover in such regions of the globe that might have any effect on such localized strengthening.

Some observational and modelling work over the Tropical Pacific has identified or related properties along the vertical for the tropical atmosphere with the intraseasonal time scales (see for example the works of Madden and Julian, 1971; Hayashi and Golder, 1986; Hsu *et al.*1990). The description of the vertical structure for the observed intraseasonal variability was used to focus this study on particular time scales from the output of the AGCM simulation.

Furthermore, some authors have performed observational and theoretical work to classify relationships between the radiative properties of the upper tropical troposphere and the intraseasonal time scales (see for examples the work of Lau and Chan, 1985, 1986; Weickmann *et al.*1985; Knutson and Weickmann, 1987; Lau and Peng, 1987; Anderson and Stevens, 1987). One of the purposes of this work is to clarify the general role that the radiative atmospheric interactions might have in generating this kind of variability.

It is well known that moisture convergence is an important source of water vapor for the tropical atmosphere. In this work it is assumed that a wind driven surface evaporation can provide enough moisture to maintain a convectively active atmosphere. Under such conditions, the modelled atmosphere is a simplified system that, perhaps, will not resemble the real atmosphere

very much. It is expected, although unproven, that the mechanisms generating intraseasonal variability in this limited AGCM are similar to those that serve to enhance locally the variability in these time scales in the real atmosphere if the proper conditions are set. The question to be answered is about the identification of the predominant types of variability in the absence of any lateral transport of mass, heat, moisture and momentum.

In essence, this is a study of intraseasonal variability generated within a single non-interacting column of a simulated tropical oceanic atmosphere, under the influence of parameterized sub-grid scale processes of convection, turbulence and radiative interactions.

The study is based on the use of the Goddard's Laboratory for Atmospheres Global Climate Model (refered to as GLA-AGCM). The GLA computerized model is based on a set of primitive equations in flux form for the wind components, potential temperature, specific humidity, and mass of the vertical column. To isolate the simulated atmospheric column, all references to the horizontal divergence of the wind and convergence of mass, moisture and sensible heat were supressed. Only the variations and forcing terms along the vertical direction are preserved. This model is in essence a one dimensional version (refered to as 1D), along the vertical direction, of the GLA-AGCM, over a warm oceanic area with a sea surface temperature of 30°C. The horizontal upper air winds were specified as a means of controlling the surface evaporation. For the results presented in this work only the cases for which the upper air wind was prescribed at 3.5 and 12 m/s are discussed, as they provide the most contrasting and clarifying information.

In the original three dimensional (3D) version of the GLA-AGCM many of the calculations are performed within the simulated atmospheric column. Only those that required information from neighboring grid points would imply lateral propagation of atmospheric perturbations. The modifications performed on the original 3D AGCM did not modify substantially the general logic of the model calculations for the physical forcings acting on a single column.

The GLA model includes parameterized representation of the cumulus convective activity, turbulent fluxes in the planetary boundary layer, and radiative interactions with the main gases

of the atmosphere. All these parameterizations are part of the 1D version of the GLA-AGCM, also. In a local horizontal plane, the 1D-AGCM is representative of the physical processes that can take place in one grid box of the 3D-AGCM in the absence of horizontal interactions with neighboring grid boxes. These are, in turn, intended to represent the physical processes that occur, as a spatial average, in an area several thousand square kilometers in size. The vertical direction is discretized uniformly in σ coordinates from the surface at 1010 mb to the top at 10 mb in 17 layers.

The simulations were performed with a time step of 7.5 min, for a total integration time of 1096 days. The time series for numerous variables at all layers were recorded at 1 hour intervals. Both, the resolution in time as well as the total coverage should provide for a proper representation of the phenomena associated with the scales of interest.

Spectral decomposition of subsets of the original time series were performed to identify the most relevant time scales in the series. Some of the spectral estimates are shown within the included figures.

The next section presents an introduction to the properties of this intraseasonal variability, as identified in the literature. Then a formulation of the research problem to be studied is included. Chapter 2 is a description of the hydrodynamical equations included in the original computational model, the parameterization of physical processes, the finite differences representation of the equations, and a justification of the use of a 1D-AGCM *vis a vis* the use of a more standard procedure such as a simulation with a full 3D-AGCM. Chapter 3 is a discussion of the results from the experiments. Chapter 4 is a presentation of the spectral techniques used to identify the most relevant time scales in the time series from the numerical experiments. Chapter 5 is a discussion of the possible mechanisms that can be responsible for the generation of intraseasonal variability in the 1D-AGCM. The conclusions to the work appear in Chapter 6.

1.1 Previous Work

Madden and Julian [1971] identified what they termed a 40 to 50 day oscillation, by analyzing 10 year long time series of daily rawindsonde data for wind, pressure, and temperature from Canton Island (172°W, 3°S). The oscillations they identified had the following properties: i) the spectrum of the zonal wind at 150 and 850 mb had a significant broad band peak in the 40 to 50 day range, that were out of phase with respect to each other; ii) the spectrum of the surface pressure had a peak in the same range, that was in phase with the zonal wind at 850 mb, but out of phase with the surface temperature spectrum; iii) there were no discernible signals in this frequency range for the meridional wind; iv) the phase of the temperature signals was independent of height; v) there was an annual modulation to the amplitude of the signals, with the strongest signals appearing during Winter; vi) there was a nodal surface at the 500–600 mb layer zonal wind.

There are a number of implications to the properties identified by Madden and Julian [1971]. The phase relationships between the pressure, the temperature, and the wind are typical features of the geostrophically balanced motions. The absence of a meridional component for the wave, and the low frequency of the phenomena is reminiscent of the equatorially trapped Kelvin wave as described by Holton and Lindzen [1968], Haltiner and Williams [1980], and Pedlosky [1987]. As Madden and Julian [1971] noted, there are some discrepancies between their results and the classical Kelvin wave theory, such as the lack of vertical transport of momentum, and (what was considered true at the time) the stationary nature of the wave, neither of which is a feature of the Kelvin waves as described in Pedlosky [1987]. The phase locking between the temperature and the pressure might be an indication that the wave is generated (or sustained) under barotropic conditions. It is also an indication that (as other authors have proven), if the precipitation intensifies during the passage of the propagating part of the wave, then the local convective processes play an important role in dissipating baroclinic conditions, thus suggesting the possibility that these local convective processes of very short time scale do interact with the phenomena of much longer time scales of the wave. However, it is not clear how the temperature changes on the

longer time scales of the propagating wave, in the presence of the rapid adjustments induced by the convective activity, or even, if it is the temperature field what induced the intraseasonal variability observed in other variables.

Lau and Chan [1986] were concerned with the evolution of the 40 to 50 day signal over the Indian and Western Pacific Oceans, and its relation with the Indian and Southeast Asian monsoonal regimes during the Northern Hemisphere Summer. Using daily data of the outgoing longwave radiation (OLR), for the regions of 0° to 120° W, and from 50°S to 50°N, in a grid of 5° longitude $\times$ 5° latitude resolution, they studied the empirical orthogonal functions (EOF) for the evolution of the monsoonal regime in the frequency range of 20 to 60 day. The development of the monsoonal regime started with a negative anomaly of the OLR centered on the Indian Ocean, between the Equator and the Indian subcontinent, and a delayed development of positive anomalies at the southern tip of the Indian subcontinent, and in the Western Pacific Indonesia region. Then, the negative anomaly extended longitudinally to the Western Pacific, and its center moved northward towards the Indian landmass, with the onset of the Indian Monsoon over land. The onset of the monsoon over South China, and over Southeast Asia, occurs 10 to 30 days later, and was produced by an eastward and northeastward propagation of the Indian Ocean negative OLR anomalies during the Northern Hemisphere Summer. Lau and Chan [1985] showed that the negative OLR anomalies propagate eastward and southeastward during the Northern Hemisphere Winter, concurrently with the onset of the Australian Monsoonal Season. The spatial scale of the perturbation was 6000 to 7000 km. The eastward propagation speed was 4 to 5 m/s, and the northeastward propagation speed was 1 to 2 m/s. The principal components from the EOF analysis presented characteristic time scales in the range of 30 to 60 days, although the percent variance accounted for by the largest single-point correlations is only 15%. In accordance to Lau and Chan [1985, 1986], the initial equatorial minima in the OLR was pervasive throughout the whole year (moving North or South of the equator with the location of the Summer Hemisphere). This was interpreted as an indication that the intraseasonal oscillation modulated the Indian

monsoon, but had a different origin for its preferred time scales and propagational speeds.

Another property of the intraseasonal oscillations identified by Lau and Chan [1985] was the existence of heating sources located over the Indonesian (centered about 110°E) and the Western Pacific (centered about 180°E) Equatorial waters, whose structure dominated the spatial structure of the intraseasonal variability.

The study by Knutson and Weickmann [1987] was based on a composite of several intraseasonal oscillations, that separated the events during the Northern Hemisphere Winter and Summer seasons, for a total of 6 years, from March 1979 to November 1984. Their primary data were the National Meteorological Center (NMC) analysed winds on a global grid at 250 and 850 mb, and the OLR measurements from polar orbiting satellites. The spatial resolution was 5° longitude by 5° latitude, with a time resolution of 5 day means for data reported twice a day. At each grid point, the time series were filtered from the annual and semiannual cycles. Then a band pass filter was applied to extract only the signals in the range of 30 to 60 day, and the resulting data was then used to construct contour plots of the variation of the signals as a function of longitude and time, by means of Hövmuller diagrams, for the latitude band of $\pm 5°$ about the Equator. The wind data was used to calculate the wind velocity potential, and the wind stream function from the inverse Laplacian of the divergence of the wind and the vorticity, respectively.

Knutson and Weickmann [1987] showed that there was a propagating part to the intraseasonal oscillation and a localized strenghtening (stationary part) of the upper air wind, as the wave propagated over the Indian Ocean and the Western Pacific. Knutson and Weickmann [1987] asserted that the use of the velocity potential provides a much clearer picture of the global spatial structure of the 30 to 60 day wave. The negative anomalies in the velocity potential at 250 mb, which can be used as an indication of rising air motion [Hendon, 1986; Geisler and Pitcher, 1988] propagated eastward all around the globe, but intensified over the Indian and Western Pacific Oceans. The negative anomalies in the OLR, which can be used as an indication of enhanced convective activity, propagated eastward in a much more limited domain, and were

quite strong in the equatorial Indian Ocean and the Western Pacific. The analysis of the velocity potential also showed the phase locking between the OLR anomalies and the wind at 850 mb, and the phase difference between the 250 mb and 850 mb wind signatures. However, while the wind signal traveled eastward all around the globe, the OLR signal did not generally propagate beyond the mid-Pacific Ocean (or, up to about a longitude 150°W), even during the Northern Hemisphere Winter, when the intraseasonal wave cloudiness perturbations reached its maximum extension in the tropical oceans.

Another result of the Knutson and Weickmann [1987] study was an analysis of the vertical structure of the 30 to 60 day waves in terms of the velocity potential as a function of height and longitude. They used analysed wind data from the NMC at 12 specified levels, for the latitudes of 1°S through 19°S, for a shorter period of time (December 1, 1978 thru January 31, 1979). The data were used to calculate the velocity potential without filtering the time series, as was previously done in the other parts of their study. Their results were: i) there was a vertical phase lag of about 180° between the winds at 850 mb and the winds at 150 mb; ii) the stronger anomalies in the upper air velocity potential covered the layer from 300 to 100 mb, and were more coherent than the lower level counterparts; iii) the surface layer with noticeably structured anomalies extended from 1000 to 600 mb; iv) the layer from 600 to 400 mb was a nodal surface of the velocity potential; v) the variations of the vertical structure occured on time scales of 40 to 50 days.

The last part of their study was the compositing work, to verify that the previous observations could be objectively associated to a "typical" intraseasonal oscillation. The compositing work overlapped the contour plots for the OLR and for the velocity potential from an EOF analysis to show that: i) the OLR negative anomalies (related to enhanced convective activity) large scale features appeared localized over the Indian Ocean and the Western Pacific, and some minor features appeared over Central America, the Caribbean, the Amazon forest, and Western Central Africa. The large scale features of the anomalies in the OLR and in the velocity potential

seemed to propagate eastward, while the minor features in the OLR only appeared as the sharper gradients of the velocity potential wave arrived over these regions of high surface temperature and high evaporation; ii) the large scale features of the OLR anomalies seemed to dissociate from the eastward propagating velocity potential, after the peak of the velocity potential wave left the Warm Pool region; iii) the phase locking between the OLR minima and the wind convergence (as indicated by the minima in the velocity potential anomalies), or the OLR maxima and the velocity potential maxima, was not maintained all the time, during one full cycle of the 30 to 60 day wave, but only during the passage of the wave through the Indian and Western Pacific Oceans; iv) although the minima in the OLR, during the Northern Summer, occasionally extended south of the Equator into the Indian Ocean, it was mostly constrained to a latitudinal band just north of the Equator. In contrast, the velocity potential features were of much wider range (i.e., smaller gradient), covering symetrically to the North and to the South of the Equator, but with the maxima and the minima essentially centered at the Equator; v) the Northern Winter version of the OLR broader minima extended further Eastward (i.e., beyond the dateline), and to the South of the Equator, than its Northern Summer counterpart; vi) non-Indonesian tropical convective activity (i.e., in Central America, the Amazon Forest, and Central Africa) during the passage of the velocity potential wave was broader during the Northern Winter than during Northern Summer; vii) convective acitivity concurrent with the passage of the velocity potential 30 to 60 day wave preferably occured in the Summer Hemisphere tropics, while the concurrent velocity potential anomalies in the subtropics occured in the Winter Hemisphere. Since the surface wind convergence over an oceanic tropical region implies a transport of moisture into the region, the work by Knutson and Weickmann [1987] implies that the local enhancement of the intraseasonal oscillation was accompanied by an increase in the surface moisture content, that occured simultaneously with a decrease in the OLR. But the absence of a phase lock between the OLR minima and the velocity potential minima might indicate a decoupling between the propagating and the stationary components of the intraseasonal variability. Or as Knutson and Weickmann [1987] asserted in their conclusions, the possibility of a "generation mechanism not necessarily related

to the previous oscillation [which] may often be important".

In a case study, Hsu *et al.*[1990] studied the properties of an intraseasonal disturbance, using data for the wind, the temperature, the height of the isobaric surfaces, and the vertical velocity from the European Centre for Medium Range Weather Forecast (ECMRWF) from December 1985 to January and February 1986, for a grid resolution of 5° latitude by 5° longitude, centered at the Equator, at 11 pressure levels between 50 mb and 1000 mb. In their work they constructed a set of variables representing wind components, the divergence of the wind, the velocity potential as the inverse Laplacian of the wind divergence, the stream function as the inverse Laplacian of the vertical component of the vorticity, and the vertically integrated diabatic heating. They also used the OLR as a measure of the convective activity. Hsu *et al.*[1990] also found a stationary component centered at about 120° East, longitude, and identified in terms of the strength of the OLR or the divergence of the wind at 150 mb, and an eastward propagating component.

There have been other studies of the stationary components of the intraseasonal oscillations. Hu and Randall [1991a,b] used a modified GCM from the Colorado State University, with a prescribed warm sea surface temperature and prescribed sea surface winds, a full parameterization of the radiative transfer, the Arakawa-Schubert [1974] cumulus convection parameterization, and bulk aerodynamic formulas for the latent and sensible heat fluxes from the oceanic surface, to generate intraseasonal time scale oscillations, as identified in the mean daily precipitation. The spectrum of the mean daily precipitation from their simulation showed broad band peaks centered at about 27, 35, and 70 days.

Hu and Randall's model simulations reached an equilibrium state after several hundred days. Although they do not assert such in their text, this equilibrium state was characterized by oscillations between two regimes of similar residence time, for which the atmospheric column was, alternatively, dryer and cooler, or more moist and warm. The largest perturbations in the moisture occured in the 5–6 km layer and propagated from the top down. In their simulations, the strong convective activity occured when the upper levels were warming and moistening, and

the lower levels were cooling and drying. They observed that the convective activity was weaker when the upper levels were cooling and drying, but that, as the moisture was accumulated in the lower levels, convection was triggered to return stability to the full column. Hu and Randall [1991a] stated that warmer sea surface temperatures induced more intense oscillations, but they did not present any evidence of the changes of the spectral content of the daily precipitation as a function of the simulated sea surface temperature. The modulation of the intraseasonal oscillations was expected, as can be inferred from some of the previously cited works (i.e., the annual modulation as mentioned in Knutson and Weickmann [1987]), but not presented in their results.

Hu and Randall [1991b] interpreted their results as meaning that an enhanced lapse rate will favor a weaker radiative cooling and a reduced sensible heat loss at the surface. Their results show discrepancies with those properties of the oscillations as identified by Madden and Julian [1971] and by Hsu *et al.*[1990] concerning the phase locking in the temperature signals at all levels, and the presence of a nodal point for moisture variations at the 500–600 mb layer.

1.2 Climatological description of the Western Pacific

To evaluate the absolute magnitude of the numerical results it is convenient to describe briefly the climatology of the equatorial Western Pacific in terms of the sea surface temperature, the precipitation, the surface evaporation, and the radiative fluxes at the surface. This climatological description focuses on the equatorial Western Pacific because it is the region identified in the literature where the intraseasonal variability of convective activity shows the strongest localized enhancements, or "stationary components".

The physical oceanography text by Neumann and Pierson [1966] show on figs. 14.7 and 14.8 maps for the average surface temperatures of the oceans during the months of February and August, respectively, as representative of the Northern Hemisphere's Winter and Summer seasons. The area enclosed between 140 to 160° E of longitude, and 5°S to 5°N of latitude, has temperatures above 28°C in both maps. The annual variation of the surface temperature

can be obtained from Levitus [1984], who shows that the surface temperatures in such region have a variation of less than 1°C all year around. The same cannot be said of the deep ocean temperatures for such regions, which according to Levitus [1984] can have changes as large as 2°C at a depth of 100m throughout the year. Peixoto and Oort [1992] quote values for $\sqrt{\overline{(T')^2}}$ of 2 to 3°C and 0.25 to 0.50°C, at 150m and 500m of depth, respectively, for an oceanic point at the Equator and 150E of longitude. Peixoto and Oort [1992] state that at the surface, the variation in the temperature is less than 1°C for seasonal and intraseasonal variations (see their figs. 8.6a,b,c). The variability in the sea surface temperature along the Equator for other longitudes can be much larger, as it happens, for example, in the Western Coast of South America. The constancy in the Western Pacific surface temperatures might be sustained by convergence of warm surface waters, but the variations in the deep sea waters at the same geographical locations might be induced by seasonal variations of the converging surface currents, which in turn can induce changes in the depth of the thermocline.

Although the geographical region enclosed within 140 to 160E of longitude, and 5S to 5N of latitude, does include a large number of small islands, the variability in the precipitation records is noticeable. Riehl [1954] describes on his figs. 3.1 and 3.2 the zonal mean annual precipitation rates. In the latitude bands of 0 to 5S, and 0 to 5N, the annual rainfall estimates are 150 to 167, and 167 to 183 cm/year, respectively. At the equatorial point of 150E, the precipitation rate is in the range of 200 to 300 cm/year. Riehl [1954] describe in his fig. 3.15 the variability in the precipitation at the equatorial location mentioned before as about 25% of the mean. Riehl [1954] identifies that a large fraction of the total precipitation at the equatorial trough occur during intense events, rather than during a sustained rainy period. These events can be associated to the passage of wind anomalies that intensify wind convergence (and consequently, the horizontal transport of moisture). The work by Palmer [1952] relates wind convergence and the constancy of the winds with the precipitation during some individual events. Furthermore, Riehl [1954] describes (p. 85) the seasonal variability of the upper tropospheric winds: unsteadiness in Summer

and greater constancy in Winter, for the Western Pacific. As mentioned before, the intraseasonal variability of the Madden and Julian [1972] type is stronger during the Northern Hemisphere Winter, which may be related to the steadiness of the upper air wind during that season of the year.

There are several ways in which an increasing wind speed can enhance the provision of moisture to a particular region. One of them is a ventilation effect, which in turn can be enhanced in two ways: one is an aeration effect, and secondly, by increasing the choppiness of the oceanic surface and the generation of ocean spray. In addition to ventilation effects, there are convergence effects that induce lifting or vertical motion, and the nonlinear interactions between the mean wind and the gradient terms of the wind anomalies. The current treatment can only include the "aeration" and the mean-wind-eddy-interaction effects.

Because of their observational nature, the works of Riehl [1954] and Palmer [1952] were unable to consider the effects of a weak but steady wind convergence, or of a constant horizontal wind, capable of maintaining a supply of water vapor to a particular region, that is disrupted by the passage of a disturbance in the divergence field. The disturbance might trigger a precipitation event. At least, the work by Lau and Peng [1987] mentioned above, treated in part the problem of the wind convergence effects in the generation of intraseasonal variability. The question arise as to possibility of other mechanisms for the triggering of the precipitation events.

Peixoto and Oort [1992] quote the work included in the atlas by Baumgartner and Reichel [1975] to describe the surface evaporation. These are estimates of the surface evaporation, rather than measurements of the surface fluxes. At the equatorial location of 150E, they estimate the evaporation as 120 cm/year. In the latitude bands of 10° North and South of the Equator they estimate that the yearly evaporation to precipitation ratio are 0.66 and 0.96, respectively. Using these numbers, the annual precipitation estimates are about 130 and 180 cm/year, for the 10° latitude bands North and South of the Equator. These are within the estimates of the variability for the precipitation mentioned before, and would imply a mean surface evaporation rate of 3.3

mm/day throughout the year.

The book by Parker [1988] includes a chart (p. 57) of the insolation at the top of the atmosphere as a function of latitude and time of the year. At the equatorial belt of 10°S to 10°N, the total insolation per day is in the range of 31.3 to 37.6 MJ/m^2/day throughout the year. The seasonal anomalies from the total global annual insolation are on the range of 0 to 210 MJ/m^2/month (Parker, 1988, p.59) for the same latitude belt, from which an estimate of the upper bound for the daily surplus of solar energy at the equatorial latitudes of the Western Pacific is about 7 MJ/m^2/day. This is an estimate of the extra radiative energy received by these tropical locations (when compared to the rest of the globe) at the top of the atmosphere. In the absence of atmospheric absorption, if all the energy arriving at the top of the atmosphere were used to warm up and evaporate the surface waters currently at 30°C, over 13 mm of water would evaporate each day at these latitudes. Typical estimates (Vonder Haar in Parker, 1988) are that, globally averaged, some 24% of the insolation is backscattered to space by clouds and some 6% by reflection from the different earth surfaces, and that only about 53% is absorbed at the surface (mainly the oceans), while some 17% is absorbed by clouds and the atmosphere. But, because of the enhanced cloudiness over the tropical oceans, only about 1/5 of that amount of water (or 2.6 mm/day) would evaporate from the Western Pacific if all the solar energy absorbed at the surface is used to evaporate water.

Vonder Haar in Parker [1988] also provides global estimates of the long wave radiative emissions to space. As a fraction of the insolation, some 13% of the surface thermal emissions goes directly out to space, while 87% of the surface thermal emissions are absorbed by the atmosphere. The atmosphere itself emits in all directions, with some 76% towards the surface, and 57% out to space. Finally, the surface transfers to the atmosphere some 29% in sensible and latent heat. A word of caution is to be included with these global estimates as fractions of the insolation at the top of the atmosphere, when applied to specific latitude bands. In particular, for the tropics, because of the enhanced water vapor profile, the absorption of thermal surface

radiation by the atmosphere might be higher, as well as the fractions of sensible and latent heat transfered.

1.3 The Definition of the Problem

As described in the previous paragraphs, there is a definite possibility that the intraseasonal variability discovered by Madden and Julian [1971] has both a propagating and a stationary component. The propagating component appears in terms of the fluctuations in the upper air zonal wind (and its related quantities, the velocity potential and the streamfunction). The propagating wave is either non-dissipative or there are some still unknown mechanisms that can enhance the wave throughout its global propagation. The stationary component over the Indian and Western Pacific Oceans appears in the fluctuations in the precipitation, the vertically coherent temperature fluctuations that were out of phase with the local fluctuations in the pressure near the surface, by fluctuations in the upper level cloudiness, and by fluctuations in the radiative properties of the local atmosphere. This stationary component, or localized strengthening of the intraseasonal variability, occured under suitable local conditions of moisture availability and surface temperature. The OLR wave amplitude intensified more as it traversed the Indian and Western Pacific Oceans, whose surface waters have a temperature above 27°C (between 60°E and 180°E of longitude, and $\pm 5°$ of latitude about the Equator), than what it intensified as the wave propagated over the colder waters of the Eastern Pacific or the Atlantic Oceans. This underlines the importance of the locally enhanced convective processes.

The physical variables undergoing intraseasonal variability are related to the convective activity: that is, to the processing of the available moisture within a vertical column of the atmosphere. However, convection is also the vertical motion of air masses as induced by thermal differences of contiguous layers, if these differences imply an unstable temperature lapse rate. What is peculiar of the Madden-Julian oscillations is the vertically coherent character of the fluctuations in the temperature. It can be questioned whether the fluctuations in the precipitation, in the cloudiness, and in the OLR are a response to localized intraseasonal fluctuations

in the temperature. These fluctuations in the temperature could be induced by the exchange of latent heat, by radiative heating or cooling, by sensible heat transfer, and by adiabatic expansion or compression.

One of the purposes of this study is to identify some of the mechanisms that can generate stationary intraseasonal variability in the atmospheric temperature for a tropical ocean-atmosphere environment.

Hence, a study of the stationary character of the intraseasonal variability, or even, of the possibility of generating such time scales within a single column of the atmosphere, would require the use of the temperature and the moisture as variables, as well as the corresponding forcing terms for each one of these variables. The model used to study the generation of the intraseasonal variability must include a representation of cumulus convection, of the water vapor and heat fluxes at the lower boundary, and of the radiative interactions with the main atmospheric gases. Each of these representations, or parameterizations of physical processes, estimate the forcing terms for the thermodynamic and moisture equations. Normally, an atmospheric model would also include a description of the horizontal transport (i.e., advection) of mass by the divergent wind, a subject that is discussed later.

The Goddard Laboratory for Atmospheres's Global Climate Model (AGCM) is a well documented modular computational program designed for weather and climate studies. The original version is a finite differences representation of the primitive equations of atmospheric motions (see section 2.1) with an implementation of the Arakawa and Schubert [1974] parameterization of cumulus convection (see section 2.2.1), the Helfand and Labraga [1988] parameterization of the turbulent transport of heat and momentum at the planetary boundary layer (see section 2.2.2), and the radiation codes of Harshvardhan and Corsetti [1984] for the radiative interactions with the main atmospheric gases (see sections 2.2.4 and 2.2.5).

Since the localized strengthening in the precipitation and cloudiness has been linked to warm oceanic waters, it is natural to consider that an enhanced moisture source over the warm waters

might be related to the occurance of these time scales. This study will consider an adjustable surface evaporation as one of the control parameters.

Lau and Chan [1985] mentioned the possibility that the sea surface temperature anomaly and the large-scale circulation could enter into a feedback loop that results in an enhanced convective activity. One could consider three known sources of water vapor in an atmospheric column: the surface evaporation, the evaporation of falling raindrops and the horizontal mass convergence. The surface evaporation is a function of the horizontal wind speed and of the deficit in specific humidity at the surface layer (when compared to the saturation value; see section 2.2.2). Since the saturation specific humidity is a function of temperature, then the surface evaporation is an implicit function of the two prognostic variables selected for the model. The control parameter for the evaporation is the surface wind speed. The evaporation of falling raindrops is treated inside the cumulus parameterization of the GLA-AGCM (see section 2.2.1). The wind divergence and the advection terms are the means by which a column interacts with neighboring columns. However, one of the objectives of this work is to study the generation of intraseasonal variability in the absence of propagating waves that can enhance or diffuse local responses. Several conceptual pathways could be considered:

(1) To use an isolated non-advected simulated column of the atmosphere, with an arbitrarily prescribed horizontal wind speed. The problem arises on the feasibility of the time series as describing real atmospheric phenomena.

(2) To use an isolated column with an arbitrarily prescribed wind divergence field that brings an extra amount of moisture into the column. A problem arises because of the implied vertical velocity that mass continuity would require.

(3) To consider a "swamp" world with a longitudinally asymmetrical sea surface temperature field, and with advection as a means of grid interaction. A long term climate integration of such model with equal representation of the physical processes could be computationally more expensive than alternatives 1 or 2.

(4) To use a regular 3-dimensional run of an AGCM. Such a study would bring into the results a multiplicity of factors that would make the isolation of fundamental mechanisms quite intractable. It would also be computationally expensive.

The first approach was followed because it requires fewer arbitrary definitions, and was computationally economical (see section 2.3 for a justification).

From Madden and Julian [1971] or from Hsu *et al.*[1990] it becomes clear that the stationary component of the intraseasonal oscillations has a dominant number one wavelength for the variations in the zonal wind along the vertical for pressure levels between 1000 and 150 mb. One could use a prescribed wind profile that mimics the observed wind profile that relates the local response to the propagating wave component, in order as to prepare a more realistic simulation of the intraseasonal fluctuations. In the real atmosphere, this implies the presence of a horizontal transport of moisture by convergence of moist air at every level. The presence of the divergent wind at any grid point implies an interaction with neighboring grid points, so that the overall mass of the simulated atmosphere remains constant. As mentioned before, for a 1D model, with no horizontal interactions, the values of the wind divergence would need specification, which would in turn specify the mean vertical velocity from a continuity condition, if the model is to be self-consistent. Instead of specifying a vertical shear for the horizontal wind, a constant wind speed througout the entire simulated atmosphere will be used, with the exception of the surface wind speed. The surface wind speed will be adjusted by the surface turbulence parameterization of Helfand and Labraga [1988]. In addition, the mass of the column of air is assumed constant, although the mass of water vapor in the air is a function of time.

In the sense that the typical vertical structure of the wind and the accompanying horizontal mass transport are not included in the modeled atmosphere, any oscillation of the column will be self-activated, and the numerical experiment will test the possibility that the non-advected simulated tropical oceanic atmosphere is susceptible to the occurence of intraseasonal variability.

The amount of moisture input to the modeled atmospheric system at the surface is trans-

ported upwards by a series of exchanges between neighboring layers. These processes that "diffuse" sensible heat and moisture to the upper layers modify the current values of the moist static energy, thus inducing local instabilities, and triggering convection. In the absence of mean vertical velocities, there can be convective activity if the mass flux at the top of the PBL is appropiate, and the vertical thermal structure can sustain it; that is, if the temperature lapse rate is unstable.

Lorenz [1965] presented a qualitative description of how the atmospheric motions become unstable, or aperiodic. The idea was that: the daily rotation of the earth (at quite a fast pace) and the diurnal variation of the solar heating shifts the state of the atmosphere between dynamical regimes. The steady state motions of the general circulation or the periodic fluctuations of these atmospheric motions persist on certain dynamical regimes, but the atmosphere may jump between regimes whenever its current state is favorable to another regime. The long term variability was defined as the "sluggishness" or the persistence in one particular dynamical regime ("sluggishness" as ascribed to quantities like the midlatitudes zonally averaged zonal component of the geostrophic wind). An idea behind this thesis work is that it is possible to identify characteristic modes of intraseasonal variability in the absence of the known periodic atmospheric forcings (i.e., Coriolis, diurnal and seasonal heating), and that although there is a seasonal modulation to the intraseasonal variability (e.g., Madden and Julian, 1971; Lau and Chan, 1985,1986), the generating mechanisms are more fundamental than a response to a quasi-periodic forcing.

To summarize, the objectives of this work are:

(i) to construct a model simulation that includes a description of the principal physical processes related to the input of moisture to the atmosphere, and to the local variations in the atmospheric temperature, variations which seem to be strongly related to the stationary component of the intraseasonal fluctuations under study;

(ii) to describe the convective processes that contribute to the intraseasonal variability of the precipitation patterns observed over broad tropical domains;

(iii) to identify the principal modes of these intraseasonal (modelled) fluctuations;

(iv) to identify the physical processes that contribute to the local generation of intraseasonal time scales phenomena.

Chapter 2.

Description of the GLA-AGCM

2.1.0 Hydrodynamics

This section presents briefly the general form of the equations used in the model and the notation for the variables. The following subsections describe the equations, and some of the scaling analysis used to simplify the set of equations for the prognostic variables. Then, a presentation of the finite difference form of the equations follow. The section on "Physical Parameterizations" describe the individual forcing terms related to the subgrid processes of convection, turbulence, and radiative interactions. The final section of this chapter is a discussion of the validity of using a one dimensional (1-D) reduction of the three dimensional (3-D) version of the Goddard's Laboratory for Atmospheres (GLA) Atmospheric Global Climate Model (AGCM) for a long term climate simulation.

The prognostic variables used to describe the state of the model atmosphere are: (u, v, w), the zonal, meridional and vertical components of the wind velocity, respectively; θ, the potential temperature; q, the specific humidity (or, mass of water vapor per unit mass of air); Π, the pressure difference between the top and the bottom of the model atmosphere. In general, each of the prognostic variables is a function of position (i.e., the triad x, y, z) and time, t. A complete

specification of the problem requires, at least, six equations in the six unknowns.

The equations for the wind components can be obtained from modified versions of the fluid dynamics equations for a spherical geometry in a rotating reference frame. To describe the local changes in the components of the wind velocity, $\vec{u} = (u, v, w)$, the equation has the following general form,

$$\frac{\partial \vec{u}}{\partial t} = \delta\vec{U}_{adv} + \delta\vec{U}_{press} + \delta\vec{U}_{grav} + \delta\vec{U}_{Cor} + \delta\vec{U}_{centr} + \delta\vec{U}_{turb} + \delta\vec{U}_{geom} \qquad (2.1)$$

The forcing terms, $\delta\vec{U}$, represent the advection, the pressure gradient force, the gravitational force, the Coriolis effect, the centrifugal force, the turbulence effects, and the geometrical terms. Each one of the forcing terms, $\delta\vec{U}$, will be examined in the following subsections.

The first law of thermodynamics is used to describe the local changes in the temperature. These changes can be related, in turn, to the local changes in the potential temperature.

$$\frac{\partial T}{\partial t} = \delta T_{adv} + \delta T_{moist} + \delta T_{turb} + \delta T_{rad}. \qquad (2.2)$$

Here the terms δT represent the advective effects, latent heat release, turbulence effects, and radiative heating.

The local changes in the specific humidity are described by a conservation law for water vapor,

$$\frac{\partial q}{\partial t} = \delta q_{adv} + \delta q_{moist} + \delta q_{turb}. \qquad (2.3)$$

where the different δq terms represent the advective effects, the combined effects of condensation and evaporation, and turbulence effects.

Let $p = p(x, y, z, t)$ be the pressure at any given point and time. Following Arakawa and Suarez [1983], the pressure difference between the top and the bottom of the simulated atmosphere, $\Pi = p_s(x, y, t) - p_t$, can be related to the mass of air over a unit surface area for an atmospheric column. Here p_t is the pressure at the top of the simulated atmosphere and p_s the surface pressure. If the vertical and horizontal variations in the pressure can be decoupled, then,

$$p(x, y, z, t) = \Pi(x, y, t)\sigma(z) + p_t. \qquad (2.4)$$

where σ varies between 0 and 1, from the top to the bottom, respectively. Under environmental hydrostatic conditions, the pressure variations, δp, perceived by an air parcel during an adiabatic ascending displacement, δz, are described as,

$$\delta p = -\rho g \delta z. \tag{2.5}$$

where ρ is the density of air, and g is the gravitational constant. From the previous definition of $p(x, y, z, t)$ in terms of Π and σ, the δp can also be expressed as

$$\delta p = \Pi \delta \sigma$$

if the top model pressure, p_t, is assumed constant. Hence, for an upward displacement under hydrostatic conditions it can be stated that,

$$\Pi \delta \sigma = -\rho g \delta z. \tag{2.6}$$

An integration throughout the vertical column will give the mass areal density on the right hand side of the following expression:

$$\frac{\Pi}{g} \int_0^1 d\sigma = \int_{bottom}^{top} \rho dz$$

Thus, Π/g represents the mass of air over a unit area of a column in the model atmosphere. Local changes in the quantity Π/g will represent net mass changes in the column. Conversely, the continuity equation can be used to describe changes in the density of mass at a given point; namely,

$$\frac{\partial \rho}{\partial t} + \nabla \cdot (\rho \vec{u}) = 0. \tag{2.7}$$

which can be transformed to describe local changes in the column,

$$\frac{\partial \Pi}{\partial t} + \frac{\partial (\Pi u)}{\partial x} + \frac{\partial (\Pi v)}{\partial y} + \frac{\partial (\Pi \dot{\sigma})}{\partial \sigma} = 0$$

Here, $\dot{\sigma} = d\sigma/dt$ is called the sigma velocity.

Hence, nominally, a set of six equations in six unknowns describes the state of the model atmosphere. As will be seen, the problem becomes more complex than the previous set of

equations suggests because: (i) a scale analysis of some of the terms in the equations might decouple the prognostic variable set; (ii) the complete specification of the individual forcing terms is non-trivial, since the sub-grid scale processes naturally interact with the large scale environment; (iii) the boundary conditions at the surface are not fixed in time, but can rather alter, as an example, the water vapor content of the model atmosphere.

2.1.1 The Conservation of Mass

Suppose a differential volume element, $\delta^3 x$, that has an air mass density, ρ. The mass density flux out of this volume element is $\rho\vec{u}$. The equation of continuity (Equation (2.7)) relates the local changes in the mass density to the mass density flux through the boundaries of the volume being considered,

$$\frac{\partial \rho}{\partial t} + \nabla \cdot (\rho \vec{u}) = 0$$

where, $\nabla = \hat{x}\partial/\partial x + \hat{y}\partial/\partial y + \hat{z}\partial/\partial z$. Here, an inward mass density flux could imply convergence of the mass density flux vector. This equation must be rewritten in σ coordinates.

For a mass element $\rho\delta^3 x$ in motion, mass continuity implies that the mass inside the volume does not change following its motion,

$$\frac{d}{dt}\left(\rho\delta^3 x\right) = 0. \tag{2.8}$$

In Cartesian coordinates, the total time derivative is expressed as, $d/dt = \partial/\partial t + \vec{u} \cdot \nabla$. The total time derivative of a scalar quantity is the rate of change of that quantity as perceived when following the motion. Suppose that a parcel of air moves through an environment with a characteristic property $Q = Q(x, y, z, t)$. As the parcel of air moves through with a velocity $\vec{u}$, local changes in Q are induced by local sources, plus those changes induced by the fact that $\nabla Q \neq 0$. This last type of perceived changes is proportional to the scalar product between the gradient in Q and the velocity of the air parcel, $\vec{u} \cdot \nabla Q$. The hydrostatic equation, $\delta p = -\rho g \delta z$, can be used to eliminate the dependence on ρ, so that the continuity equation appears as,

$$\frac{d}{dt}\left(\delta x \delta y \frac{\delta p}{g}\right) = 0$$

which, per unit volume and constant g, translates to,

$$\rho\left(\frac{\partial u}{\partial x}+\frac{\partial v}{\partial y}+\frac{\partial \omega}{\partial p}\right)=0. \tag{2.9}$$

$$\omega \equiv \frac{dp}{dt}. \tag{2.10}$$

These two equations describe the conservation of mass in the isobaric coordinate system. By using this formulation for the conservation of the mass of air and with a conservation law for the specific humidity, the model will contain a mass conservation rule for two of the major constituent gases in the atmosphere. These aspects of the conservation of mass and moisture are discussed in the subsections for the conservation of moisture and the cumulus parameterization.

The transformation to the σ coordinate system must take into account the fact that the horizontal gradient of Q with constant p, $\nabla_p Q$, or the gradient with constant σ, $\nabla_\sigma Q$, might not be parallel in both systems. In general, following the work of Arakawa and Suarez [1983] let

$$\nabla_p Q = \nabla_\sigma Q + (\nabla_p \sigma)\frac{\partial Q}{\partial \sigma}. \tag{2.11}$$

The horizontal gradients, ∇_p and ∇_σ, are defined as,

$$\nabla_p \equiv \left(\hat{x}\frac{\partial}{\partial x}+\hat{y}\frac{\partial}{\partial y}\right)\Bigg|_p$$

$$\nabla_\sigma \equiv \left(\hat{x}\frac{\partial}{\partial x}+\hat{y}\frac{\partial}{\partial y}\right)\Bigg|_\sigma$$

From the definition of the σ coordinates (Equation (2.4)), and since $\nabla_p p \equiv 0$, it is easy to see that,

$$\sigma\nabla_p \Pi + \Pi\nabla_p\sigma = 0. \tag{2.12}$$

Hence, the two operators ∇_p and ∇_σ are related by

$$\nabla_p = \nabla_\sigma - \frac{\sigma}{\Pi}(\nabla_\sigma \Pi)\frac{\partial}{\partial \sigma}. \tag{2.13}$$

The vertical velocity, ω, from Equation (2.10) can be redefined as

$$\omega = \sigma\left(\frac{\partial \Pi}{\partial t}+\vec{u}\cdot\nabla_\sigma\Pi\right)+\Pi\dot{\sigma}. \tag{2.14}$$

where $\dot{\sigma} \equiv d\sigma/dt$. Since

$$\frac{\partial \omega}{\partial \sigma} = \frac{\partial \Pi}{\partial t} + \vec{u} \cdot \nabla_\sigma \Pi + \frac{\partial (\Pi \dot{\sigma})}{\partial \sigma} + \sigma \frac{\partial \vec{u}}{\partial \sigma} \cdot \nabla_\sigma \Pi. \tag{2.15}$$

and using the relation between the operators (Equation (2.13)) into the isobaric form of the continuity equation (Equation (2.9)),

$$\nabla_p \cdot \vec{u} + \frac{\partial \omega}{\partial p} = \nabla_\sigma \cdot \vec{u} - \frac{\sigma}{\Pi} \left(\frac{\partial \vec{u}}{\partial \sigma} \right) \cdot \nabla_\sigma \Pi + \frac{\partial \omega}{\partial \sigma} \frac{\partial \sigma}{\partial p}. \tag{2.16}$$

A combination of these two equations yields,

$$\frac{\partial \Pi}{\partial t} + \nabla_\sigma \cdot (\Pi \vec{u}) + \frac{\partial (\Pi \dot{\sigma})}{\partial \sigma} = 0. \tag{2.17}$$

This is the continuity equation in σ coordinates.

Since Π can be related to the weight per unit area of the column of air above the surface, this form of the continuity equation relates local changes in the mass of the column to mass transport into the column through the lateral boundaries (i.e., convergence of air masses), and to mass exchange between neighboring layers. The vertical mass exchange caused by thermal differences between layers and by the exchange of latent heat due to moist processes is called convection.

An indefinite integration of the continuity equation in σ coordinates (Equation (2.17)), from the top down to layer σ, and since $\partial \Pi / \partial \sigma = 0$, yields,

$$\Pi \dot{\sigma} \Big|_0^\sigma = - \int_0^\sigma d\sigma \left[\frac{\partial \Pi}{\partial t} + \nabla_\sigma \cdot (\Pi \vec{u}) \right]$$

Also, an integration from the top to the bottom yields,

$$\frac{\partial \Pi}{\partial t} = \Pi \dot{\sigma} \Big|_{top} - \int_0^1 d\sigma \nabla_\sigma \cdot (\Pi \vec{u}). \tag{2.18}$$

if $\dot{\sigma} \mid_{\sigma=1} = 0$. That is, for a hydrostatic atmosphere and in the absence of local mass sources, the net lateral convergence of air mass through the sides of the column is balanced by the mass flux at the top boundary.

2.1.2 The Equations of Fluid Dynamics

The equations for the wind velocity in Cartesian coordinates, $\vec{u} = (u, v, w)$, can be written as,

$$\frac{\partial \vec{u}}{\partial t} = \delta\vec{U}_{adv} + \delta\vec{U}_{press} + \delta\vec{U}_{grav} + \delta\vec{U}_{Cor} + \delta\vec{U}_{centr} + \delta\vec{U}_{turb}. \tag{2.19}$$

where the forcing terms, $\delta\vec{U}$, represent the advection, the pressure gradient force, the gravitational force, the Coriolis and centrifugal effects, and the turbulence effects. The expression for the conservation of mass (Equation (2.17)),

$$\frac{\partial \Pi}{\partial t} + \frac{\partial(\Pi u)}{\partial x} + \frac{\partial(\Pi v)}{\partial y} + \frac{\partial(\Pi \dot{\sigma})}{\partial \sigma} = 0$$

can be used to get an expression for the fluid dynamics equations in σ coordinates.

The total time derivative in σ coordinates is expressed as,

$$\frac{d}{dt} = \frac{\partial}{\partial t} + \vec{u} \cdot \nabla_\sigma + \dot{\sigma}\frac{\partial}{\partial \sigma}$$

Then, the time derivative for $\vec{u}$ is

$$\frac{d\vec{u}}{dt} = \frac{\partial \vec{u}}{\partial t} + u\frac{\partial \vec{u}}{\partial x} + v\frac{\partial \vec{u}}{\partial y} + \dot{\sigma}\frac{\partial \vec{u}}{\partial \sigma}. \tag{2.20}$$

If Equation (2.20)is multiplied by Π and is added to the continuity expression, Equation (2.17), multiplied by $\vec{u}$, then the result is,

$$\Pi\frac{d\vec{u}}{dt} = \frac{\partial(\Pi\vec{u})}{\partial t} + \frac{\partial(\Pi u\vec{u})}{\partial x} + \frac{\partial(\Pi v\vec{u})}{\partial y} + \frac{\partial(\Pi\dot{\sigma}\vec{u})}{\partial \sigma}. \tag{2.21}$$

This is the flux form for the total time derivative of the wind velocity.

The specific form for some of the forcing terms, $\delta\vec{U}$, follow. The advective term from the previous equation is given by,

$$\Pi\delta\vec{U}_{adv} = -\frac{\partial(\Pi u\vec{u})}{\partial x} - \frac{\partial(\Pi v\vec{u})}{\partial y} - \frac{\partial(\Pi\dot{\sigma}\vec{u})}{\partial \sigma}. \tag{2.22}$$

The pressure gradient force can be expressed in terms of the geopotential, Φ. The pressure gradient term in Cartesian coordinates is given by $\delta\vec{U}_{press} = -\alpha\nabla p$, where α is the **specific volume** of air, and $p = p(x, y, z, t)$ is the pressure. The use of the relation between the operators ∇_p and ∇_σ, Equation (2.13), and the definition of the geopotential function as $\delta\Phi = -\alpha\delta p$ yields the pressure gradient force expressed as,

$$\nabla_p\Phi = \nabla_\sigma\Phi - \frac{\sigma}{\Pi}(\nabla_\sigma\Pi)\frac{\partial\Phi}{\partial\sigma}$$

or as,

$$\Pi\nabla_p\Phi = \nabla_\sigma(\Pi\Phi) - \frac{\partial(\sigma\Phi\nabla_\sigma\Pi)}{\partial\sigma}. \tag{2.23}$$

The expression for the pressure gradient force becomes,

$$\Pi\delta\vec{U}_{press} = -\nabla_\sigma(\Pi\Phi) + \frac{\partial(\sigma\Phi\nabla_\sigma\Pi)}{\partial\sigma} + \hat{z}\Pi g. \tag{2.24}$$

The gravitational force on an air mass element $\rho\delta^3x$ can be expressed as,

$$-\frac{GM_e}{r^2}\rho\delta^3x$$

where G is the universal gravitational constant, M_e is the mass of the Earth, and r is the distance between the center of the Earth and the position of the volume δ^3x. The negative sign indicates the attractive nature of the force, in the direction of an imaginary line between the two objects. The portion of interest of the lowest atmosphere (i.e., the troposphere) has a thickness $H \sim 2.0 \times 10^4$ m, which is much smaller than the mean radius of the Earth, $a = 6.37 \times 10^6$ m. Then, for any parcel of air at a height z within that vertical domain and for a spherical Earth surface, the gravitational force can be approximated by,

$$-(\rho\delta^3x)\frac{GM_e}{a^2}(1 - 2z/a). \tag{2.25}$$

where the error of the approximation, by excluding the $2z/a$ term is about 0.3%.

According to the *Smithsonian Meteorological Tables* (List, 1984), the acceleration of gravity can be represented as a function of latitude as,

$$g_\phi = 9.780356(1.0 + 0.0052885 \sin^2 \phi - 0.0000059 \sin^2 2\phi)$$

With an error of less than 1% to account for height and latitude effects, and for the kind of motions of meteorological interest in this work, $\Pi \delta \vec{U}_{grav} = -\hat{z} \Pi g$.

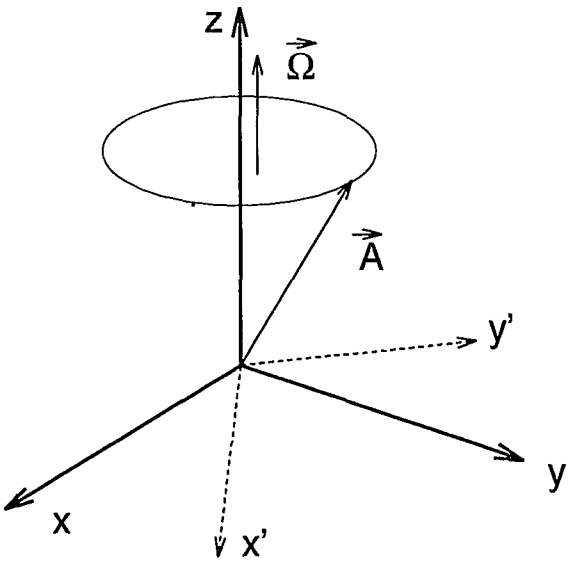

Figure 2.1 – Constant vector in a rotating coordinate system. The vector $\vec{A}$ is constant with respect to the coordinate system $\mathcal{S}'$, but rotates with an angular velocity $\vec{\Omega}$ with respect to the coordinate system $\mathcal{S}$.

The Coriolis and centrifugal effects are due to the non-inertial reference frame induced by the rotation of the Earth. Suppose two Cartesian reference frames, $\mathcal{S}$ and $\mathcal{S}'$, with a common origin, as is shown in Fig. 2.1. The reference frame $\mathcal{S}'$ rotates at a constant angular velocity, $\vec{\Omega}$, with respect to the frame $\mathcal{S}$. The position of a particle is defined by the same vector $\vec{r}$ in both $\mathcal{S}$ and $\mathcal{S}'$. The velocity of the particle, at position $\vec{r}$, in motion relative to $\mathcal{S}'$, when measured in $\mathcal{S}$ is given by,

$$\left.\frac{d\vec{r}}{dt}\right|_{\mathcal{S}} = \left.\frac{d\vec{r}}{dt}\right|_{\mathcal{S}'} + \vec{\Omega} \times \vec{r}$$

where the vector $\vec{\Omega}$ points along the axis of the rotation, upwards for a counterclockwise rotation. Hence, the time derivative of the wind velocity vector, as measured in the $\mathcal{S}$ reference frame, will contain some extra terms due to the rotation of $\mathcal{S}'$,

$$\left.\frac{d^2\vec{r}}{dt^2}\right|_{\mathcal{S}} = \left.\frac{d^2\vec{r}}{dt^2}\right|_{\mathcal{S}'} + 2\vec{\Omega} \times \vec{U}_{\mathcal{S}'} + \vec{\Omega} \times \vec{\Omega} \times \vec{r} + \left.\frac{d\vec{\Omega}}{dt}\right|_{\mathcal{S}'} \times \vec{r}. \tag{2.26}$$

If it is assumed that the rotation of the Earth has a constant angular velocity, $\vec{\Omega}$, then the acceleration with respect to $\mathcal{S}$ is equal to the acceleration with respect to $\mathcal{S}'$ plus the two extra terms $2\vec{\Omega} \times \vec{U}_{\mathcal{S}'}$ and $\vec{\Omega} \times \vec{\Omega} \times \vec{r}$.

The first extra term is called the Coriolis force. The Coriolis force is exerted perpendicular to both, the motion of the air parcel, and to the axis of the rotation, and tends to deflect its motion always to its right (left) in the Northern (Southern) Hemisphere. The representations of $\vec{\Omega}$ and $\vec{u}$ in component form are given by $\vec{\Omega} = \Omega(0, \cos\phi, \sin\phi)$ and $\vec{u} = (u, v, w)$, where ϕ is the latitude. The components of the Coriolis effect, then, are expressed as,

$$\Pi\delta\vec{U}_{Cor} = 2\Pi\Omega(v\sin\phi - w\cos\phi, -u\sin\phi, u\cos\phi). \tag{2.27}$$

Close to the Equator $\sin\phi \approx \phi$ and $\cos\phi \approx 1$, which implies that, $\delta\vec{U}_{Cor} \simeq 2\Pi\Omega(v\phi - w, -u\phi, u)$. The numerical value of Ω is about 7.27×10^{-5} rad/sec. The typical mean vertical velocity, w, is about 1 cm/s, and the typical horizontal velocity is about 3 m/s. The Coriolis force is often represented as $\Pi\delta\vec{U}_{Cor} \simeq 2\Pi\Omega(v\phi, -u\phi, u)$ under such conditions.

The other term is the centrifugal effect, $\Pi\delta\vec{U}_{centr} = \Pi\vec{\Omega} \times \vec{\Omega} \times \vec{r}$. In the local (x, y, z) coordinate system this product appears as,

$$\Pi\delta\vec{U}_{centr} = \Omega^2 r\cos\phi\ (0, -\sin\phi, \cos\phi). \tag{2.28}$$

At low latitudes it is approximated as $\Pi\delta\vec{U}_{centr} = \Omega^2 r\ (0, -\phi, 1)$. The $\hat{z}$ component modifies the acceleration of gravity as $\hat{z} \cdot \Pi(\delta\vec{U}_{centr} + \delta\vec{U}_{grav}) = \Pi(\Omega^2 r - g)$. This is a very small correction since $\Omega^2 r/g \simeq 0.34\%$. The $\hat{y}$ component is also rather small when compared to the other terms in the meridional velocity equation.

2.1.3 The Conservation of Energy

As stated in the introductory remarks for this chapter, the first law of thermodynamics is used to account for the conservation of energy; namely,

$$\frac{\partial T}{\partial t} = \delta T_{adv} + \delta T_{moist} + \delta T_{turb} + \delta T_{rad}$$

The local changes in the temperature, T, are due to advective effects (for example, when the cool marine breeze cools off inland daytime temperatures), to latent heat exchanges during condensation or evaporation (for example, during the formation of cloud cells, or caused by the environmental subsidence of upper atmospheric dry air), to microscale turbulent transport of sensible heat, and to radiative effects, respectively. The first law of thermodynamics must be used to construct an equation for the potential temperature, θ.

The first law of thermodynamics relates the heat applied per unit mass to a system, δQ, the work done by the system per unit mass, δW (say, during an expansion), and the temperature changes, δT, as

$$c_v \delta T = \delta Q - \delta W. \tag{2.29}$$

Here c_v is the specific heat at constant volume (for dry air, $c_v = 717$ J/kg-K). For an ideal gas, the work done per unit mass during an expansion can be expressed as $\delta W = p\delta\alpha$, where α is the specific volume of the gas (i.e., $\alpha = 1/\rho$). Hence,

$$c_v \delta T = \delta Q - p\delta\alpha \qquad \text{or} \qquad (c_v + R)\delta T - \alpha\delta p = \delta Q. \tag{2.30}$$

if the ideal gas law, $p\alpha = RT$, is used. R is the universal gas constant divided by the equivalent molecular mass of air (i.e., $R = 287$ J/kg-K). The combination $c_v + R = c_p$ is called the specific heat at constant pressure. Under adiabatic conditions, $\delta Q = 0$, and the definition of the potential temperature is,

$$\theta \equiv T/P, \qquad P = (p/p_s)^{\kappa}, \qquad \kappa = R/c_p. \tag{2.31}$$

with p_s a standard reference pressure. Physically, the potential temperature would be the temperature of an air parcel if it is brought dry adiabatically to the pressure level p_s from an initial level at pressure p.

From the definition of θ it is clear that

$$c_p \delta \ln \theta = \frac{1}{T} \delta Q$$

or that

$$\frac{dQ}{dt} = c_p \frac{T}{\theta} \frac{d\theta}{dt}$$

$$\frac{dQ}{dt} = c_p \left(\frac{p}{p_s} \right)^{\kappa} \frac{d\theta}{dt}. \tag{2.32}$$

which is the first law of thermodynamics in terms of the potential temperature, for an atmosphere that behaves like an ideal gas.

Since the total time derivative of θ is expressed as

$$\frac{d\theta}{dt} = \frac{\partial \theta}{\partial t} + \vec{U} \cdot \nabla_\sigma \theta + \dot{\sigma} \frac{\partial \theta}{\partial \sigma}$$

multiplying by Π and adding to the continuity expression (Equation (2.17)) multiplied by θ, yields,

$$\frac{\partial (\Pi \theta)}{\partial t} = -\nabla_\sigma \cdot (\Pi \theta \vec{U}) - \frac{\partial (\dot{\sigma} \Pi \theta)}{\partial \sigma} + \frac{\Pi}{c_p} \left(\frac{p_s}{p} \right)^{\kappa} \left[\delta T_{moist} + \delta T_{turb} + \delta T_{rad} \right]. \tag{2.33}$$

This is the flux form of the thermodynamic equation in terms of the potential temperature.

2.1.4 The Conservation of Moisture

A conservation rule for the water substance is presented in this subsection. The real atmosphere might contain several phases of water in a given column. Some of the phases might appear in several species; say, the solid phase might appear as snow particles, hail particles, frozen rain, etcetera, with a distribution of sizes for each type. The motion inside the cloud convective cells mix the particle types allowing the growth and decay of the different species. The budgets for

these mass exchanges can be rather difficult to describe. These mass exchanges also imply energy transfers of latent heat between layers of the atmosphere. The scope of this work is more limited than the detailed description of these phase transitions and of the conservation of the water substance, this one defined as the sum of the masses in all phases and species.

For the simulations presented in this work the water substance is assumed to consist of only two phases: vapor and liquid. In a 3-D simulation, the water evaporates from the surface of the Earth and ascends to the higher levels of the atmosphere, either by turbulent transport or by means of the convective activity. There are three additional alternate paths for the vapor reaching any particular level: it can precipitate, it can be transported horizontally to neighboring grid cells by the wind, or it can remain within the layer. The horizontal or vertical transport by the wind is termed advection of the moisture. This process is of particular importance for the climate of the middle latitudes, and for the large amounts of moisture present in the atmosphere of the warmer tropical regions.

The model recognizes two types of precipitation processes: stratiform or large scale, and convective precipitation. The convective precipitation type can occur under conditions of thermal instability. It is the most effective of the precipitating process included in the model, and can account normally for 40–80% of the total precipitation.

The stratiform precipitation type can occur in the model whenever a whole layer becomes saturated. The excess water vapor is precipitated immediately to the layer below. Some evaporation of the precipitation can occur in the subsequent lower layers, and only the precipitation left after the lowest layer reaches the ground. In the real atmosphere this type of precipitation process is the longest lived, but it accounts for only a small portion of the net precipitation.

As in Haltiner and Williams [1980], the conservation of the water vapor contained in a mass element of air $\rho\delta^3 x$ can be expressed as,

$$\frac{d}{dt}\left(q\rho\delta^3 x\right) = \mathcal{S} \quad , \tag{2.34}$$

where q is the **specific humidity**, or the mass of water vapor per unit mass of air, and $\mathcal{S}$ represents the sources and sinks of water vapor per unit volume of air. The quantity ρq represents the mass of water vapor per unit volume. By means of the continuity condition (Equation (2.8)) the former expression is reduced to

$$\frac{dq}{dt} = \frac{\mathcal{S}}{\rho \delta^3 x}$$

This general conservation rule for q is written in σ coordinates as,

$$\frac{\partial q}{\partial t} + \vec{u} \cdot \nabla q + \dot{\sigma} \frac{\partial q}{\partial \sigma} = \delta q_{cond} + \delta q_{evap} + \delta q_{turb}. \tag{2.35}$$

The two terms δq_{cond} and δq_{evap} could be combined into a single term δq_{moist}, as in Equation (2.3), except at the surface boundary where it is the turbulent flux of moisture what accounts for the evaporation. The continuity equation in σ coordinates and the conservation rule for water vapor (Equation (2.35)) yield

$$\frac{\partial(\Pi q)}{\partial t} = -\nabla \cdot (\Pi \vec{u} q) - \frac{\partial(\Pi \dot{\sigma} q)}{\partial \sigma} + \delta q_{cond} + \delta q_{evap} + \delta q_{turb}. \tag{2.36}$$

The first two terms on the right represent the horizontal and vertical advection of moisture, respectively. The subsection on the Arakawa-Schubert parameterization of cumulus activity describes in more detail these physical processes. The turbulence forcing term is discussed in the subsection on the parameterization of turbulence.

2.1.5 Some Geometrical Considerations

This subsection is a discussion of the additional terms introduced in the equations of motion by the nearly spheroidal shape of the Earth's surface. The Earth has an equatorial radius of 6378.4 km and a mean polar radius of 6356.9 km, with a relative difference of 0.34% (List, 1984). To a good approximation it is sensible to use a spherical coordinate system with coordinates (λ, ϕ, r) to describe atmospheric motions. Here λ is the longitude, ϕ is the latitude, and r is the radial distance from the center of the Earth. As expressed before, it will be assumed that $r = a + z$, where a is the radius of the Earth, and z the height of a point above the surface.

The curvilinear length elements in a spherical coordinate system are given by,

$$\begin{aligned} dx_1 &= r\cos\phi\, d\lambda \\ dx_2 &= r\, d\phi \\ dx_3 &= dr = dz \end{aligned} \qquad (2.37)$$

Hence, the velocity vector is given by $\vec{u} = \hat{x} r\cos\phi\dot{\lambda} + \hat{y} r\dot{\phi} + \hat{z}\dot{z}$ in a local Cartesian coordinate system. The time derivative of the velocity is

$$\frac{d\vec{u}}{dt} = \hat{x}\frac{du}{dt} + \hat{y}\frac{dv}{dt} + \hat{z}\frac{dw}{dt} + u\frac{d\hat{x}}{dt} + v\frac{d\hat{y}}{dt} + w\frac{d\hat{z}}{dt}. \qquad (2.38)$$

The extra terms have the following form,

$$\begin{aligned} \frac{d\hat{x}}{dt} &= \hat{y}\frac{u}{r}\tan\phi - \hat{z}\frac{u}{r} \\ \frac{d\hat{y}}{dt} &= -\hat{x}\frac{u}{r}\tan\phi - \hat{z}\frac{v}{r} \\ \frac{d\hat{z}}{dt} &= \frac{1}{r}(u\hat{x} + v\hat{y}) \end{aligned}$$

Another way of expressing the component form of these time derivatives is

$$\frac{d\vec{u}}{dt} = \hat{x}\left(\frac{du}{dt} - \frac{uv}{r}\tan\phi + \frac{uw}{r}\right) + \hat{y}\left(\frac{dv}{dt} + \frac{u^2}{r}\tan\phi + \frac{vw}{r}\right) + \hat{z}\left(\frac{dw}{dt} - \frac{u^2+v^2}{r}\right). \qquad (2.39)$$

The individual terms of the form du/dt are expanded as $\frac{\partial u}{\partial t} + \vec{u}\cdot\nabla u + \dot{\sigma}\frac{\partial u}{\partial \sigma}$, if expressed in σ coordinates, and by including the forcing terms of section 2.1.2 one gets for the $\hat{x}$ component,

$$\frac{du}{dt} - \frac{u}{r\cos\phi}(v\sin\phi - w\cos\phi) = -\frac{1}{\rho}\frac{\partial p}{\partial x} + 2\Omega(v\sin\phi - w\cos\phi) + \hat{x}\cdot\delta\vec{U}_{turb}$$

This last expression is rewritten as,

$$\frac{\partial u}{\partial t} = -\vec{U}\cdot\nabla u - w\frac{\partial u}{\partial z} - \frac{1}{\rho}\frac{\partial p}{\partial x} + (2\Omega + \frac{u}{r\cos\phi})(v\sin\phi - w\cos\phi) + \hat{x}\cdot\delta\vec{U}_{turb}. \qquad (2.40)$$

Similarly, for the other components,

$$\frac{\partial v}{\partial t} = -\vec{U}\cdot\nabla v - w\frac{\partial v}{\partial z} - \frac{1}{\rho}\frac{\partial p}{\partial y} - (2\Omega + \frac{u}{r\cos\phi})u\sin\phi - \frac{vw}{r} + \hat{y}\cdot\delta\vec{U}_{turb}. \qquad (2.41)$$

$$\frac{\partial w}{\partial t} = -\vec{U}\cdot\nabla w - w\frac{\partial w}{\partial z} - \frac{1}{\rho}\frac{\partial p}{\partial z} - g + (2\Omega + \frac{u}{r\cos\phi})u\cos\phi + \frac{v^2}{r} + \hat{z}\cdot\delta\vec{U}_{turb}. \qquad (2.42)$$

Since $\overline{w}$ is typically of the order of 1 cm/s, and the horizontal components have magnitudes of the order of 1 m/s, it is customary to disregard the terms $uw/r, vw/r, 2\Omega w$, as these are small when compared to the horizontal advection or pressure gradient terms. The reduced equations of horizontal fluid motion for the GLA-AGCM are given as,

$$\frac{\partial u}{\partial t} = -\vec{U} \cdot \nabla u - w\frac{\partial u}{\partial z} - \frac{1}{\rho}\frac{\partial p}{\partial x} + (f + \frac{u \tan \phi}{r})v + \hat{x} \cdot \delta\vec{U}_{turb}. \tag{2.43}$$

$$\frac{\partial v}{\partial t} = -\vec{U} \cdot \nabla v - w\frac{\partial v}{\partial z} - \frac{1}{\rho}\frac{\partial p}{\partial y} - (f + \frac{u \tan \phi}{r})u + \hat{y} \cdot \delta\vec{U}_{turb}. \tag{2.44}$$

where $f = 2\Omega \sin \phi$ is called the Coriolis parameter.

The use of the hydrostatic expression (Equation (2.5)) and of Equation (2.42) yields,

$$\frac{\partial w}{\partial t} = -\vec{U} \cdot \nabla w - w\frac{\partial w}{\partial z} + \frac{u^2 + v^2}{r} + 2\Omega u \cos \phi + \hat{z} \cdot \delta\vec{U}_{turb}$$

Instead, the GLA-AGCM describes the pressure velocity by using Equation (2.18) to calculate the mass tendency $\frac{\partial \Pi}{\partial t}$ and then Equation (2.17) to calculate ω.

2.1.6.0 Finite Differences Form of the Equations

The equations of motion for a generic physical quantity, $Q = Q(\vec{x}, t)$, contain a local time derivative term, $\frac{\partial Q}{\partial t}$, advective terms, $\vec{u} \cdot \nabla Q$, and other forcing terms that take the form of local sources or sinks for Q. The values of Q are evaluated for a finite number of points in space, conforming a *mesh* or *grid.* The local time derivative terms and the advective terms for $Q(\vec{x}, t)$ must be represented as functions of the values at contiguous points. There are several methods to perform this finite resolution representation. Some AGCM's use a **finite differences form of the primitive equations**, others use **spectral methods**, **semi-lagrangian methods**, and **variable mesh size methods.**

In the spectral methods the field variables are represented as a truncated series of spherical harmonics, whose amplitude coefficients must be determined as a function of time. Some examples of an AGCM based on such methods are the National Center for Atmospheric Research

CCM1, as described in Williamson et.al. [1987] and Bath et.al. [1987], and the work by Lau and Peng [1987].

The semi-lagrangian methods are based on interpolations of the current field values to estimate the next time values of the prognostic variables. Some examples of this kind of work appear in Robert et.al. [1985], Ritchie [1988], and McDonald and Bates [1989].

The variable mesh size methods are normally used in oceanography to resolve small scale structures that arise within large scale field variations.

2.1.6.1 Notation

The GLA AGCM is a primitive equations model with a finite differences representation for the prognostic fields of u, v, w, θ, q, Π. The following subsections describe the finite difference form of the forcing terms for the mass divergence, the horizontal advection, the vertical advection, the pressure gradient force, the time filters, and the negative humidity corrections.

The three dimensional (3D) version of the GLA AGCM divides the lowest part of the atmosphere in K_m spherical shells or **layers** of finite thickness. Each layer is divided in a horizontal grid, with I_m uniformly distributed points in the longitudinal direction and $(J_m + 1)$ uniformly distributed points in the latitudinal direction. Let λ be the longitude and ϕ the latitude of a point on a spherical shell; then, $\Delta\lambda = 2\pi/I_m$ and $\Delta\phi = \pi/J_m$ are the grid spacings or angular resolutions in the longitudinal and latitudinal directions. The longitude and latitude are defined by,

$$\lambda = (i-1)\Delta\lambda \quad , \quad \text{for} \quad i = 1, 2, 3, \ldots, I_m. \tag{2.45}$$

$$\phi = j\Delta\phi - \pi/2 \quad , \quad \text{for} \quad j = 0, 1, 2, \ldots, J_m. \tag{2.46}$$

where $i = 1$ refers to the International Dateline and $j = 0$ to the South Pole. The most common resolution used for the GLA AGCM is 5° of longitude and 4° of latitude, in which case $I_m = 72$ and $J_m = 45$.

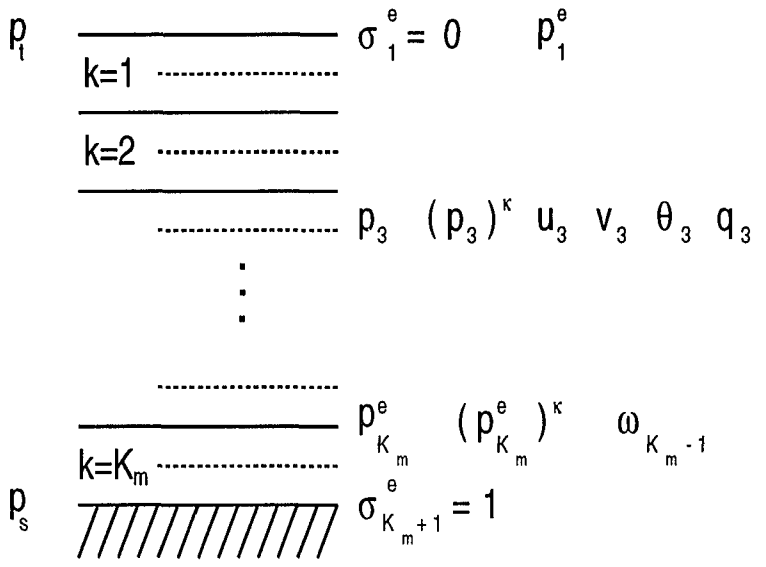

Figure 2.2 – Discretization of the vertical atmospheric column. The column of the simulated atmosphere is discretized in K_m layers. The terms in powers of the pressure are defined at the boundaries of each layer, and in the middle of each layer. The other prognostic variables are defined at the layers only. $K_m = 17$ for the current version of the GLA-AGCM.

The vertical direction is divided in K_m layers using the sigma coordinates of Arakawa and Suarez [1983] (see Fig. 2.2). If p_t is the pressure at the top of the simulated atmosphere and $p_s = p_s(x, y, z, t)$ is the pressure at the surface, then the pressure at the boundaries of the k^{th} layer are given by p^e_{k-1} and p^e_k, defined by

$$p^e_k = \sigma_k \Pi + p_t \quad , \quad \text{for} \quad k = 0, 1, 2, \ldots, K_m. \tag{2.47}$$

where $\sigma_k = k\Delta\sigma$ and $\Delta\sigma = 1/K_m$ for uniformly spaced layers. With $p_t = 10\text{mb}$, $p_s \simeq 1010\text{mb}$, and $K_m = 17$, the resolution in the vertical direction is $\Delta p \simeq 58.8\text{mb}$.

Any field variable, say Q, used in the AGCM is generally a function of position and time: $Q = Q(x, y, z, t)$. Four indices are needed to describe an instantaneous value of Q at a particular location; namely, $Q(x, y, z, t) \equiv Q^n_{ijk}$, where the set (i, j, k, n) maps the set (x, y, z, t). For example, the quantity Π/g is the mass areal density at the point $\vec{x} = (x, y, z_s)$ and time t, and

would be described as Π_{ij}^n/g. Notice that no k subscript has been included for Π since it is not an explicit function of height.

2.1.6.2 Mass Divergence

The finite difference form of the divergence of the horizontal mass flux can be represented in the following way. Define the provisional variables

$$X_{ijk} = \Pi_{ij} u_{ijk} \qquad Y_{ijk} = \Pi_{ij} v_{ijk} \cos\phi_{ij}. \tag{2.48}$$

The x and y parts of the mass divergence are represented by the centered finite differences,

$$T_{ijk}^1 = (X_{i+1,jk} - X_{i-1,jk})C_1 - (X_{i+2,jk} - X_{i-2,jk})C_2$$

$$T_{ijk}^2 = (Y_{i,j+1,k} - Y_{i,j-1,k})D_1 - (Y_{i,j+2,k} - Y_{i,j-2,k})D_2$$

where the constants are defined as $C_1 = 2/(3a\Delta\lambda)$, $C_2 = 1/(12a\Delta\lambda)$, $D_1 = 2/(3a\Delta\phi)$, $D_2 = 1/(12a\Delta\phi)$, and a is the radius of the Earth. The horizontal mass flux term in Equation (2.17)becomes

$$\nabla\cdot(\Pi\vec{u}) \simeq \frac{1}{\cos\phi_{ij}}(T_{ijk}^1 + T_{ijk}^2) \quad \text{for} \quad k = 0, 1, 2, \ldots, K_m. \tag{2.49}$$

An estimate of the vertical velocity, $\omega = dp/dt$, can be obtained from the continuity equation (Equation (2.15)), but it requires the gradient of the surface pressure field, $\nabla\Pi$, and the divergence of the mass flux, $\nabla\cdot(\Pi\vec{u})$, as in

$$\omega_{ijk'} \simeq -\sum_{k=1}^{k'} \Delta\sigma_k \nabla\cdot(\Pi_{ij}\vec{u}_{ijk}) + \sigma_{k+1}(\overline{\vec{u}}_{ijk}\cdot\nabla\Pi_{ij}). \tag{2.50}$$

The components of the vector $\overline{\vec{u}}_{ijk} = (\overline{u}_{ijk}, \overline{v}_{ijk})$ are given by the expressions

$$\overline{u}_{ijk} = \frac{\Delta\sigma_{k+1}u_{ijk} + \Delta\sigma_k u_{ij,k+1}}{\Delta\sigma_{k+1} + \Delta\sigma_k}. \tag{2.51}$$

$$\overline{v}_{ijk} = \frac{\Delta\sigma_{k+1}v_{ijk} + \Delta\sigma_k v_{ij,k+1}}{\Delta\sigma_{k+1} + \Delta\sigma_k}. \tag{2.52}$$

To avoid cluttering the formulas with indices, only those subscripts associated with the particular averaging or finite difference operation underway will be used in the expressions that follow; thus,

$T^1_{ijk} = (X_{i+1} - X_{i-1})C_1 - \ldots$ and $T^2_{ijk} = (Y_{j+1} - Y_{j-1})D_1 - \ldots$ will be the type of expressions used.

2.1.6.3 Horizontal Advection

By means of the provisional variables defined before in Equation (2.48), the horizontal advection terms for a generic variable Q are represented by

$$\frac{\partial(u\Pi Q)}{\partial x} \simeq \{[X_{i+1} + X_i](Q_{i+1} + Q_i) - [X_i + X_{i-1}](Q_i + Q_{i-1})\frac{C_1}{2} - \{[X_{i+2} + X_i](Q_{i+2} + Q_i) - [X_i + X_{i-2}](Q_i + Q_{i-2})\}\frac{C_2}{2} \quad (2.53)$$

$$\frac{\partial(v\Pi Q)}{\partial y} \simeq \{[Y_{j+1} + Y_j](Q_{j+1} + Q_j) - [Y_j + Y_{j-1}](Q_j + Q_{j-1})\frac{D_1}{2} - \{[Y_{j+2} + Y_j](Q_{j+2} + Q_j) - [Y_j + Y_{j-2}](Q_j + Q_{j-2})\}\frac{D_2}{2} \quad (2.54)$$

2.1.6.4 Vertical Advection

If w_k represents the pressure velocity, then the vertical advection for (Πu) and (Πv) at the k^{th} layer is represented by

$$\frac{\partial(w\Pi u)}{\partial \sigma} \simeq \frac{1}{2\Delta\sigma_k}[w_k(u_k + u_{k+1}) - w_{k-1}(u_{k-1} + u_k)]. \quad (2.55)$$

$$\frac{\partial(w\Pi v)}{\partial \sigma} \simeq \frac{1}{2\Delta\sigma_k}[w_k(v_k + v_{k+1}) - w_{k-1}(v_{k-1} + v_k)]. \quad (2.56)$$

for $k = 1, 2, \ldots, K_m$ and where $w_{K_m} = w_0 = 0$.

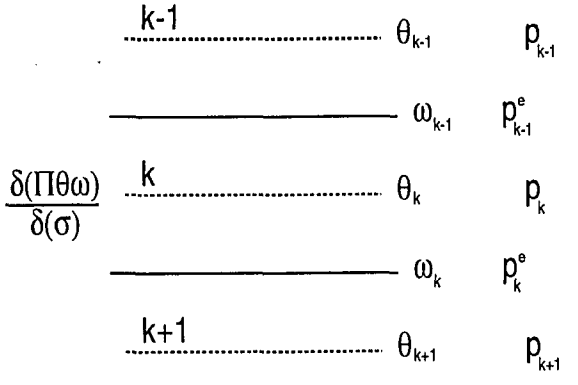

Figure 2.3 – Centered vertical finite differences for θ.

If p_k is the mean layer pressure and p_k^e is the pressure at the lower boundary of the k^{th} layer, then the vertical advection of potential temperature, θ_k, is represented by

$$\frac{\partial(w\theta\Pi)}{\partial\sigma} \simeq \frac{1}{\Delta\sigma_k}\left\{ w_k \frac{\left[(p_k^e)^\kappa - (p_k)^\kappa\right]\theta_k - \left[(p_k^e)^\kappa - (p_{k+1})^\kappa\right]\theta_{k+1}}{(p_{k+1})^\kappa - (p_k)^\kappa} \right. \\ \left. - w_{k-1}\frac{\left[(p_{k-1}^e)^\kappa - (p_{k-1})^\kappa\right]\theta_{k-1} - \left[(p_{k-1}^e)^\kappa - (p_k)^\kappa\right]\theta_k}{(p_k)^\kappa - (p_{k-1})^\kappa} \right\}. \tag{2.57}$$

for $k = 1, 2, 3, \ldots, K_m$ and where $w_{K_m} = w_0 = 0$. It is shown in Fig. 2.3 how the neighboring points contribute to the centered finite differences representation of the vertical advection of potential temperature.

If q_k is the specific humidity at the k^{th} layer, then the vertical advection of q_k is

$$w\frac{\partial q}{\partial\sigma} \simeq \frac{2}{\Delta\sigma_k}\left[\frac{w_k q_k q_{k+1}}{q_k + q_{k+1}} - \frac{w_{k-1}q_{k-1}q_k}{q_{k-1}+q_k}\right]. \tag{2.58}$$

for $k = 1, 2, \ldots, K_m$ and where $w_{K_m} = w_0 = 0$.

2.1.6.5 Pressure Gradient Force

The pressure gradient force is calculated with the use of the geopotential, $\Delta\Phi_k$, in the following scheme

$$\Delta\Phi_k = \left[(p_k^e)^\kappa - (p_k)^\kappa\right]\theta_k - \left[(p_k^e)^\kappa - (p_{k+1})^\kappa\right]\theta_{k+1}. \tag{2.59}$$

for $k = 1, 2, \ldots, K_m - 1$. At the surface, the geopotential is given by

$$\Phi_{K_m} = \Phi_s + C_p\theta_{K_m}\left[(p_{K_m}^e)^\kappa - (p_{K_m})^\kappa\right]. \tag{2.60}$$

where Φ_s is given by the fixed boundary conditions. The geopotentials at every layer can, then, be recalculated as

$$\Phi_k = \Phi_{k+1} + C_p\Delta\Phi_k \quad , \quad \text{for} \quad k = K_m - 1, \ldots, 2, 1. \tag{2.61}$$

The pressure gradient force is

$$\frac{\partial p}{\partial x} \simeq \Pi\left[\frac{\partial\Phi_k}{\partial x} + C_p\left(\theta_k - \frac{\theta_0}{(p_0)^\kappa}\frac{\partial(p_k)^\kappa}{\partial x}\right)\right]. \tag{2.62}$$

$$\frac{\partial p}{\partial y} \simeq \Pi \left[\frac{\partial \Phi_k}{\partial y} + C_p \left(\theta_k - \frac{\theta_0}{(p_0)^\kappa} \frac{\partial (p_k)^\kappa}{\partial y} \right) \right]. \tag{2.63}$$

where the divergence terms are represented as,

$$\frac{\partial \Phi_k}{\partial x} \equiv \frac{1}{\cos \phi} \left[(\Phi_{i+1} - \Phi_{i-1}) C_1 - (\Phi_{i+2} - \Phi_{i-2}) C_2 \right]. \tag{2.64}$$

$$\frac{\partial \Phi_k}{\partial y} \equiv (\Phi_{j+1} - \Phi_{j-1}) D_1 - (\Phi_{j+2} - \Phi_{j-2}) D_2. \tag{2.65}$$

and similarly for $(p_k)^\kappa$. Here, $\theta_0 = 280$ K, $p_0 = 1000$ mb.

2.1.6.6 Time Filter

To avoid the generation of numerical instabilities of very short time scales the GLA model uses the following filtering scheme, for the prognostic variables u, v, θ, q, and Π

$$Q_2' = (1 - \alpha) Q_2 + \frac{\alpha}{2} (2 Q_1 + \Delta t \frac{dQ}{dt})$$

Here, Q_1 and Q_2 are the values for two sucessive iterations of Q, and Q_2' is the filtered value.

2.1.6.7 Negative Humidity Correction

In some cases, because of numerical uncertainties, the difference between two similar values of the specific humidity might yield a negative value for q_{ijk}^n. At any layer and point where $q_{ijk}^n < 0$, then a two step procedure is followed to mix the moisture of the layer with the next lowest one,

$$q_k \doteq q_k + \frac{\Delta \sigma_{k-1}}{\Delta \sigma_k} q_{k-1} \qquad \text{and} \qquad q_{k-1} \doteq 0 \quad , \quad \text{for} \quad k = 2, 3, \ldots, k'. \tag{2.66}$$

where k' is defined such that $q_{k'} \geq 0$.

2.2.0 Physical parameterizations

The following subsections will describe some of the parameterizations included in the GLA-AGCM and in particular those that are closely related to the phenomena under study. This will serve as a basis in the justification of the present 1D simulations of tropical climate variability.

The design of an Atmospheric Global Climate Model (AGCM) with a coarse spatial and temporal resolution requires the inclusion of parameterized sub-grid scale processes. Some of the processes represented this way are the effects of cumulus convective activity, the turbulent fluxes at the surface boundary, and the radiative interactions with the main atmospheric gases. The computational models of the general circulation of the atmosphere were first designed to study climate phenomena induced by the large scale dynamics of the atmosphere, but to improve the compatibility between the observed and the simulated atmosphere, the need has arisen to include sub-grid scale processes that can modify the large scale fields. This is true even for those simulations in which the overall purpose is to recreate the minimum necessary conditions to generate particular atmospheric phenomena, and not the general atmospheric behavior.

Some parameterizations consists of a set of rules relating the mean dynamical properties of the grid box, as determined from the general flow characteristics, to the generation of atmospheric instabilities and the variations in the mass, heat and momentum exchanges. In those cases the interest resides on the cumulative effect of these exchanges on the large scale field, and not on the small scale (sub-grid size) perturbations. In the case of the radiative energy transfer problem the need for a parameterization arises from the large number of electromagnetic interactions with the atmospheric constituents and the complexity of those interactions. As an example, the absorption of energy in a particular wavelength range will depend on the distribution of cloud particle sizes and on the incidence angle of the radiation over that particular geographical point. The parameterizations of radiative transfer are designed to reduce the number of calculations to be performed for a broad range of the electromagnetic spectrum, per cycle of the simulation. In essence, the set of rules and the selection of local state variables that are to be expressed as a function of the mean grid box state conform a theoretical frame or **scheme** to present the parameterization.

2.2.1 The Parameterization of Cumulus Convection

The primitive equations AGCM has a finite spatial resolution that is typically of the order

of several hundred kilometers on the side of a regular grid box. A typical convective cloud in the tropics has a diameter of one or two kilometers. Even a collection of tropical cloud cells covers only a small fraction –usually less than 5%– of the total grid box area. Although generally small in extent, the cumulus cloud cells affect the mass, moisture and temperature fields in very significant ways by means of mass exchanges between the clouds and their environment, vertical transport of water vapor from the surface to the upper troposphere, release of latent heat, resultant sensible heat transport, environmental subsidence, changes in the planetary albedo, or the reduction of the outgoing longwave radiation from its clear sky values. Given the nonlinearity of the dynamical processes represented in an AGCM, the extra terms introduced in the equations of motion by the small scale cloud phenomena will produce noticeable differences from a non-parameterized climate simulation. A parameterization of the cumulus convective activity must then bridge the gap between the small scale cumulus effects, some of which were listed above, and the large-scale longer-term variability described by the AGCM dynamics. The accuracy of the description is of utmost importance for tropical areas where most of the precipitation is convectively produced, and where modification of the environment through convection occurs as a time-integrated effect (*e.g.* convective perturbations may provide extra amounts of moisture to the upper troposphere in a cumulative fashion, both spatially and temporally). Furthermore, the large scale dynamics (whether, wind convergence or sustained horizontally advecting winds) provide a supply of moisture to the tropical latitudes that is, either, locally processed or transported at high altitudes to other latitudes, by the overall convective regime. Hence, interactions between subgrid scales and large scale dynamics are an important aspect of the study of climate in the tropics.

Anthes [1977] classified the cumulus parameterization schemes in two general groups: (i) convective adjustment ; (ii) cloud model schemes. The first type is based on adjusting the moisture and temperature fields towards a moist neutral state. An example of these is the work of Manabe et.al. [1965]. These schemes are normally simpler in their construction and adjust

the large scale dynamical fields, T and q, through the release of latent heat and the immediate precipitation processes, but cannot adjust, as an example, for the radiative effects of clouds. The second type is designed to include the effects of the cumulus activity on the large scale dynamics by means of additional eddy terms in the equations of motion. Some examples of these are the works by Kuo [1965], Arakawa et.al. [1969], Ooyama [1971], Anthes [1977] and the presently discussed work of Arakawa and Schubert [1974]. These schemes calculate (or parameterize) the cloud activity as a function of the grid box mean dynamical state by means of a suitably defined cloud distribution model.

This presentation of the Arakawa-Schubert parameterization scheme will include a description of the relevant dynamical equations, a definition of the most relevant cloud environment variables, their inclusion into the dynamical equations, and a description of the cloud model in terms of the vertical mass flux. The notation used follows closely the notation used in the original paper by Arakawa and Schubert [1974]. The need for such a lengthy description is to understand the terminology and the concepts hidden in the parameterization, while presenting some important remarks relevant to these numerical experiments.

There have been several diagnostic studies of this parameterization, including the works by Lord and Arakawa [1980], Lord [1982] and Lord et.al. [1982]. Other works (Arakawa and Chen, 1986; Sud and Molod, 1988; Cheng, 1989a,b) have suggested improvements to this parameterization. The computational scheme used for the simulations discussed in this work included only the rain evaporation scheme implemented by Sud and Molod [1988].

The phenomena to represent the sub-grid scale cloud effects to be described fall in the class for which the air density, ρ, is assumed to be a function of height only. Hence, $\frac{\partial \rho}{\partial t} \simeq 0$, $\nabla \rho \simeq 0$. The continuity equation can then be written as,

$$\nabla \cdot (\rho \vec{u}) + \frac{\partial (\rho w)}{\partial z} = 0 \tag{2.67}$$

As before, $\vec{u} = (u, v)$, is the **horizontal wind velocity**, w the **vertical wind velocity**, all in units of [m/s], and $\nabla \equiv \hat{x}\frac{\partial}{\partial x} + \hat{y}\frac{\partial}{\partial y}$ is the horizontal gradient operator.

The thermodynamic state is described by the prognostic equations for **temperature**, T, **water vapor mixing ratio**, q, and **liquid water mixing ratio**, ℓ,

$$C_p \left(\frac{\partial T}{\partial t} + \vec{u} \cdot \nabla T + w \frac{\partial T}{\partial z} \right) = R + L(C - \mathcal{E}) \tag{2.68}$$

$$\frac{\partial q}{\partial t} + \vec{u} \cdot \nabla q + w \frac{\partial q}{\partial z} = \mathcal{E} - C \tag{2.69}$$

$$\frac{\partial \ell}{\partial t} + \vec{u} \cdot \nabla \ell + w \frac{\partial \ell}{\partial z} = C - \mathcal{E} - \mathcal{R} \tag{2.70}$$

Here R is the **radiative heating rate** in units of [J/kg-s]; C and $\mathcal{E}$ are the **condensation** and **evaporation** rates, respectively, in units of [kg/kg-s]; $\mathcal{R}$ is the **conversion rate of cloud liquid water to raindrops**, in units of [$\sec^{-1}$]; C_p the constant **specific heat of air**, in units of [J/kg-K]; and L the constant **latent heat of condensation**, in units of [J/kg].

There is no explicit inclusion of the ice phase, nor is there an explicit separation of the radiative effects of the liquid water and water vapor phases. Also, the coalescence of cloud droplets, sublimation and other processes are somewhat implicitly included in the prescription of $\mathcal{R}$. The simulated atmosphere can be separated into a mixed boundary layer (sometimes called the planetary boundary layer, PBL) covering the lowest 50 mb to 100 mb, a cloud layer covering the middle 700 mb, and a small portion of the stratosphere covering about 200 mb. For the simulations reported in this work there are 17 layers in total: approximately, 2 in the PBL, 12 in the cloud layer, and 3 in the stratosphere.

Clouds are assumed to be regions of condensed water that has not been converted to liquid raindrops. These can exists anywhere in that middle cloud layer provided that the local thermal state and the amounts of moisture are favorable to their formation. The scheme does not treat individual clouds in the end, but does estimate their cumulative properties as a function of the mean grid box state.

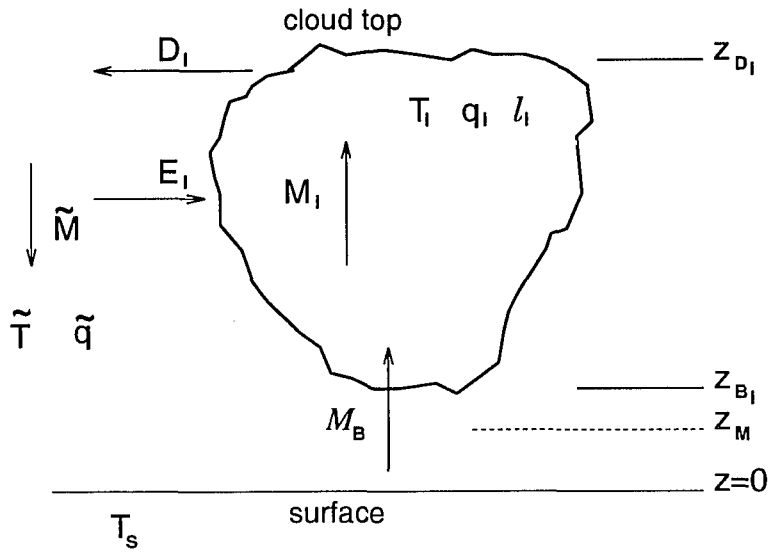

Figure 2.4 – Cloud and environment variables.

First, consider a justification of the terms based on a continuous vertical coordinate system. The purpose is to develop the set of rules relating the cumulative properties of the clouds to the mean state of the layer. Fig. 2.4 illustrates some of the terms defined in the following paragraphs.

The **vertical mass flux** for the i^{th} cloud, M_i, across the horizontal cloud area, σ_i, is defined as,

$$M_i \equiv \int_{\sigma_i} d^2x \; \rho w = \rho \sigma_i w_i \tag{2.71}$$

where w_i is the constant vertical velocity for the i^{th} cloud at a level z. The $(i+1)^{\text{th}}$ cloud has, perhaps, a different set of σ_i, w_i, M_i at level z.

In general, the surrounding air can enter the vertical plume of ascending air in the cloud cell (a process called **entrainment**, E_i), or there can be mass transport from the vertical plume into the environment (a process called **detrainment**, D_i). The entrainment of environmental air will tend to dilute the moist air of the cloud cell and to reduce its buoyancy. This horizontal transport of mass is related to the vertical gradient of the vertical mass flux and to the growth rate of the cloud's horizontal cross sectional area,

$$E_i = \frac{\partial M_i}{\partial z} + \rho \frac{\partial \sigma_i}{\partial t} \quad , \quad \text{for} \quad \frac{\partial M_i}{\partial z} + \rho \frac{\partial \sigma_i}{\partial t} > 0 \quad \text{(entraining cloud layer)} \tag{2.72}$$

$$D_i = -\frac{\partial M_i}{\partial z} - \rho\frac{\partial \sigma_i}{\partial t} \quad , \quad \text{for} \quad \frac{\partial M_i}{\partial z} + \rho\frac{\partial \sigma_i}{\partial t} < 0 \quad \text{(detraining cloud layer)} \tag{2.73}$$

The cloud model will specify the conditions under which these horizontal mass transport types occur. The net vertical cloud mass flux in the grid box area at level z is $M_c = \sum_i M_i$ and the net area occupied by clouds is $\sigma_c = \sum_i \sigma_i$. Notice that σ_i as well as σ_c can be functions of height. The environmental area encompasses the rest of the unit grid box area that is not occupied by clouds, $(1 - \sigma_c)$, with a horizontally uniform vertical mass flux $\tilde{M}$. The mean vertical mass flux for a unit area then is given by

$$\rho\overline{w} = M_c + \tilde{M} \tag{2.74}$$

The integration of the continuity equation (Equation (2.67)) over the unit grid box area yields,

$$\overline{\nabla \cdot (\rho\vec{u})} + \frac{\partial(\rho\overline{w})}{\partial z} = 0$$

The sum of the values for E_i and D_i over all the clouds in the grid box at a height z is,

$$E - D = \frac{\partial M_c}{\partial z} + \rho\frac{\partial \sigma_c}{\partial t} \tag{2.75}$$

where $E = \sum_i E_i$ (summing over the entraining clouds only), and $D = \sum_i D_i$ (summing over the detraining clouds only), and the assumption that $\nabla\rho \simeq 0$ has been used.

The equation for T, (Equation (2.68)) can be redefined in terms of the **static energy**, s, as

$$s = C_p T + gz \tag{2.76}$$

It can be proven that for dry adiabatic and hydrostatic processes, (see section 2.1.3) the vertical gradient of s is given by

$$\frac{\partial s}{\partial z} = C_p \left(\frac{p}{p_0}\right)^{\kappa} \frac{\partial \theta}{\partial z} \quad , \quad \kappa = R'/C_p$$

where p is the level's pressure, p_0 the reference surface pressure, θ the potential temperature, and R' the gas constant for air.

The equation for the temperature then becomes,

$$\frac{\partial s}{\partial t} = -\vec{u} \cdot \nabla s - w\frac{\partial s}{\partial z} + R + L(C - \mathcal{E}) \tag{2.77}$$

This last equation is multiplied by ρ and added to Equation (2.67) multiplied by s, and integrated over the grid box area to obtain,

$$\rho\frac{\partial\overline{s}}{\partial t} = -\overline{\nabla\cdot(\rho\vec{u}s)} - \overline{\frac{\partial(\rho ws)}{\partial z}} + \rho\left(\tilde{R} + \sum_i R_i - L\mathcal{E} + L\sum_i C_i\right)$$

Here, $\tilde{R}$ and R_i represent the radiative heating rates for the environment and for the i^{th} cloud, respectively. Adding the terms of $\overline{s}\left[\overline{\nabla\cdot(\rho\vec{u})} + \overline{\frac{\partial(\rho w)}{\partial z}}\right] = 0$ to the previous equation, and using the following approximations,

$$\overline{\nabla\cdot(\rho\vec{u})} \simeq \nabla\cdot(\rho\ \overline{\vec{u}}) \tag{2.78}$$

$$\overline{\nabla\cdot(\rho\vec{u}s)} \simeq \nabla\cdot(\rho\ \overline{\vec{u}}\ \overline{s}) \tag{2.79}$$

$$\overline{\nabla\cdot(\rho\vec{u}q)} \simeq \nabla\cdot(\rho\ \overline{\vec{u}}\ \overline{q}) \tag{2.80}$$

it can be shown that

$$\rho\frac{\partial\overline{s}}{\partial t} = -\frac{\partial}{\partial z}[\rho\overline{ws} - \rho\ \overline{w}\ \overline{s}] + \rho(\tilde{R} + \sum_i R_i) + \rho L(\sum_i C_i - \mathcal{E}) - \rho\overline{\vec{u}}\cdot\nabla\overline{s} - \rho\overline{w}\frac{\partial\overline{s}}{\partial z} \tag{2.81}$$

Similarly for q,

$$\rho\frac{\partial\overline{q}}{\partial t} = -\frac{\partial}{\partial z}[\rho\overline{wq} - \rho\ \overline{w}\ \overline{q}] + \rho(\mathcal{E} - \sum_i C_i) - \rho\overline{\vec{u}}\cdot\nabla\overline{q} - \rho\overline{w}\frac{\partial\overline{q}}{\partial z} \tag{2.82}$$

The forcing terms on the local rate of change for $\overline{s}$ and $\overline{q}$ are divided in three groups: eddy flux terms, the normally expected radiative and condensational heating terms, and the mean flow (vertical and horizontal) gradient terms. The terms of the form $\overline{\rho ws} - \rho\ \overline{w}\ \overline{s} = \overline{\rho w's'}$ refer to the vertical flux of static energy by the cumulus eddies. Since,

$$\overline{\rho ws} \equiv \int d^2x\ \ \rho ws = \sum_i \rho\sigma_i w_i s_i + (1-\sigma_c)\rho\tilde{w}\tilde{s}$$

then

$$\overline{\rho w's'} = \sum_i \rho\sigma_i\left[w_i(s_i - \overline{s}) - \tilde{w}(1-\sigma_c)(s_i - \tilde{s})\right] \tag{2.83}$$

It has been stated that the typical fractional area occupied by a cloud cell is very small and that the vertical velocity of the environmental air is also rather small. Under such conditions, $\sigma_i \tilde{w} \ll 1$ and then,

$$\overline{\rho w' s'} \simeq \sum_i M_i (s_i - \overline{s}) \tag{2.84}$$

Similarly for q,

$$\overline{\rho w' q'} \simeq \sum_i M_i (q_i - \overline{q}) \tag{2.85}$$

Hence, by using the continuity and the modified thermodynamic equations, the local changes of the grid box mean temperature and humidity fields have been related to the vertical gradient of the vertical transport of static energy and moisture induced by the cumulus eddies. The vertical mass flux eddies have been related to the vertical flux of the excess static energy and moisture of the clouds.

A similar set of equations to Equation (2.81) and Equation (2.82) can be obtained by applying the equations for s and q to the environmental area. If the net area covered by clouds is assumed to be small, $\sigma_c \ll 1$, and for a not so dry environment, $\overline{s} \approx \tilde{s}$ and $\overline{q} \approx \tilde{q}$, and after some algebraic manipulation the tendency equations for $\tilde{s}$ and $\tilde{q}$ yield,

$$\rho \frac{\partial \tilde{s}}{\partial t} = \sum_i D_i (s_{D_i} - \overline{s}) - \tilde{M} \frac{\partial \overline{s}}{\partial z} + \rho (\tilde{R} - L\mathcal{E} - \overline{\vec{u}} \cdot \nabla \overline{s}) \tag{2.86}$$

$$\rho \frac{\partial \tilde{q}}{\partial t} = \sum_i D_i (q_{D_i} - \overline{q}) - \tilde{M} \frac{\partial \overline{q}}{\partial z} + \rho (L\mathcal{E} - \overline{\vec{u}} \cdot \nabla \overline{q}) \tag{2.87}$$

The terms $\tilde{R}$, $\mathcal{E}$, and $\rho \overline{\vec{u}} \cdot \nabla \overline{s}$ have the expected form. The term related to D_i show that the detrainment of the excess static energy in the clouds (and moisture, for the case of q) will raise the mean temperature (or water vapor mixing ratio) in the layer's environment. Since $\frac{\partial s}{\partial z} > 0$, the extra term in the equation shows that the subsiding environmental air (for $\tilde{M} < 0$) warms up the grid box area. The environmental subsidence tends to dry out the grid's area, also, for the typical case of $\frac{\partial q}{\partial z} < 0$, but it can moisten any layer whenever $\frac{\partial q}{\partial z} > 0$. Hence, any precipitation that reevaporates in the next lower layer might load up the environment with water vapor.

If the detrained liquid water evaporates at the same level,

$$\mathcal{E} = \sum_i D_i \ell_{D_i} \tag{2.88}$$

where ℓ_{D_i} is the liquid water mixing ratio from the i^{th} detraining cloud. This assumption restricts interlayer evaporation to detrained liquid water. The modification of the parameterization by Sud and Molod [1988] is intended to relax this restriction by adding the possible interlayer evaporation of rain.

Hence, the equations that describe the effects of the cumulus activity on the environment (Equation (2.86) and Equation (2.87)) were presented. The environment is affected by the sensible heat and moisture transport of the detraining air, and by the adiabatic heating and drying of the convectively induced subsidence, in addition to the known terms. However, the goal of the cumulus parameterization is to describe the cloud amounts and distributions as a function of the mean spatial properties of the grid box.

The process has also been identified by which small amounts of moisture can remain at higher levels after convective activity, and by which a slow moistening of the whole simulated troposphere can occur: namely, the detrainment of cloud water and/or the reevaporation of precipitation. This is equivalent to a "diurnal pumping", or for a better name and because of the different time scales involved, a "convective pumping of moisture". It is expected that the time scales of such a process are to be longer than the "cumulus convection adjustment time" refered to in Arakawa and Schubert [1974].

It is necessary to apply the equations for s, q, and ℓ to the clouds. At any given layer, the i^{th} cloud could be entraining or detraining moist air. The use of the definition for E_i (Equation (2.72)), multiplied by s, and integrated over σ_i yields,

$$\overline{s}E_i = s_i \frac{\partial M_i}{\partial z} + \rho s_i \frac{\partial \sigma_i}{\partial t}$$

where the entraining air has static energy $\overline{s}$. For a saturated cloud, $\mathcal{E}_i = 0$, and with the assumptions that $\nabla s_i = 0$ and $\frac{\partial \rho}{\partial t} = 0$, the equations for the static energy and the water phases

are,

$$\frac{\partial(\rho\sigma_i s_i)}{\partial t} = -\frac{\partial(M_i s_i)}{\partial z} + \overline{s}E_i + \rho\sigma_i(LC_i + R_i)$$

$$\frac{\partial(\rho\sigma_i q_i)}{\partial t} = -\frac{\partial(M_i q_i)}{\partial z} + \overline{q}E_i - \rho\sigma_i C_i$$

$$\frac{\partial(\rho\sigma_i \ell_i)}{\partial t} = -\frac{\partial(M_i \ell_i)}{\partial z} + \rho\sigma_i(C_i - \mathcal{R}_i)$$

These three can be combined to form,

$$\frac{\partial(\rho\sigma_i h_i)}{\partial t} = -\frac{\partial(M_i h_i)}{\partial z} + \overline{h}E_i + \rho\sigma_i R_i \tag{2.89}$$

$$\frac{\partial(\rho\sigma_i[q_i + \ell_i])}{\partial t} = -\frac{\partial(M_i[q_i + \ell_i])}{\partial z} + \overline{q}E_i - \rho\sigma_i\mathcal{R}_i \tag{2.90}$$

where $h = s + Lq$ is called the **moist static energy** and $(q_i + \ell_i)$ is called the **total water substance**. From Equation (2.89) it can be seen that in the absence of the radiative heating term, $\rho\sigma_i R_i$, the balance in the moist static energy flux is achieved if $\overline{h}E_i = \frac{\partial(M_i h_i)}{\partial z}$. There are three sources (or sinks) to the total water substance within the cloud plume: the vertical gradient of the moist mass flux, entraining water vapor from the environment, and depletion by precipitation.

For the detraining layer of the i^{th} cloud the equations are,

$$\rho s_i \frac{\partial \sigma_i}{\partial t} = -D_i s_i - s_i \frac{\partial M_i}{\partial z}$$

$$\frac{\partial(\rho\sigma_i s_i)}{\partial t} = -D_i s_i - \frac{\partial(M_i s_i)}{\partial z} + \rho\sigma_i(LC_i + R_i)$$

$$\frac{\partial(\rho\sigma_i q_i)}{\partial t} = -D_i q_i - \frac{\partial(M_i q_i)}{\partial z} - \rho\sigma_i C_i$$

$$\frac{\partial(\rho\sigma_i \ell_i)}{\partial t} = -D_i \ell_i - \frac{\partial(M_i \ell_i)}{\partial z} + \rho\sigma_i(C_i - \mathcal{R}_i)$$

Some simple relations between variables will be needed. The cloud air is saturated, and the pressures inside and outside the cloud are assumed to be very similar,

$$q_i = q^*(T_i, p_i) \simeq q^*(T_i, \tilde{p}) \simeq q^*(T_i, \overline{p})$$

then,

$$q_i \simeq \tilde{q}^* + \frac{\partial \tilde{q}^*}{\partial \overline{T}}(T_i - \tilde{T}) \simeq \overline{q}^* + \frac{\gamma}{L}(s_i - \overline{s})$$

where, for constant pressure,

$$\gamma \equiv \frac{L}{C_p}\left(\frac{\partial \overline{q}^*}{\partial \overline{T}}\right)_{\overline{p}} \qquad \text{and} \qquad \overline{q}^* = q^*(\overline{T}, \overline{p}).$$

Also,

$$(1+\gamma)(s_i - \overline{s}) = h_i - \overline{h}^* \tag{2.91}$$

$$q_i - \overline{q}^* = \frac{\gamma}{1+\gamma}\frac{1}{L}(h_i - \overline{h}^*) \tag{2.92}$$

The environment is assumed to be near saturation in the previous expressions. Hence, the cloud's mixing ratio is described in terms of the mean properties of the grid cell and the temperature dependent saturation mixing ratio. The stability of the environment can be described also from the saturated moist adiabatic lapse rate,

$$\frac{\partial \overline{h}^*}{\partial z} >=< 0 \tag{2.93}$$

for the **stable**, **neutral** and **unstable** cases.

Arakawa and Schubert [1974] construct a cloud model based on the following specification of the properties of the clouds:

(i) growing clouds are entraining at all levels;

(ii) for a cloud that has reached its maximum height, detrainment occurs only at a thin layer at the cloud top;

(iii) the cloud top is located at the level of vanishing buoyancy;

(iv) the excess cloud static energy determines the sign of the buoyant force.

The second assumption can be used to characterize the type of clouds. Since D_i is a function of the vertical mass flux, M_i, then Arakawa and Schubert [1974] defined a parameter μ that will

characterize the cloud type. This parameter was related to the fractional entrainment rate in the following way. Within a thin layer of thickness δz at the cloud top,

$$-D(z)\delta z = \mathcal{M}(z,\mu_D)\delta\mu$$

where $D = \sum_{\mu_D<\mu_i<\mu_D+\delta\mu} D_i$ and $\mathcal{M}(z,\mu_D)\delta\mu \equiv \sum_{\mu_D<\mu_i<\mu_D+\delta\mu} M_i$, for all the clouds that detrain at level z_D. The quantity μ_D is defined as $\mu_D = \mu(z_D)$. Furthermore, the **mass flux at the base of the cloud** (or nearly above the mixed layer), $\mathcal{M}_B$, is defined from

$$\mathcal{M}(z,\mu) = \mathcal{M}_B(\mu)\eta(z,\mu) \tag{2.94}$$

Here $\mathcal{M}(z,\mu)$ refers to the total mass flux from all the clouds that, at least, reach level z, whether those that detrain at $z_D = z$ or those whose cloud top is higher. Each μ_D is characteristic of a cloud type, or "subensemble" of clouds, as Arakawa and Schubert [1974] termed the types of clouds. By using Equation (2.72) for an entraining cloud cell, added over all cloud of the same type, yields

$$\frac{\partial\eta}{\partial z} = \frac{1}{\mathcal{M}_B\delta\mu}\sum_{\mu<\mu_i<\mu+\delta\mu} E_i$$

In this expression the time derivative of the areal expansion term have been discarded from Equation (2.72). From the expressions for h_i (Equation (2.89)) and $(q_i+\ell_i)$ (Equation (2.90)) it can be shown that,

$$\overline{h}\frac{\partial\eta}{\partial z} = \frac{\partial(\eta h_c)}{\partial z}$$

$$\overline{q}\frac{\partial\eta}{\partial z} = \frac{\partial\left(\eta[q_c+\ell_c]\right)}{\partial z} + \eta r \qquad \text{where} \qquad r = \frac{1}{\mathcal{M}}\sum_{\mu<\mu_i<\mu+\delta\mu}\mathcal{R}_i$$

These two expressions can be translated to,

$$\frac{\partial h_c}{\partial z} = -\mu(h_c - \overline{h})$$

$$\frac{\partial(q_c+\ell_c)}{\partial z} = -\mu(q_c+\ell_c-\overline{q}) - r$$

It is seen that for higher values of μ the excess cloud moist static energy and the excess water substance decrease faster with height. This implies that there will be a level at which clouds of

type μ_D loose buoyancy. This is consistent with the buoyancy conditions Equation (2.91) and Equation (2.92). For a constant $r(z,0)$ the upper layers would produce less precipitation than the lower layers. With a parameterized $r(z,\mu)$, and the terms $h_c(z_B), q_c(z_B)$ determined by subcloud base processes, then a determination of $\eta(z,\mu)$ and $\mathcal{M}_B(\mu)$, with the proper boundary conditions, constitute the cumulus parameterization.

It is assumed that within each cloud type or subensemble, the cloud cells are at random phases in their life cycles. This is a sensible assumption only when the cloud life time is much smaller than the environmental climate changes time scales. This is called the "quasi equilibrium" assumption. The Arakawa and Schubert [1974] parameterization assumes that because of this random phases condition, the instantaneous mass flux for the subensemble is proportional to the net mass flux for a single cloud cell integrated over its lifetime. Then it is sensible to select a constant fractional rate of entrainment,

$$\frac{1}{\eta}\frac{\partial \eta}{\partial z} \equiv \mu \tag{2.95}$$

Then, the specification of $\eta(z,\mu)$ is given by,

$$\begin{aligned} \eta(z,\mu) &= \exp(\mu[z - z_B]) \quad \text{for} \quad z_B \leq z \leq z_D \\ &= 0 \qquad\qquad\qquad\quad \text{for} \quad z > z_D \end{aligned} \tag{2.96}$$

2.2.2 Turbulence of the planetary boundary layer

In the design of an AGCM there are several boundary conditions that require specification. The surface boundary conditions of roughness, temperature, albedo and availability of moisture must be properly coupled to the lowest layer's momentum transfer, sensible and latent heat transport. The role of the parameterization for turbulence processes in the planetary boundary layer (PBL) is to link (by specifying) the surface fluxes to the forcing of the prognostic variables in the lowest layers of the AGCM. This section is a brief description of the Helfand and Labraga [1988] parameterization of atmospheric turbulence.

The objective of this parameterization is to predict the turbulent fluxes of mass, heat and momentum. The fluxes are constructed as functions of the second moments (*i.e.* variances and covariances) of the potential temperature, specific humidity, kinetic energy, and momentum. Different from a bulk parameterization of the fluxes, the scheme used for the GLA–AGCM resolves the PBL structure by specifying several layers in the lowest 150 mb of the simulated troposphere. Such a treatment has the definite advantages of providing prognostic variables that can be compared to surface layer measurements (*e.g.* whether remotely sensed winds or meteorological station's datasets), and of smoothing out the transition from the specified surface boundary conditions to the dynamically controlled values of the free atmosphere. The article by Helfand [1985] specifies the desire to build a parameterization that is grid-size independent, and that includes a flux scheme suitable for turbulent interlayer exchanges above the PBL in the free atmosphere.

The Helfand and Labraga [1988] work belongs to a hierarchy of turbulence schemes developed by Mellor and Yamada [1974,1982]. It is a modification of one of their schemes for use in an AGCM and introduced by Yamada [1977], and termed a Level 2.5 second-order closure model for turbulence.

The Helfand and Labraga [1988] work is based, initially, in a "boundary layer approximation". This approximation is a set of simplifications to be applied in the eddy interactions equations: (1) the horizontal gradients of the horizontal eddy velocity and eddy potential temperature are neglected for being much smaller than their vertical counterparts; (2) the horizontal divergence of the turbulent flux terms are negligible; (3) the vertical gradient of the vertical component of the eddy wind is neglected; (4) the flux divergence of vertical momentum is neglected; (5) to generalize the theory to the free atmosphere, it is necessary to express the turbulence length scale as independent of the distance from the surface. With these assumptions, a set of equations for the budgets of the turbulent kinetic energy (TKE), the variance in the kinetic energy for each of the components of the velocity (called the components of the variance of the

velocity), the vertical flux of horizontal momentum, the variance of the potential temperature, the vertical flux of potential temperature, and for the horizontal flux of potential temperature is constructed. Implicitly, five more equations are added by treating the specific humidity variance and fluxes similarly to the case of the potential temperature.

In general, the Helfand and Labraga [1988] treatment of atmospheric turbulence in terms of budget equations for the variances contain terms in the vertical gradients of the horizontal components of the velocity, of the TKE and of the potential temperature. Only the equation for the time rate of change in TKE contains horizontal gradient terms, which are then neglected based on the boundary layer approximation.

The system of equations is inherently dependent on the square of the vertical shear of the mean horizontal wind, and on the vertical gradient of the potential temperature. By constructing dimensionless variables, the set of equations are transformed into an algebraic system of equations upon which certain restrictions (or realizability conditions) are imposed. The process adds one prognostic equation to the AGCM set of variables for the TKE. There are production and dissipation terms for the TKE. An "equilibrium TKE" is defined from the solutions to the case when production balances dissipation; this equilibrium value is related to the master length scale (*i.e.* the turbulence length scale) of the parameterization.

Helfand and Labraga [1988] divide the solutions into three possible regimes: (1) rapidly growing turbulence (*i.e.* whenever the TKE is smaller than its equilibrium value); (2) the near equilibrium case; (3) the rapidly decaying turbulence case (*i.e.* the TKE is larger than its equilibrium value). The solutions of the algebraic system works fine for the later two cases, but not for the first one. To improve this inability of the parameterization to handle the rapidly growing turbulence case, some of the terms not considered in the boundary layer approximation for the Level 2.5 scheme must be included. To simplify the calculations, it is assumed that the ratio of the combined growth rate, advection and vertical diffusion, to the production term, for each of the other moments, is proportional to a similarly defined ratio for the TKE. The implication

is that the TKE and the potential temperature variance, for example, change simultaneously. The production rate of the TKE depends positively on the vertical eddy flux of eddy potential temperature, and negatively on the vertical eddy flux of the vertical shear of the mean horizontal wind. The production rate of the potential temperature variance is a function of the negative vertical eddy flux of potential temperature and the lapse rate of the mean potential temperature. Under such terms, for larger vertical eddy flux of potential temperature there is a larger generation of TKE, which in turn will reduce the deviation from equilibrium of the vertical eddy flux of the temperature and lapse rate. Hence, although turbulent buoyancy will tend to increase the TKE, it will tend to equilibrate the lapse rate.

In essence, the larger the TKE departure from equilibrium, the faster will the variance in the temperature vanish. In that context, the mean field values (as determined by the other components of the AGCM) of the potential temperature lapse rate, mean horizontal wind shear, and vertical gradient of the specific humidity intervene in the generation of turbulent eddies for $\theta, q, u,$ and v.

2.2.4 Longwave Radiative Interactions (LWR)

The representation of the longwave electromagnetic (EM) interactions with the atmospheric constituents requires, nominally, the calculation of the transmittances for narrow spectral bands at each grid point in space, for which the concentrations of atmospheric gases and particles are known, and then the integration through a range of frequencies to obtain the thermal forcing terms at each time step. Since air is a mixture of gases (*e.g.*, nitrogen, oxygen, carbon dioxide, ozone, water vapor) and particles of multiples sizes (*e.g.*, water droplets, biogenic materials), there are, consequently, numerous absorption lines for the former types, and light scattering processes induced by the later types. The representation of the EM interactions in terms of narrow spectral bands might be computationally laborious, both in its complexity and time consumption.

To reduce the number of computations several approaches have been taken for the use of long wave radiation (refered to as LWR) codes in the field of atmospheric climate simulations.

One approach is to perform a spectrally detailed calculation at longer time intervals than the time step of the integration. A disadvantage of this procedure is the incomplete representation of radiative interactions within the life-cycle of convective cells, which simulate the most important ways in which water vapor amounts are adjusted in the upper troposphere. Another approach is to use a set of spectral band approximations to the collective effects of several spectral lines in the radiative fluxes, but at time steps similar to those of the convective adjustments.

The currently used version of the GLA-AGCM uses band approximations at longer time steps. This section describes briefly the spectral bands used in the calculation of the LWR transmittances, as documented in Harshvardhan and Corsetti [1984], and in a rather general approach, the calculation of the heating rates.

The calculation of the longwave heating rate profile, δT_{LWR}, requires the upward and downward radiative fluxes, $F_\uparrow$ and $F_\downarrow$, as a function of the pressure at each level, p. For a clear sky atmosphere the fluxes can be obtained from,

$$F^c_\uparrow(p) = \int_{\Delta\nu} d\nu \left[B_\nu(T_s)\tau_\nu(p,p_s) + \int_{p_s}^{p} dp' \; B_\nu(T(p'))\frac{d\tau_\nu(p,p')}{dp'} \right] \tag{2.97}$$

$$F^c_\downarrow(p) = \int_{\Delta\nu} d\nu \left[\int_{p_t}^{p} dp' \; B_\nu(T(p'))\frac{d\tau_\nu(p')}{dp'} \right] \tag{2.98}$$

Here $\Delta\nu$ is the spectral range in wavenumbers for the calculation; $B_\nu(T_s)$ is the blackbody spectral density flux from the surface at the temperature T_s; $\tau_\nu(p,p')$ is the spectral diffuse transmittance between the pressure levels p and p'; and p_t is the pressure at the top of the atmosphere. The blackbody spectral density flux, $B_\nu(T)$, is expressed as,

$$B_\nu(T) = \frac{2hc^2\nu^3}{\exp(hc\nu/kT) - 1}$$

where h, k and c stand for the Planck, Boltzmann, and speed of light constants, respectively.

The first term in Equation (2.97) is due to blackbody emissions from the surface, that are transmitted through all atmospheric layers up to the level at pressure p. The second term,

or the exchange term, is the integrated contribution of the emissions from all layers at pressure p', $(p' > p)$, and temperature $T(p')$, that reach the level at pressure p. The term in Equation (2.98) represents the integrated contributions from all layers above the pressure level p, $(p' < p)$.

Table 2.1

Spectral Regions for the LWR Calculation

Substance	Centers (cm^{-1})	Wings (cm^{-1})
Water vapor	0–340	340–540
	1380–1900	800–980
		1100–1380
		1900–3000
Carbon dioxide	620–720	540–620
		720–800
Ozone	980–1100	

The vertical gradients of the fluxes at any level are then used to calculate the heating rates, as in,

$$\left.\frac{\partial T}{\partial t}\right|_{LWR} = \frac{g}{C_p}\frac{d}{dp}(F_\uparrow - F_\downarrow) \tag{2.99}$$

In practice, though, the heating rate profile depend on the finite differences representation of the vertical gradient of the fluxes. Perhaps, an improvement on the current way of performing these heating rates calculations would be to use a finer vertical resolution for the estimation of the $F_\uparrow$ and $F_\downarrow$ terms, and then, to use a higher order finite differences representation of the derivatives.

Instead of performing detailed calculations of the fluxes for separate spectral absorption lines, a number of approximations are used within selected absorption bands. These spectral

bands are presented in Table 2.1 for the substances for which radiative absorption is considered of importance. The transmittances are calculated for these spectral bands, with different approximations for each band. Just a general sketch of the calculations is included below.

An integration by parts on wavenumbers can transform Equation (2.97) and Equation (2.98) :

$$F^c_{\uparrow}(p) = B(T(p)) + G(p, p_s, T_s) - G(p, p_s, T(p_s)) + \int_{T(p)}^{T(p_s)} dT(p') \; \frac{\partial G}{\partial T}(p, p', T(p')) \qquad (2.100)$$

$$F^c_{\downarrow}(p) = B(T(p)) - G(p, p_t, T(p_t)) + \int_{T(p)}^{T(p_t)} dT(p') \; \frac{\partial G}{\partial T}(p, p', T(p')) \qquad (2.101)$$

where the functions G and $\frac{\partial G}{\partial T}$ are defined as,

$$G(p, p', T) = \int_{\Delta\nu} d\nu \; \tau_\nu(p, p') B_\nu(T) \qquad \text{and} \qquad \frac{\partial G}{\partial T} = \int_{\Delta\nu} d\nu \; \tau_\nu(p, p') \frac{\partial B_\nu}{\partial T}(T) \qquad (2.102)$$

If $\tau_\nu(p, p')$ is the transmittance at wavenumber ν between the layers at pressures p and p', then the function $G(p, p', T)$ represents the flux of blackbody emissions from the layer at temperature T.

For a narrow range of wavenumbers where $B_\nu(T)$ is not varying rapidly, the function G can be approximated as

$$G(p, p', T) = \overline{B}(T) \int_{\Delta\nu} d\nu \; \tau_\nu(p, p') \qquad \text{and} \qquad \overline{B}(T) = \frac{1}{\Delta\nu} \int_{\Delta\nu} d\nu \; B_\nu(T) \qquad (2.103)$$

The transmittances can be calculated as functions of the optical path for individual substances. The optical paths are constructed as functions of the temperature, pressure of the bounding levels, mixing ratio of the constituents and the vapor pressures. In the current version of the GLA-AGCM the profiles of CO_2 and O_3 concentrations are prescribed. Only the mixing ratio for water vapor is allowed to vary as a function of time. Hence, the dynamically calculated profile $q(\sigma)$ is used as input to the calculation of the heating rates, δT_{LWR}.

The transmittances are non-linear functions of the optical paths, and hence, minute differences in the values of the pressure, temperature and concentrations, can have significant effects

in the estimates of the fluxes. Interpolation techniques can be used, then, to estimate subgrid variations in the profiles of the variables supplied by the dynamics of the AGCM. This model takes the mixing ratio of water vapor as constant throughout the layer, and interpolates the temperatures as a logarithmic function of the pressure of the levels. The calculation of the optical paths for the center and wings of the different spectral bands, and of the transmittances from the calculated optical paths, are explained in detail in Harshvardhan and Corsetti [1984], Chou and Arking [1980], and Chou [1984].

In the case of the cloudy skies simulation, it is assumed that the clouds are optically black in the infrared wavenumbers, and a concept of partial cloud cover is implemented. The clouds cover the layer entirely in the vertical direction, but only a fraction, n (defined as **partial cloud cover**, and within the range of 0. to 1.), of the horizontal extension of the grid box. The idea is to construct an estimate of the probability of a clear line of sight between two specified levels, and between the surface level and the top of the atmosphere, given the different cloud cover amounts for the cloudy layers. This probability of a clear line of sight is estimated as a fraction of the maximum cloud overlap of the column. The maximum cloud overlap is given by the layer with the largest cloud fraction, and the fractional factor is obtained by a multiple product of the clear sky fractions of all the intervening layers between the pressure levels p and p'. In this way, the net LWR heating rate of the layer is the weigthed sum of the contributions from the clear and cloudy skies calculations.

2.2.5 Shortwave Radiative Interactions (SWR)

Contrary to the considerations presented for the LWR flux, the parameterizations for the short wave radiation (SWR) flux must include the angular dependence of the reflection, transmission and absorption of the incident solar light, and its interaction with the atmospheric gases and aerosols, at different wavelengths of light in the visible and near infrared. Some simplifications have been made to reduce the formidable computational task. This section is a description of some aspects of the SWR parameterization in the GLA-AGCM. The work presented follows

closely the description included by Harshvardhan *et al.* [1987], which in turn follows the works by Lacis and Hansen [1974] on the absorption of SWR by water vapor and ozone in the visible wavelengths, on the absorption of infrared solar radiation by water vapor, and on clear sky Rayleigh scattering; by Davies [1982] on the dependence of the scattering of solar radiation by clouds on the zenith angle; by Harshvardhan and Randall [1985] on the estimation of the cloud optical depth; and by King and Harshvardhan [1986] on the directional reflection and transmission of solar radiation.

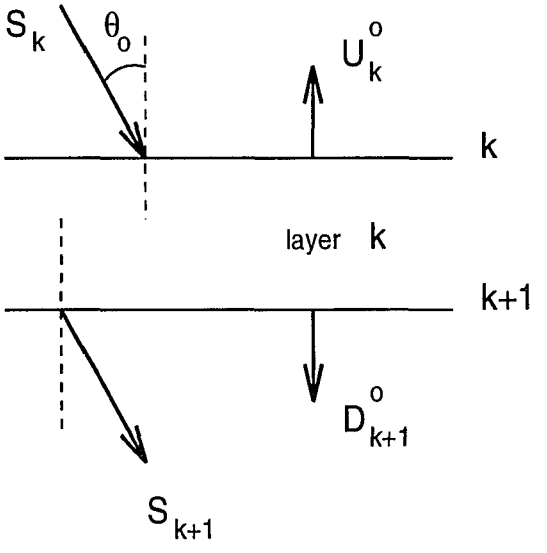

Figure 2.5 – Diffusion of obliquely incident SWR.

Assume that direct solar radiation flux, S_k, is incident upon the atmospheric level k at a zenith angle θ_o, with cosine $\mu_o = \cos\theta_o$ as illustrated in Fig. 2.5. Part of the incident flux is reflected as U_k^o and another is transmitted as D_{k+1}^o. It is assumed that both, U_k^o and D_{k+1}^o are diffuse light described by:

$$U_k^o = \mu_o S_k R_k(\mu_o) \qquad \text{for} \qquad k = 1, 2, \ldots, K+1$$

$$D_{k+1}^o = \mu_o S_k T_k(\mu_o) \qquad \text{for} \qquad k = 1, 2, \ldots, K$$

where $R_k(\mu_o)$ and $T_k(\mu_o)$ are the reflection and transmission functions of solar radiation. For K layers, then R_{K+1} is the **direct incidence surface albedo**; similarly, a **diffuse surface**

albedo, r_{K+1} can be defined. The quantities, R_{K+1} and r_{K+1} are prescribed to the radiative calculation for both, visible ($\lambda < 700$nm) and near infrared ($\lambda > 700$nm), wavelength ranges. The effects of the multiple reflections of the incident solar light are considered in the following iterative procedure. A fraction of the upward flux, U_k^o, is multiply reflected in the layers above the k^{th} level, thus increasing the downward flux of diffuse radiation at level $k+1$ to,

$$D_{k+1}^1 = (D_k^1 + U_k^o C_k) M_k t_k + D_{k+1}^o \qquad \text{for} \qquad k = 1, 2, \ldots, K$$

Here $C_k = r_{k-1} + t_{k-1} C_{k-1} t_{k-1} M_{k-1}$ for $k = 2, 3, \ldots, K+1$ is a **composite reflection coefficient** due to multiple reflections in all layers above the level k; $M_k = (1 - C_k r_k)^{-1}$ for $k = 1, 2, \ldots, K+1$ is a **magnification factor** for multiple reflections from the layers above the k^{th} level. It is assumed that $C_1 = D_1^o = D_1^1 = 0$.

The upward flux of reflected solar radiation is increased by multiple reflections of the downward flux at layers above the level k as,

$$U_k^1 = (D_k^1 r_k + U_k^o) M_k \qquad \text{for} \qquad k = 1, 2, \ldots, K+1$$

The terms r_k and t_k are the **diffuse reflection** and **transmission** coefficients for each layer, respectively. The net fluxes from diffuse light crossing the level k are described as,

$$U_k = U_k^1 + U_{k+1} t_k M_k \qquad \text{for} \qquad k = K, K-1, \ldots, 1$$

$$D_k = D_k^1 + U_k C_k + \mu_o S_k \qquad \text{for} \qquad k = K+1, K, \ldots, 1$$

The upward and downward fluxes are functions of the wavelength of light. A summation of the contributions for the different wavelengths is performed to obtain broadband fluxes, and from these the vertical gradients terms needed to calculate the heating rate profiles, δT_{SWR}.

The previous equations do not include terms associated to the scattering by clouds or the line absorption of solar radiation by gases. The presence of cloud droplets and ice particles of multiple sizes and shapes would introduce modifications in the estimates of the optical depth of the layer due to scattering, and even asymmetry factors in the calculations. In the current version of

the GLA-AGCM the scattering optical depth and the asymmetry factors for the cloud droplets are assumed to be independent of wavelength, within broad wavenumber ranges. The SWR calculation does not use the fractional cloud overlap factors defined before, and the fractional cloud cover of each layer is used to estimate the optical depth. The azimuthal dependence of the surface albedo is perhaps among the greatest uncertainties in the simulation of the net absorption of SWR energy by the atmosphere. Important unknowns in the surface roughness, the differential reflectance of the vegetation types, and the poor resolution of the surface planes of inclination can introduce significant variations of such absorption at the surface boundary.

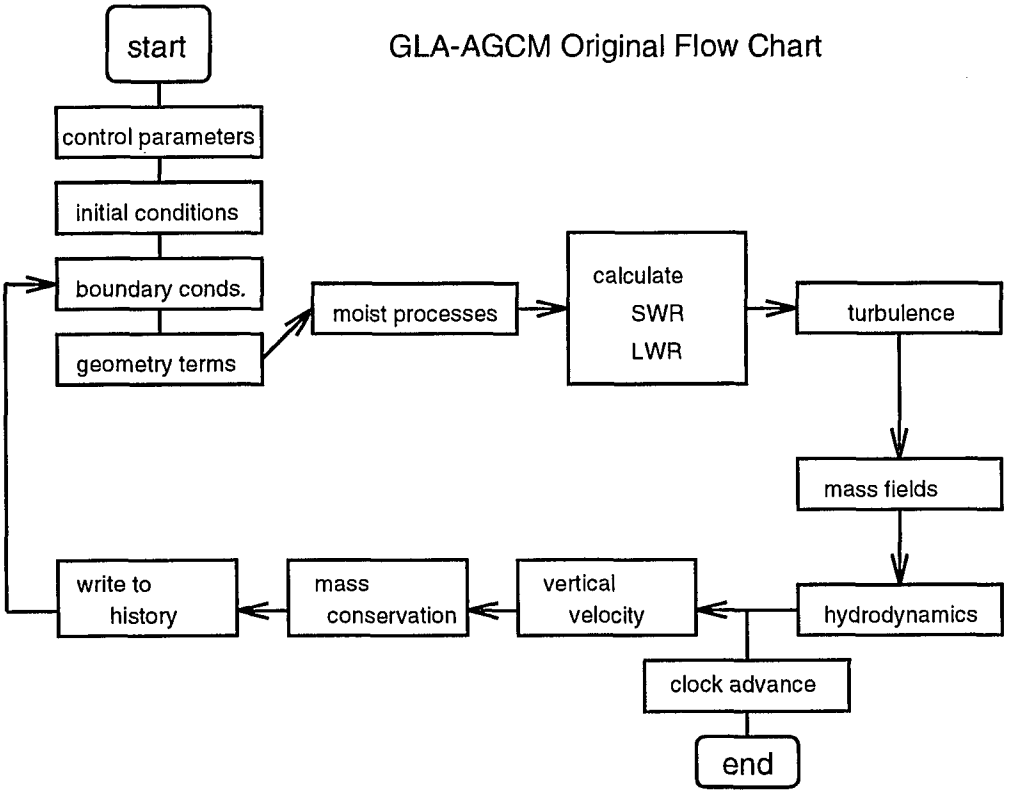

Figure 2.6 – Original GLA–AGCM Program Flow Chart.

2.3 The One Dimensional Simulation (AGCM-1D)

The structure of the GLA-AGCM is illustrated in Fig. 2.6. A typical run of the program

requires: **control parameters** to adjust for, among others, initial and final times, update time steps for the physical forcings, and to select the desired output variables; **initial conditions** for the prognostic variables and the forcing terms; **boundary conditions** for the specification of the surface boundary conditions (normally, seasonally dependent) for temperature, surface height (or topography), surface roughness, land-water-ice classification and albedo. Some of the geometrical terms vary daily or seasonally. Other terms in the figure have been explained in the previous sections. This section is a justification on the use of a one dimensional version of the AGCM in two aspects:

(1) plausibility of a 1D adaptation from the GLA–AGCM;

(2) validity of an AGCM-1D for climate studies of the tropical atmosphere.

This is discussed in terms of the conceptual and practical limitations that a 1D model would impose on the parameterizations used in the model.

The initial profiles of θ and q used for all the experiments are represented in Fig. 2.7. Some preliminary experiments were performed to select the initial profile in θ that would imply the shortest spin-up time. Some of these included an isothermal atmosphere, and a mean profile for tropical latitudes obtained from previous runs of the GLA-3D. For these experiments, the initial profile for θ shown in Fig. 2.7is constructed from a 3 parameter fit to the mean tropical profile. The initial profile for the specific humidity is shown in the same figure, also. This was obtained from a mean tropical profile measured during the GATE experiment. As it is seen from the results of the numerical experiments, even for the low surface evaporation cases, this profile is rather dry.

In the case of the AGCM-1D, the mean fields for θ and q are dynamically determined from the initial conditions, from the effects of radiation (both, LWR and SWR) and cumulus convection, and subject to the imposed boundary conditions of surface temperature and moisture availability. The mean field values for u and v are specified as constant in time and height. As discussed in the section on the turbulence parameterization, the non-vanishing vertical gradient of the mean

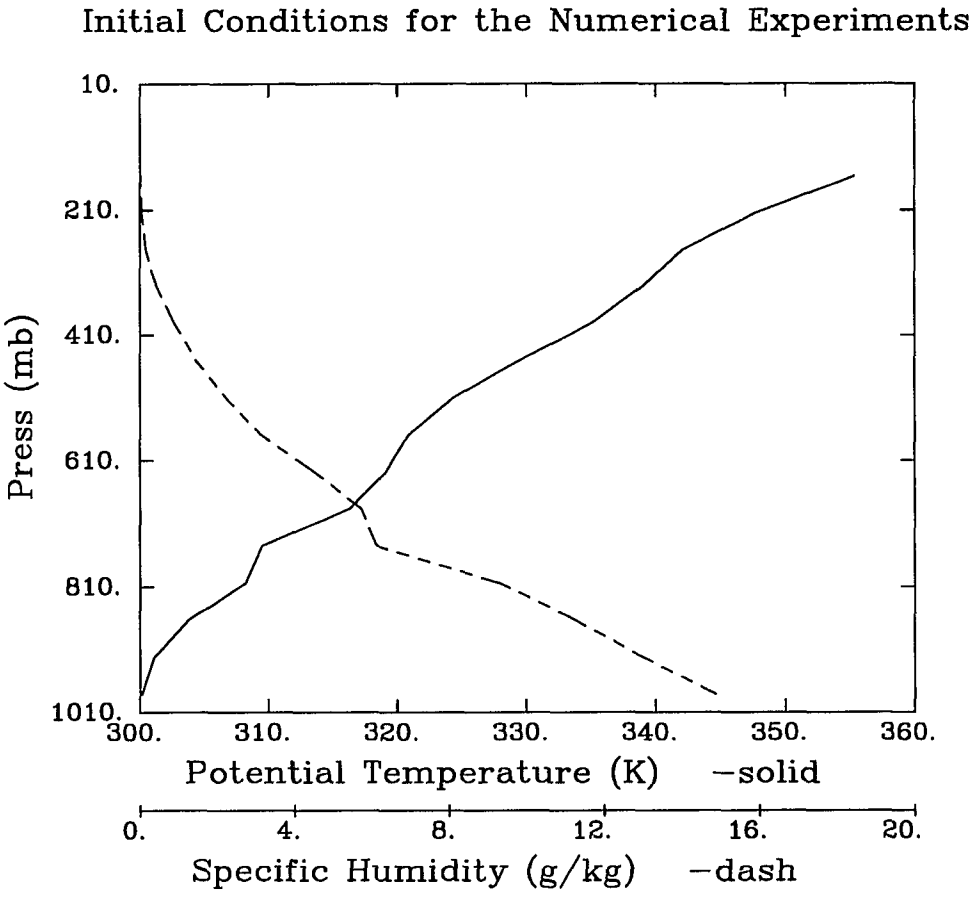

Figure 2.7 – Initial profiles for θ and q used for all the experiments reported here.

θ and q fields is the condition required for the generation of turbulent eddies in all the prognostic variables. In the free atmosphere (*i.e.* not the surface layer) only the deviations from equilibrium values induce turbulent eddies that will tend to restore the local "equilibrium condition". The vertical velocity eddies so generated transport heat (*i.e.* sensible heat transport) and moisture into the free atmosphere.

But the generation of TKE in the Helfand and Labraga scheme relies also on the vertical shear of the horizontal wind. The question is then about the necessity to have a non-vanishing shear of the wind. If values were to be specified to the vertical shear of the mean horizontal

velocity fields, then the correlation term of the vertical and horizontal eddy velocity would induce a reduction of the production term for TKE (since the shear tends to decrease the TKE), and would also reduce the "return to equilibrium" tendencies. Hence, in order as to maintain a strong "return to equilibrium" tendency without the addition of extraneous dissipation factors (or "flux corrections") under the current Helfand and Labraga [1988] turbulent scheme, and in the absence of the divergence and gradient terms on the horizontal wind components, in this AGCM-1D simulation, the suppression of a specified vertical shear is most convenient.

There is the question regarding the fundamental nature of the description of turbulence that the current parameterization implies. As mentioned in Helfand and Labraga [1988], second order closure schemes are meant to describe homogeneous, locally isotropic, three dimensional turbulence. However, the way in which the calculations proceed, and the use of the "boundary layer approximations" preclude the application of any horizontal gradient term.

The radiative parameterizations do not depend on the horizontal transport properties, but on the vertical profiles of θ and q. In that sense, their adaptation to a 1D-AGCM is most natural, but with the constrain that the assumptions regarding the existence of a large enough grid cell where clouds are dealt with in a statistical sense are not violated.

The second point to be discussed is about the validity of using an AGCM–1D for climate studies of the tropical atmosphere. The existence of large expanses of oceanic waters in the Western Equatorial Pacific that remain warmer than 29°C most of the year may well serve to justify the assumption used in these model runs of a constant sea surface temperature 30°C. The large surface evaporation from such waters, as a significant source of atmospheric water vapor partially justify our desire to consider a simplified model where horizontal transport is disregarded.

It is acknowledged that by disregarding horizontal transport, a major source of tropical atmospheric water vapor through the convergence of moist air into the region is not included in the simulation. We could think of a large enough region, encompassing several grid points

of a typical AGCM, where the moisture field is nearly horizontally homogeneous. For such a case, the horizontal advection of water vapor, represented as $\vec{U} \cdot \nabla q$, would have very small contributions to the local value of the specific humidity, even in the presence of strong surface winds. On the other hand, the surface evaporation would be proportional to the wind speed, and non-vanishing. In that restricted context, then, the numerical simulations suggested in this document bear some resemblance to reality, and the experiments can test only the possibility of generating atmospheric variability when the surface evaporation adds moisture to an already uniformly moist troposphere.

The weakness in these arguments come from the non-vanishing mean vertical velocity that the large scale horizontal convergence would imply. Furthermore, a vertical shear of the vertical velocity could imply strong influences on the convective activity. In these terms, the experiments refer to the case of a very moist tropical oceanic atmosphere, where the mean vertical velocity of the overall area is zero, and where a large field of clouds of many different heights can induce climate variability by interaction with the radiation fields. The mean wind over this area is assumed homogeneous and constant in time. How would such wind, moisture and surface temperature conditions be maintained is a concern for another research project, of great importance in the current trends of atmospheric-ocean studies.

There is the concern about the use of a 1D model as opposed to a 3D treatment of this problem. It has been mentioned that the problem of a localized strengthening of the intraseasonal oscillations is in itself a justification for the 1D approach. One can envision an additional reason for it: in a hydrostatic model vertical velocities are generated from a non-vanishing wind divergence. Although unproven, in the absence of a known restoring force to balance these mean vertical motions, the convective perturbations would be distorted beyond what turbulence balance could achieve; something that would then require the use of extraneous terms to prevent a runaway climate experiment. Furthermore, horizontal transport (*i.e.*, convergence and advection) and its representation in terms of finite differences, would introduce temporal and spatial

perturbations, which can be unrelated to the localized strengthening to be studied. Based on these terms it seems also reasonable to use a 1D version of an AGCM to study this phenomena.

Chapter 3.

The numerical experiments

Several conditions are investigated using the 1-D model described in section 2.3. Among these are the effects of the prescribed seasonal and diurnal solar forcing, and the effects of the prescribed surface wind in the absence of wind convergence.

Table 3.1

Prescribed conditions for the experiments reported in this work

Experiment	SST (°C)	u (m/s)	Cyclic solar forcing
MR35	30	3.5	*no*
MR36	30	12	*no*
MR37	30	3.5	*yes*
MR38	30	12	*yes*

The Table 3.1 summarizes the conditions that were included in the numerical experiments to be discussed in this chapter. The experiments are essentially a study of the interaction between atmospheric moisture and local radiative processes. There were a large number of preliminary

attempts during the modification phase of the three dimensional (3D) version of the GLA-AGCM into the one dimensional (1D) version of the model, and that served to define the proper form of the datasets used in the experiments, also. These preliminary attempts are not described in this document, but the following paragraphs present briefly some of the ideas involved.

The simulations to be described required the specification of the temperature at the surface boundary as a function of time; an initial specification of the temperature, specific humidity, and pressure levels distribution, atmospheric forcing terms ($\delta T_{LWR}, \delta T_{SWR}, \delta T_{trb}, \delta T_{mst}, \delta q_{trb}, \delta q_{mst}$), and turbulent kinetic energy, as a function of pressure.

The standard procedure for the specification of the surface temperature in an isolated AGCM is to use a climatology, and then to interpolate in time to obtain the instantaneous values for a particular time of the year. For a numerical experiment in which the focus is the generation of intraseasonal variability over an oceanic point with conditions similar to the Equatorial Western Pacific, and because the purpose is to study the stationary nature of such climate variability, it is opted for a warm oceanic surface with a constant temperature at the boundary of 30°C. It is expected that the lack of temporal variability in the boundary temperature would not introduce additional time scales to the simulation.

The initial temperature profile was selected from a climatologically determined set of values, as explained in the previous chapter. As it is seen from any of the θ_{250} figures, there is an adjustment phase (usually called **spin-up time**) at the beginning of each simulation.

For the simulation of a tropical oceanic atmospheric environment, the initial specific humidity profile was first selected from measurements of the GATE (Global Atmospheric Research Program - Atlantic Tropical Experiment; C.H. Sui, personal communication) experiment. This initial moisture profile was rather dry, even for the low surface evaporation case, and after the spin-up time the specific humidity profile with the longest residence time was heavier in water vapor. Slightly different profiles were tried in addition, and the final selection is one that closely resembles an exponentially decreasing specific humidity with height. The criteria used for the selection was,

again, a shorter spin-up time for the simulation.

Hence, for the prognostic variables, θ and q, the initial profiles seem to be too warm and dry in the upper troposphere, and too cool and dry for the lower troposphere. The turbulence and moisture forcing terms for both, θ and q, are given vanishing values initially. In that sense, the presence of a sustained surface evaporation feeding water vapor to the lowest levels of the troposphere is expected to induce some convective activity in the lowest part of the column, which in turn will slowly adjust $q(z)$ to the proper level. The initial profiles for the radiative heating terms are selected from Ridgway *et al.*(1991). This last specification is, perhaps, among the most important factors in reducing the spin-up time for these simulations of the tropical climate. The significance of this reduction is a problem of a different kind to be studied as another research project.

The surface layer is assumed at a constant temperature in all the experiments, as if it were to have an infinite heat capacity. The surface fluxes of short and longwave radiation vary as a function of time, because of the varying conditions of cloud cover and precipitable water. These fluxes are shown in MR37 and Fig. 3.2 for the experiments with low and high surface evaporation, respectively. The weak seasonal variation (about 10%) of the surface solar flux typical of tropical latitudes can be seen in the third panel from the bottom in both figures. The lower two panels show the fluxes for the cases in which there is no cyclic solar forcing. Several aspects are worth mentioning. The radiative effects at the surface due to cloud shielding are hidden by the diurnal and seasonal variability of the solar fluxes. In the absence of a cyclic solar forcing, the shortwave surface flux is slightly enhanced during periods of strong convective activity. This is probably due to the fact that tall cumulus clouds tend to supress the existence of a lower layer of clouds, while covering a smaller total cross sectional area. The longwave surface flux is also consistently higher. The sudden transitions into which both LWR and SWR surface fluxes acquire sustained higher values are refered as "strong cooling episodes", although the surface signature of such transitions is one of enhanced surface fluxes.

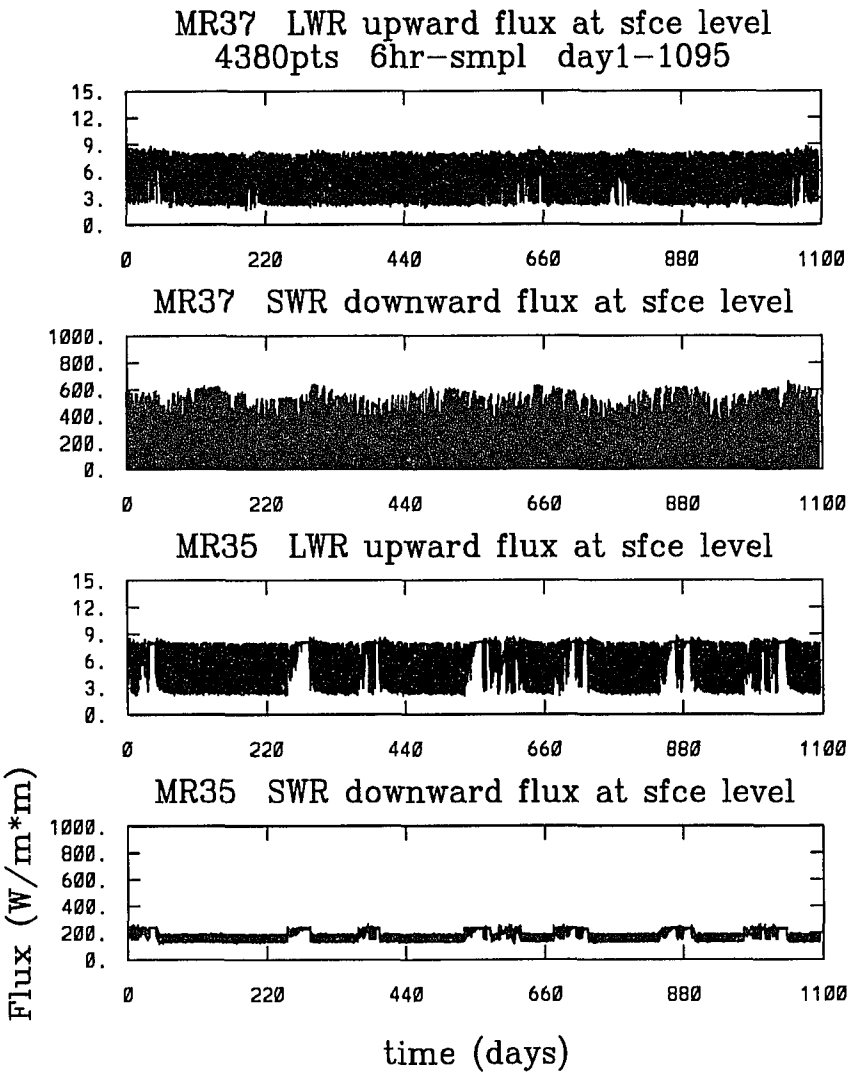

Figure 3.1 – Surface radiative fluxes for the low evaporation cases. The top two panels are for the experiment with cyclic solar forcing, while the lower two panels are for the experiment without cyclic solar forcing.

The general description of the experiments will follow these guidelines: (1) a description of the relevant features from the time series of the upper troposphere, at the 250 mb level, for the potential temperature, θ_{250}, the specific humidity, q_{250}, the long and short wave heating rates, δT_{250}^{LWR} and δT_{250}^{SWR}, the turbulent, δQ_{250}^{trb}, and moist, δQ_{250}^{mst}, forcing terms on q_{250}; (2) a description of the relevant features from the time series for θ_{950} and q_{950} at the 950 mb level, and

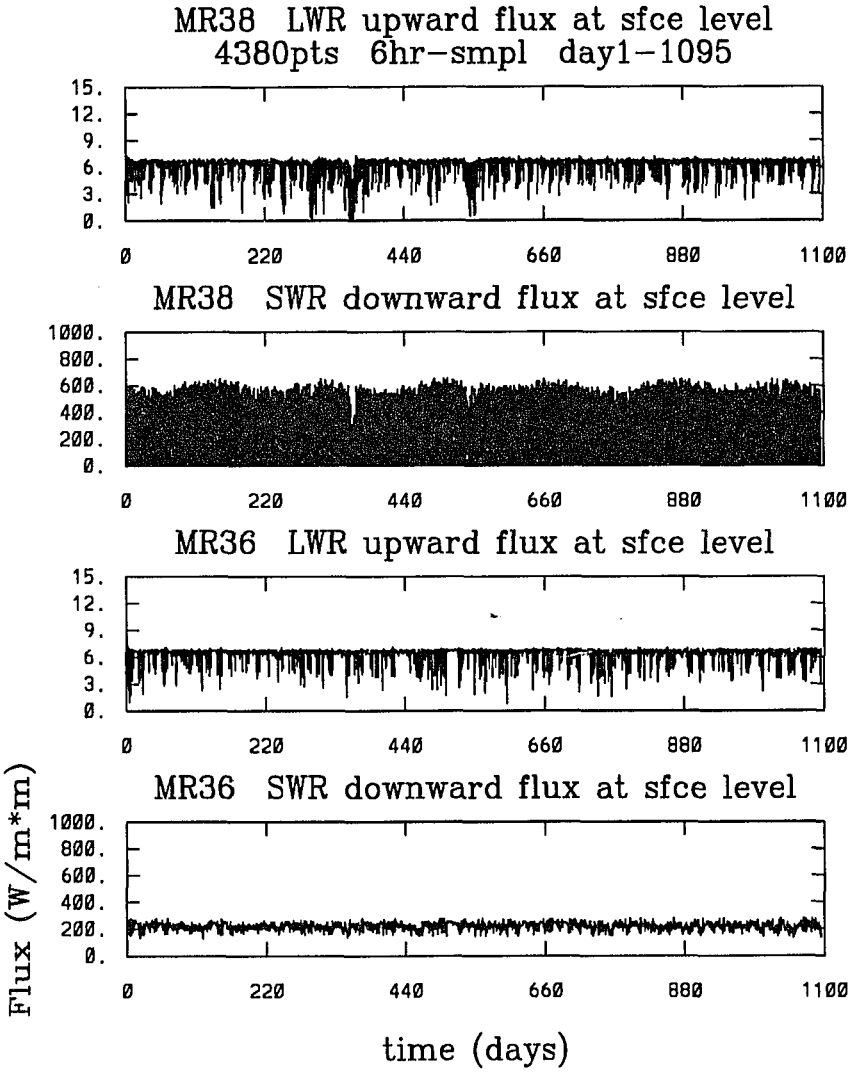

Figure 3.2 – Surface radiative fluxes for the high evaporation cases. The top two panels are for the experiment with cyclic solar forcing, while the lower two panels are for the experiment without cyclic solar forcing.

at the surface layer for the evaporation, E_v, the precipitation of stratiform, P_{strat}, and convective, P_{conv}, types. The last sections of the chapter are a discussion of the most likely states of the vertical profiles of the prognostic variables and the respective forcing terms, for the low and high surface evaporation cases.

3.1.0 The numerical experiment MR37

The following conditions describe the numerical experiment MR37. The temperature at the surface boundary is kept constant at 30°C for a simulated atmosphere over an oceanic grid point at the geographical location of $(180°W, 2°N)$. The upper air horizontal wind is kept at a uniform value of 3.5 m/s for each component throughout the troposphere. The experiment included a simulation of the diurnal and seasonal cycles of the insolation at the top of the troposphere. The insolation is expressed as $S = S_0 \cos(\psi)/R_a^2$, where S_0 is the solar constant, ψ is the zenith angle, and R_a is the ratio of the Earth-Sun distance to the length of the Earth's orbit semimajor axis. The zenith angle is a function of the time of the day, the longitude, and the latitude of the geographical point for which the angle is calculated. The R_a is a function of the calendar day and the eccentricity of the Earth's orbit.

3.1.1 The upper troposphere

Fig. 3.3 (top) illustrates the time series for the potential temperature at 250 mb, θ_{250}. This figure serves to identify some common properties of the results from all the simulations. The relevant features of this figure are: (i) the mean value is about 337 K and no climate drift is observed during the 1100 day of the simulation; (ii) the existence of large fluctuations, of the order of 10 K, between a warmer upper troposphere at 339 K and a colder upper troposphere at 330 K; (iii) the warmer climate has a longer residence time than the colder climate; (iv) there are smaller magnitude fluctuations with a time scale of about 20 to 40 days; (v) the appearance of a seasonal modulation on the 20 to 40 day time scale phenomena; (vi) the existence of a short time scale variability of about 1 day.

Fig. 3.3 (bottom) illustrates the time series for the specific humidity of the upper troposphere, q_{250}. The most relevant features of this figure are: (i) the warmer regime is also a moist regime, with a mean specific humidity of 0.30 g/kg, while the cooler regime is drier with a mean of 0.12 g/kg; (ii) the variability of the moist regime is in the range of 0.25 to 0.35 g/kg; (iii) the existence of a 20 to 40 day modulation with a peak-to-peak amplitude of 0.1 g/kg on the short time scale variability, during the warm and moist regime; (iv) the cooler and drier regime has a smaller

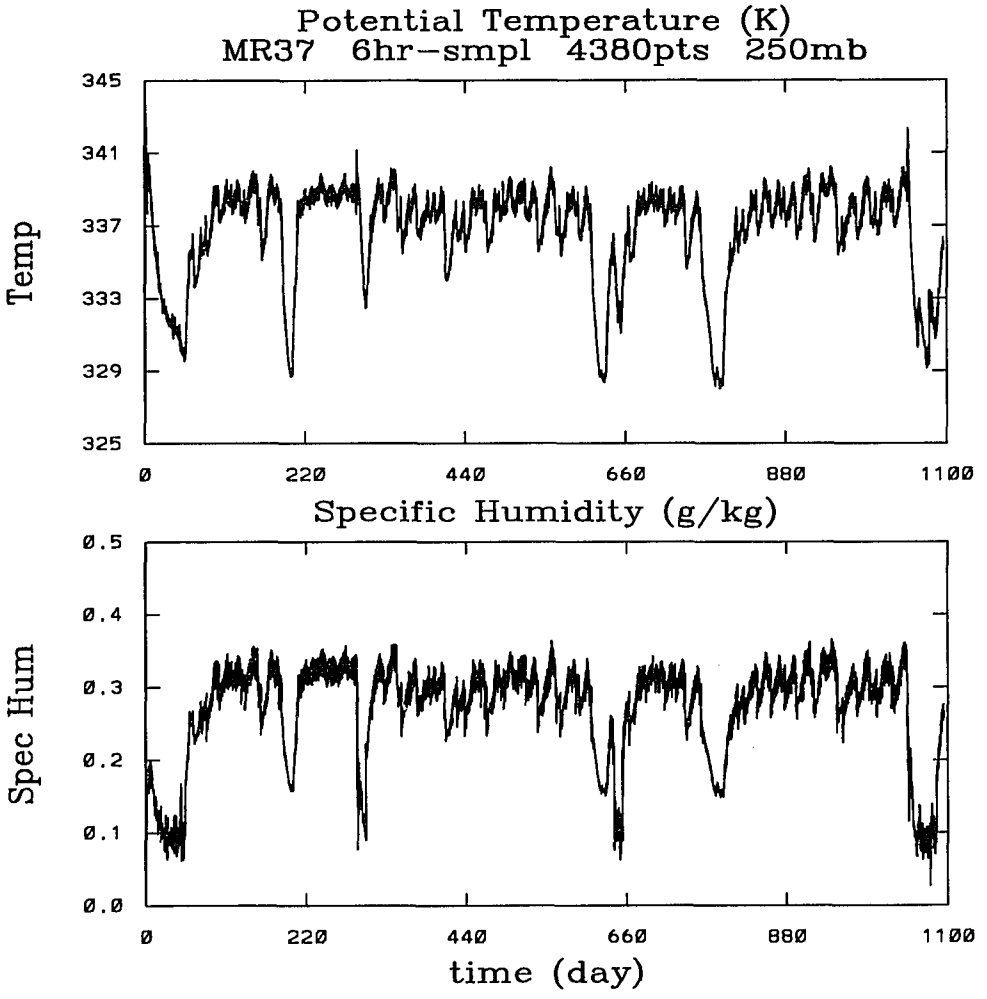

Figure 3.3 – θ and q at 250 mb for MR37. Time series for the potential temperature (upper panel) and the specific humidity (lower panel) for the upper troposphere in the low surface evaporation experiment with cyclic solar forcing.

variability during either transitions from the warmer regime; (v) the end of the cooler regime is characterized by a slow build-up in q_{250}.

Fig. 3.4 (top) is a plot of the time series for the turbulent forcing term on q_{250}, δQ_{250}^{trb}. The most relevant features of this figure are: (i) water vapor is being pumped in at all times into this layer by the turbulent processes; (ii) the warmer regime has a larger variability in the short time scale, with a range of 0.0 to 0.28 g/kg/day; (iii) δQ_{250}^{trb} decreases monotonically from 0.13 to 0.08

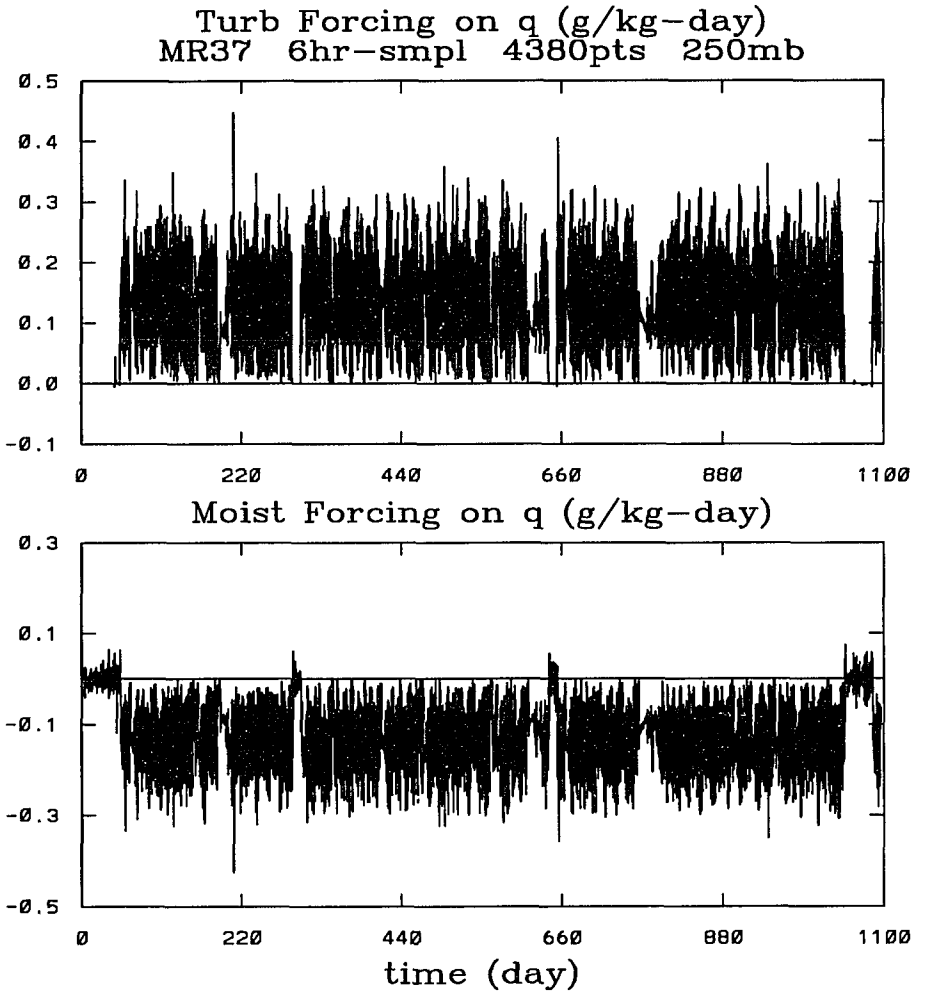

Figure 3.4 – δQ_{trb} and δQ_{mst} at 250 mb for MR37.

g/kg/day in the colder regime; (iv) there are some indications of the 20 to 40 day modulation; (v) during some of the cold events, δQ_{250}^{trb} vanished.

Fig. 3.4 (bottom) illustrates the time series for the moist processes forcing term on the specific humidity, δQ_{250}^{mst}. The most relevant features of this figure are: (i) the moist processes deplete water vapor from the layer during the warm regime; (ii) during the warm regime the small time scale variability has a range of 0.0 to -0.30 g/kg/day; (iii) during the cold events and in the absence of turbulent transport of water vapor into the layer, then $\delta Q_{250}^{mst} \sim 0.0$; (iv) for those nonvanishing values of δQ_{250}^{trb} during the cold regime, the variation in δQ_{250}^{mst} is nearly

monotonic in the range of -0.10 to -0.05 g/kg/day.

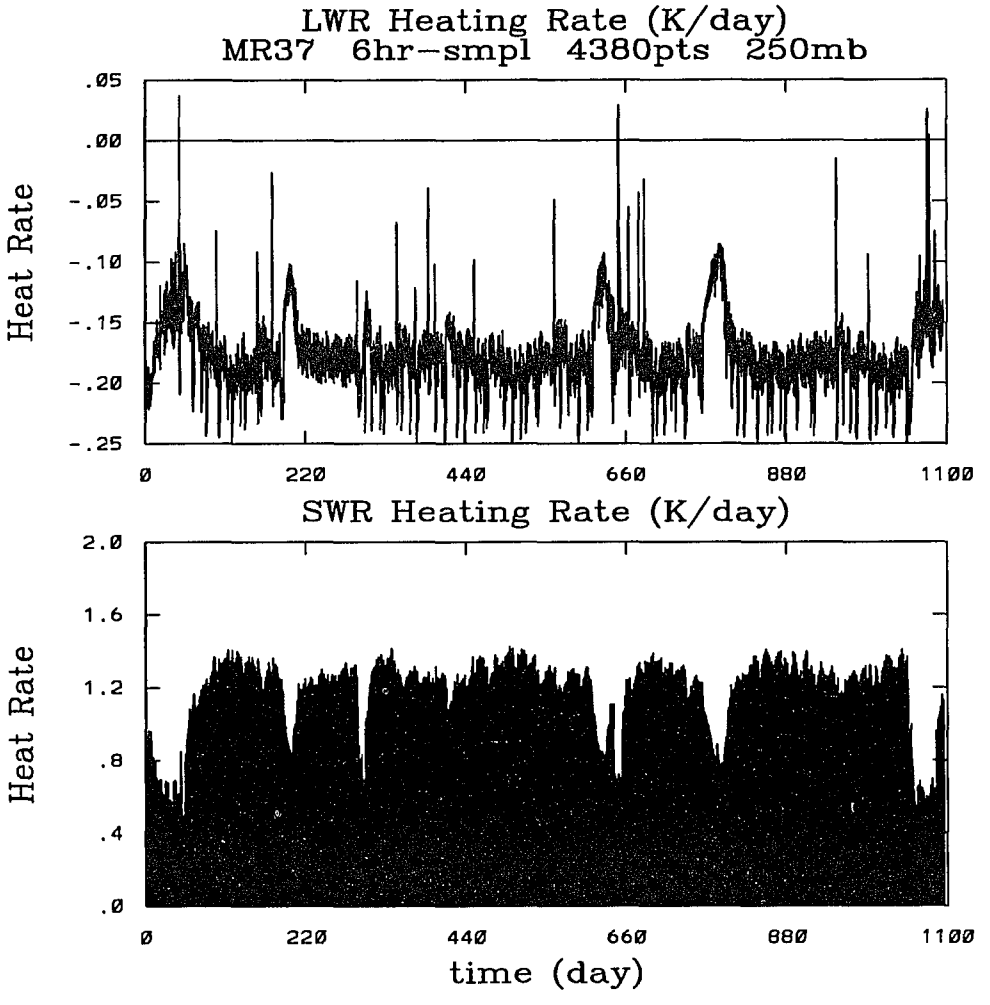

Figure 3.5 – δT_{LWR} and δT_{SWR} at 250 mb for MR37.

Fig. 3.5 (top) illustrates the time series for the long wave heating rate, δT_{250}^{LWR}. The most relevant features are: (i) the 250 mb layer almost always cools off by LWR; (ii) the longest residence time corresponds to a range of -0.175 ± 0.025 K/day during the warm regime; (iii) the long wave radiative forcing decreases to -0.1 K/day with much lesser variability during the colder regime; (iv) the 20 to 40 day modulation can be seen as stronger cooling spikes in the δT_{250}^{LWR} trace. The spikes of weaker LWR cooling rate occur for the higher temperatures in the layer, while the spikes of stronger LWR cooling rates occur at the stronger cooling trends; that is, the

simulated upper troposphere cools off radiatively, while it dries out.

Fig. 3.5 (bottom) illustrates the time series for the short wave heating rate, δT_{250}^{SWR}. The most relevant features of this figure are: (i) the daily variation of δT_{250}^{SWR} is in the range of 0.0 to 1.3 K/day during the warm regime; (ii) the seasonal cycle and the phase of the cooling events seem to be unrelated; (iii) the variation of δT_{250}^{SWR} during the colder events is in the range of 0.0 to 0.8 K/day. It is observed that the SWR heating rate has a lesser amplitude for the drier episodes, and larger amplitudes otherwise. Hence, during the cooler regime the LWR cooling is reduced at the 250 mb level, but the SWR heating, δT_{250}^{SWR}, is also reduced.

3.1.2 The lower troposphere

Fig. 3.6 (top) illustrates the time series for θ_{950}. The most relevant features of this figure are: (i) the warm regime's short time scale variability is reduced to about 1.4 K in amplitude; (ii) the cooler regime appears as a monotonically decreasing θ_{950}, but still within the variability range enclosed by the warm regime; (iii) neither, the seasonal nor the 20 to 40 day modulations can be recognized.

Fig. 3.6 (bottom) illustrates the time series for q_{950}. The most relevant features of this figure are: (i) the short time scale variability for q_{950} is predominant in the range of 14 to 18 g/kg during the warm regime; (ii) the cooler regime is characterized by short time scale variability with reduced amplitude, which is less than 0.5 g/kg at about 17 g/kg; (iii) no seasonal modulation is apparent from the time series; (iv) the 20 to 40 day modulation is barely distinguishable as spikes of 0.2 g/kg amplitude over the maximum small time scale variability.

Fig. 3.7 illustrates the time series of the stratiform (top) and convective (bottom) precipitation types, respectively. The most relevant features of these plots are: (i) small values for the stratiform precipitation of at most 0.5 mm/day during the warm regime; (ii) apparently, there is no stratiform precipitation during the cooler regime; (iii) the convective precipitation varies in the 0 to 5 mm/day range during the warm regime, with a dominant small time scale; (iv)

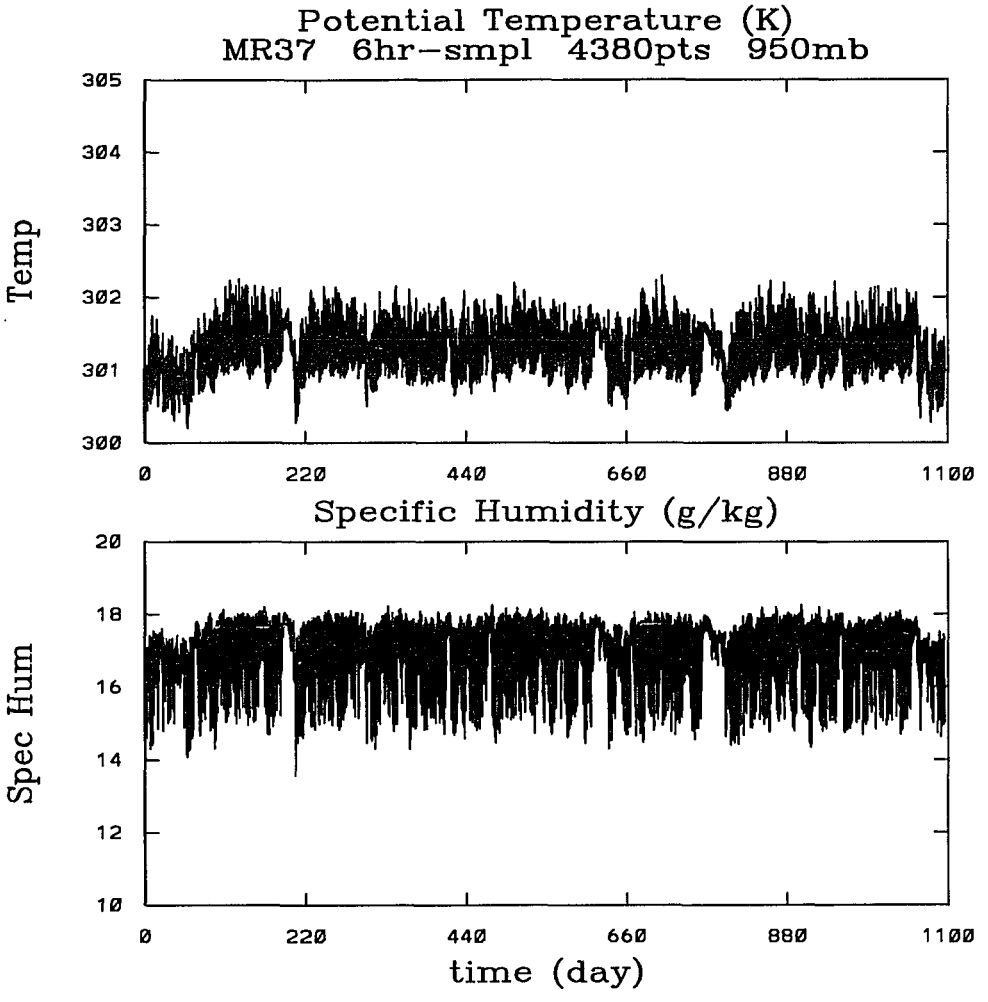

Figure 3.6 – θ and q at 950 mb for MR37. Time series at the lower troposphere for the experiment with low surface evaporation and cyclic solar forcing.

during the cooler regime the convective precipitation has an apparently narrower range of 0.5 to 1.5 mm/day.

Fig. 3.8 (bottom) illustrates the time series for the surface evaporation. The most relevant features of this figure are: (i) the largest variability occurs during the warm regime in the range of 0.95 to 1.45 mm/day; (ii) the cooler regime has an increasing surface evaporation with a smaller variability in the range of 0.95 to 1.1 mm/day.

3.2.0 The numerical experiment MR35

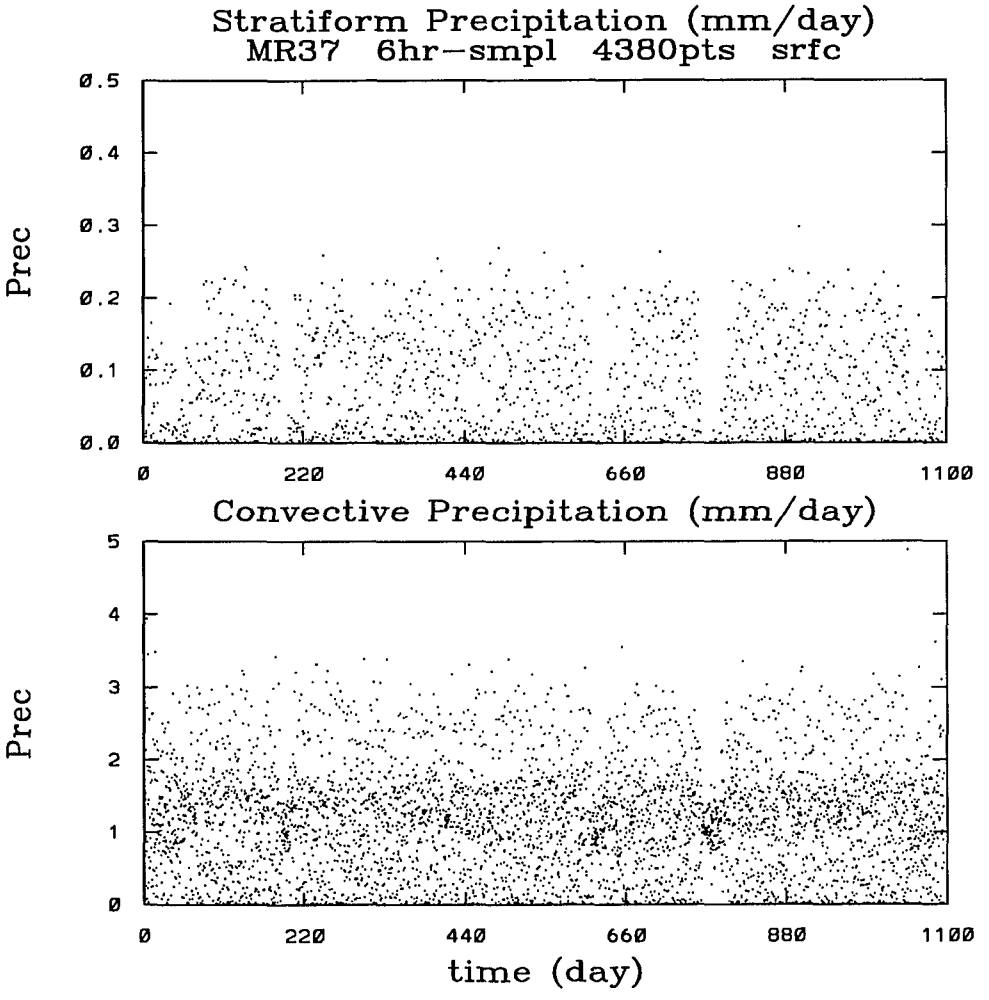

Figure 3.7 – Stratiform and convective precipitation for MR37. The precipitation values refer to the mean of a 6 hours sampling period.

Some general observations are deduced from the results of the numerical experiment MR37, among which there are: (i) the simulated troposphere has strong non-periodic fluctuations between a warm and moist regime and a cooler and dry regime; (ii) the time series for θ and q have some predominant time scales for the warm and moist regime in the ranges of 1 to 2 and 20 to 40 days; (iii) during the cool and dry regime the predominant time scale is in the range of 6 to 8 hours; (iv) the warm and moist regime has the longest residence time for the case of a prescribed warm surface temperature of 30°C and a prescribed upper air wind of 3.5 m/s

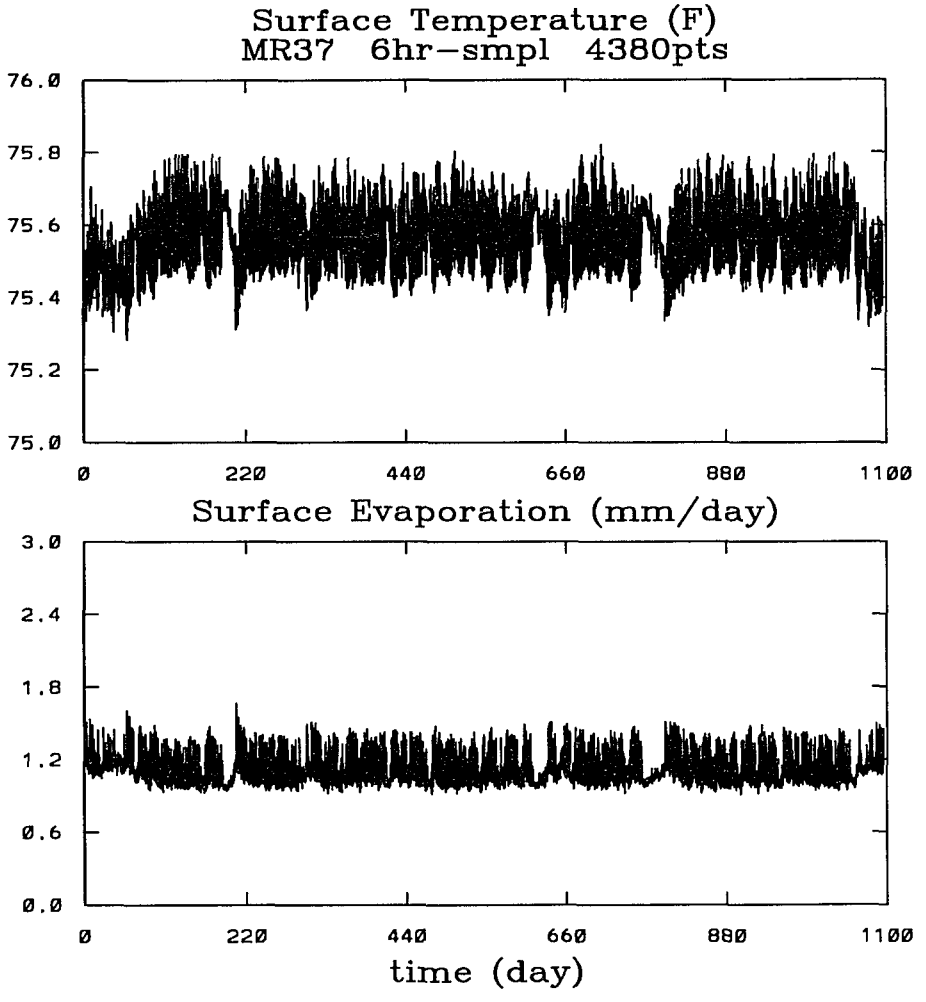

Figure 3.8 – Surface air temperature and evaporation for MR37. Values are similarly sampled as in the previous figure.

(*i.e.* low surface evaporation); (v) the simulated seasonal cycle is not a strong modulating factor on the short time scale variability during the warm regime, for an equatorial oceanic horizontally isolated atmospheric column; (vi) the phase of the fluctuations between regimes seems unrelated to the seasonal cycle.

Several questions can be posed from these results. One of them is related to the role of the diurnal cycle in generating short term fluctuations in the lower troposphere; another, to its role in pumping moisture into the upper troposphere. The third one is related to the seasonal

modulation of the transitions between regimes, and in particular, to a possible phase relationship between the seasonal cycle and the cooling events. To answer these questions the approach followed is to supress the diurnal and seasonal variations of the prescribed solar insolation at the top of the troposphere. This will identify whether the relevant transitions are induced by the cyclic radiative forcing, or whether they are determined by other forcing terms in the vertical column. Although the suppression of the cyclic solar forcing was done on several steps, only the final numerical experiment is presented.

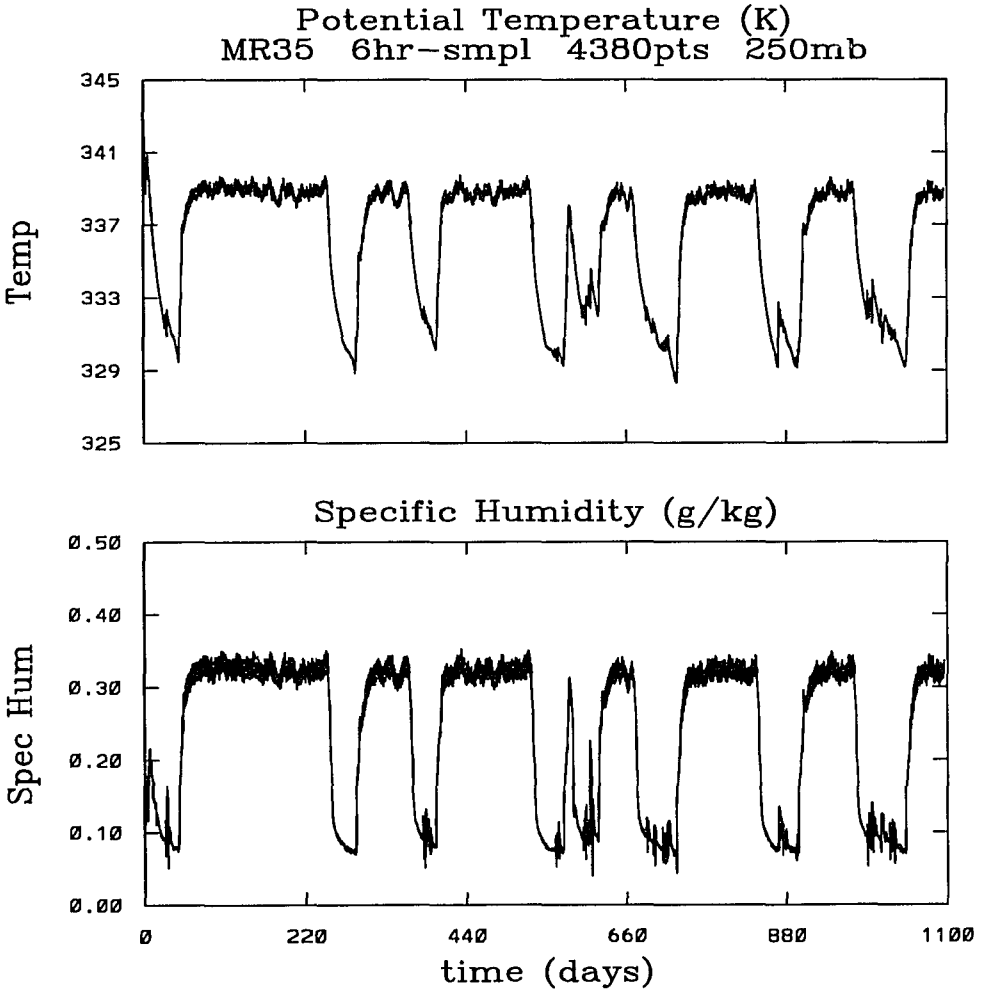

Figure 3.9 – θ and q at 250 mb for MR35. Time series at the upper troposphere for the experiment with low surface evaporation and no cyclic solar forcing.

The numerical simulation MR35 is designed to clarify the role that the seasonal and diurnal cycles played in the generation of the time scales mentioned above, and in the transitions between the cool and warm regimes. The insolation at the top of the troposphere is fixed to be a constant equivalent to the mean daily solar insolation at the Spring Equinox. It is assumed that at the Spring Equinox the sun shines straight ahead over the equatorial belt, and that the daily cycle of the insolation is the half positive part of a cosine during the day and zero at night. The mean daily insolation is then given by S_0/π. An oceanic surface condition is assumed, as for MR37, and the sea surface temperature is fixed at 30°C. The upper air winds are also specified at 3.5 m/s. The presentation of the results follow the scheme summarized in section 3.0.0.

3.2.1 The upper troposphere

Fig. 3.9 (top) is a plot of the time series for the potential temperature at the 250 mb level, θ_{250}. The most relevant features of this figure are: (i) the upper troposphere fluctuates between a warm regime at about 339 K and a cooler regime at about 330 K; (ii) the transition between regimes does not occur at regular intervals; (iii) no discernible trends or climate drifts occur during the 1100 days of the simulation; (iv) the variability in the warm regime is dominated by the 1 to 2 day time scale, and a modulation of about 20 to 40 day is more clearly visible than for the experiment MR37; (v) the cooler regime is characterized by a monotonic decrease in the temperature and a reduced amplitude of the short time scales.

Fig. 3.9 (bottom) is a plot of the time series for the specific humidity at 250 mb, q_{250}. The most relevant features of this figure are: (i) the warm regime is a moist regime with a specific humidity of about 0.33 g/kg, while the cooler regime has a specific humidity of about 0.10 g/kg; (ii) the moist regime has a longer residence time than the cooler regime; (iii) the variability in the moist regime is dominated by short time scales of about 1 to 2 and 20 to 40 days, within the range of 0.30 to 0.34 g/kg; (iv) the decay into the drier regime seems quicker than the recovery phase into the moist regime. It should be pointed out that in terms of the variables θ_{250} and q_{250} the time series from the two experiments MR35 and MR37 are very similar.

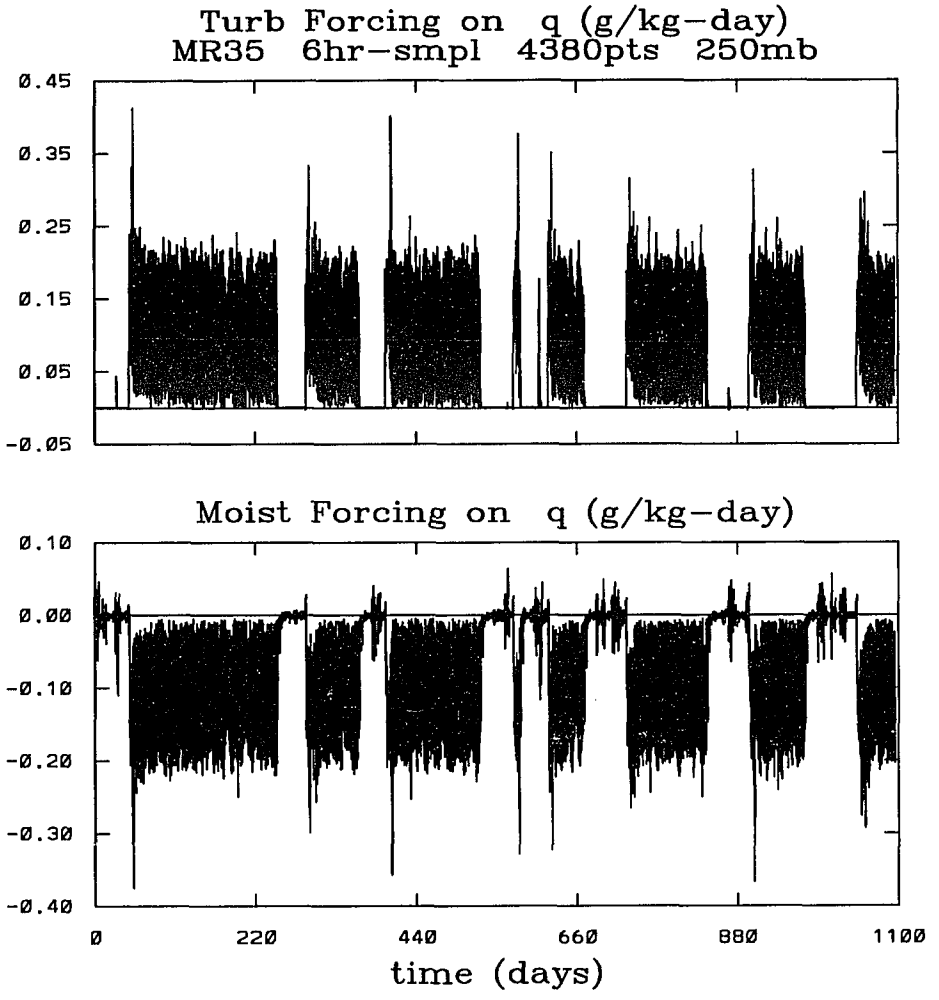

Figure 3.10 – δQ_{trb} and δQ_{mst} at 250 mb for MR35.

Fig. 3.10 (top) is a plot of the turbulent forcing term on the specific humidity, δQ^{trb}_{250}. The most relevant features of this figure are: (i) turbulence processes provide water vapor to the upper troposphere at a rate of about 0.12 g/kg/day during the warm regime; (ii) during the cold regime, the turbulence processes do not pump moisture to the upper layers; (iii) the final phase of the transition from the cold regime to the warmer regime is a sudden injection of water vapor by turbulence.

Fig. 3.10 (bottom) is a plot of the moist processes forcing term on the specific humidity, δQ^{mst}_{250}. The most relevant features of this figure are: (i) moist processes deplete water vapor from

the layer at a rate of about 0.12 g/kg/day during the warm regime; (ii) in the cooler regime, there is depletion and pumping of moisture into the layer through moist proceses, but in rather small amounts; (iii) the final transitional phase into the warmer regime is characterized by a stronger input of water vapor by moist processes. This figure indicates that depositions and reductions of water vapor during the colder regime in the upper troposphere are convectively dominated.

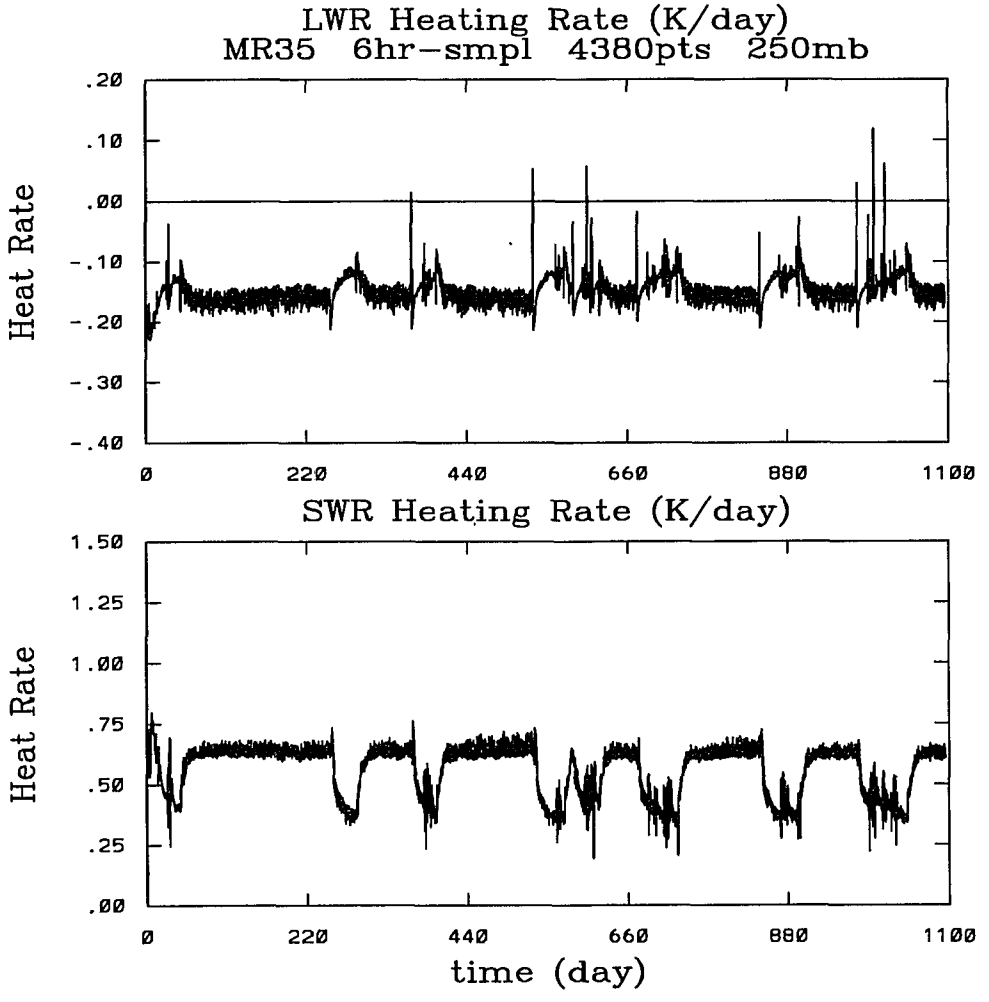

Figure 3.11 – δT_{LWR} and δT_{SWR} at 250 mb for MR35.

Fig. 3.11 (top) is a plot of the time series for the long wave radiative heating rate, δT_{250}^{LWR}. The most relevant features of this figure are: (i) most of the time the upper troposphere cools off by LWR; (ii) the warm regime cools off at a rate of about 0.15 K/day, which is higher than

the cooling rate for the cool regime of about 0.12 K/day; (iii) the variability for both warm and cool regime is about 0.03 K/day; (iv) no modulation of the 20 to 40 time scales is observed in δT_{250}^{LWR}.

Fig. 3.11 (bottom) is a plot of the time series for the short wave radiative heating rate, δT_{250}^{SWR}. The most relevant features of this figure are: (i) the SWR heating rate during the warm regime varies in the range of 0.60 to 0.70 K/day, while during the cooler regime it varies in the range of 0.35 to 0.50 K/day; (ii) a weak modulation in the 20 to 40 day time scale is recognized for the warm regime.

The simulated upper troposphere has similar features in the time series for the experiments with and without diurnal and seasonal forcings. The main features are the transitions between two regimes characterized by different temperatures ranges and moisture contents, and the existence of preferential long term (but nevertheless weak) time scales for the variability during the warmer regime. The colder regime seems to be intrinsically dominated by sustained moisture exchange processes in the upper troposphere. Radiatively, the upper troposphere cools off less in the infrared, but it also absorbs less visible light because of the reduced water vapor content.

3.2.2 The surface layer

Fig. 3.12 (top) is a plot for the time series of θ_{950}. The most relevant features of this figure are: (i) the warmer regime is defined by a mean temperature of about 301.3 K, with a variability in the range of 300.8 to 301.7 K, and time scales in the 1 to 2 day range; (ii) the cool regime is characterized by nearly monotonic reductions in the temperature, within the range of 301.8 to 301 K, and rapid fluctuations of about 0.3 K in the 300.7 K level.

Fig. 3.12 (bottom) is a plot of the time series for q_{950}. The most relevant features of this figure are: (i) the cooler regime has a very small variability, while the system's specific humidity decreases in the range of 18 to 17 g/kg; (ii) the variability of q_{950} during the warm regime is dominated by the short time scale of 1 to 2 day, and in the range of 14.5 to 18 g/kg; (iii) there

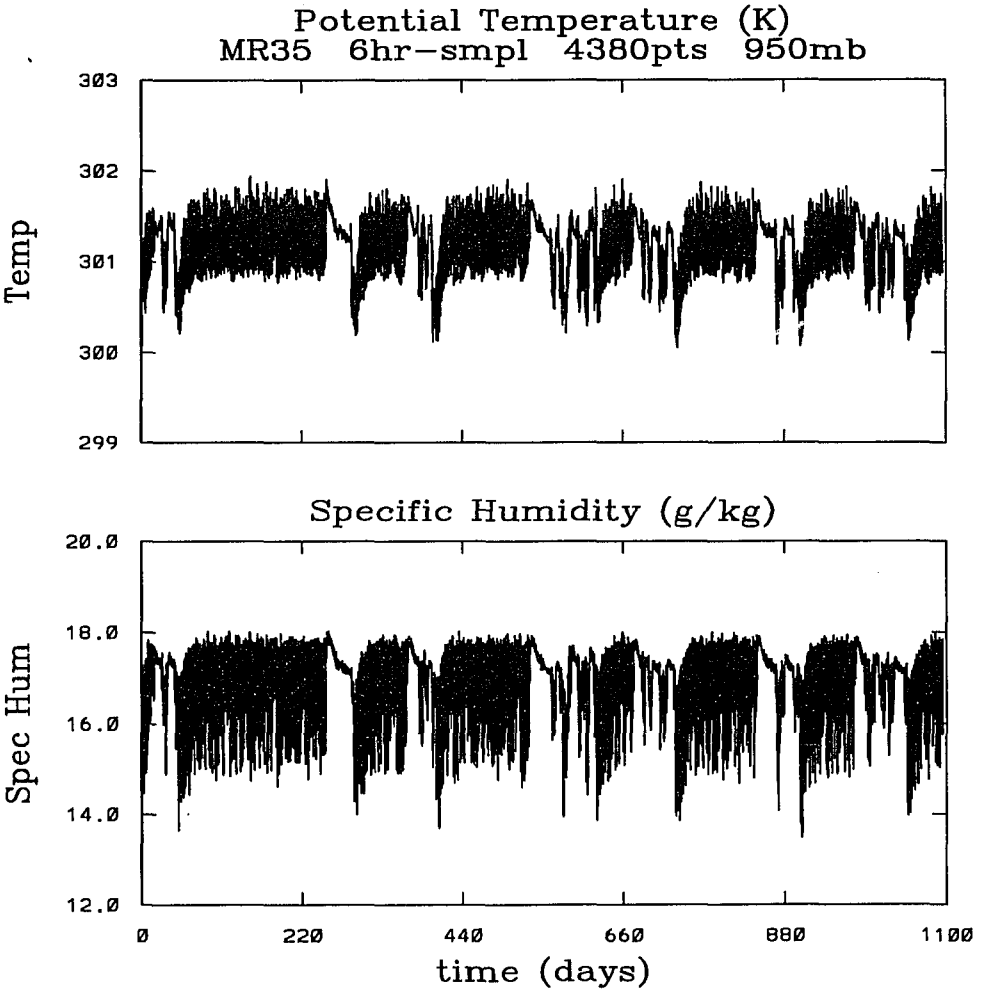

Figure 3.12 – θ and q at 950 mb for MR35. Time series at the lower troposphere for the experiment with low surface evaporation and no cyclic solar forcing.

are no visible climate drifts for the 1100 days of the simulation. An apparent slow build-up of water vapor is recognizable at the end of each dry regime.

Fig. 3.13 are plots of the time series for the stratiform (top) and convective (bottom) precipitation types. The most relevant features of these figures are: (i) there is no stratiform precipitation during the cooler regime; (ii) during the warm regime the range of the stratiform precipitation is 0.0 to 0.4 mm/day, and the range for the convective type is 0.0 to 4.0 mm/day; (iii) the convective precipitation varied in the range of 0.8 to 1.5 mm/day during the cooler

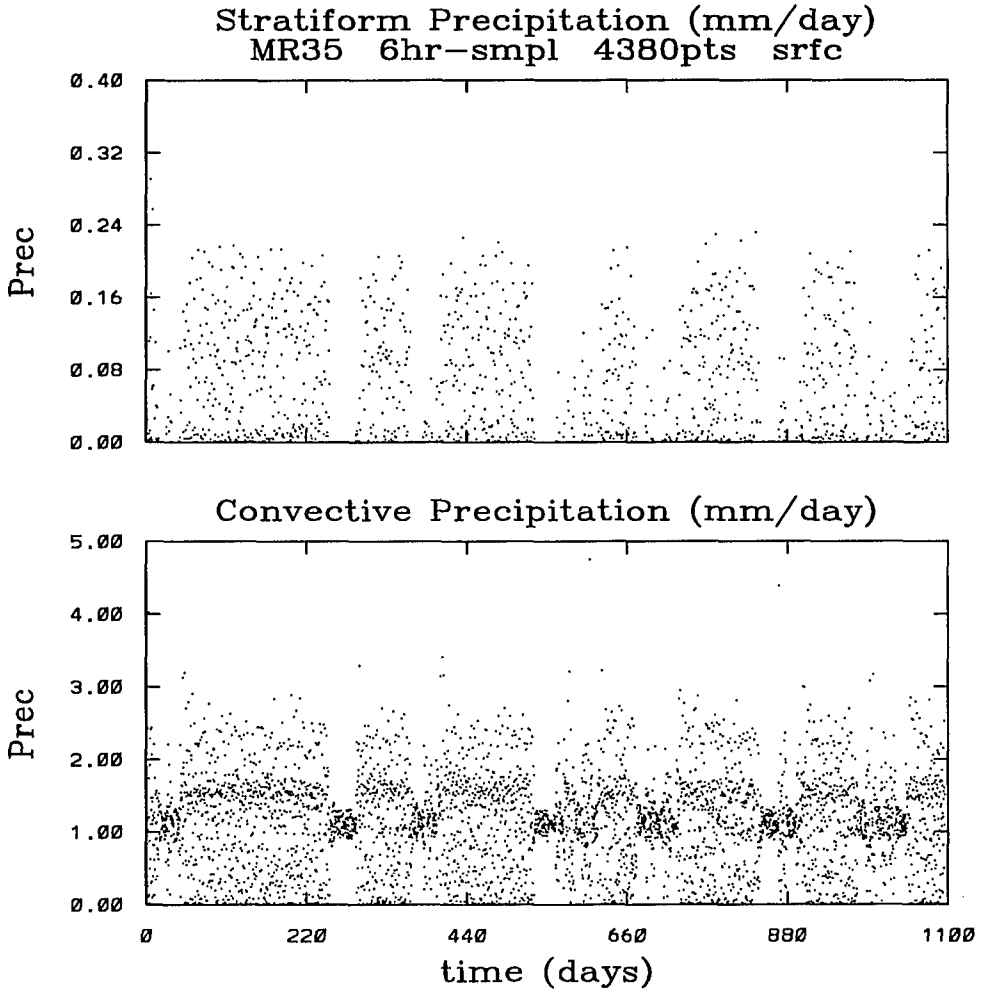

Figure 3.13 – Stratiform and convective precipitation for MR35. The precipitation values are an average for a 6 hour period.

regime. This feature of the convective precipitation type is hinted at from Fig. 3.5, but is barely visible because of the extra variability induced by the cyclic solar forcing of experiment MR37. It is also an indication that the drier regime in the lowest troposphere is strongly dominated by convective activity.

Fig. 3.14 (top) is a plot of the time series for the surface evaporation. The most relevant features of this figure are: (i) the evaporation varies in the range of 0.95 to 1.45 mm/day during the warm regime, and increases with a very small variability from 0.93 to 1.12 mm/day during

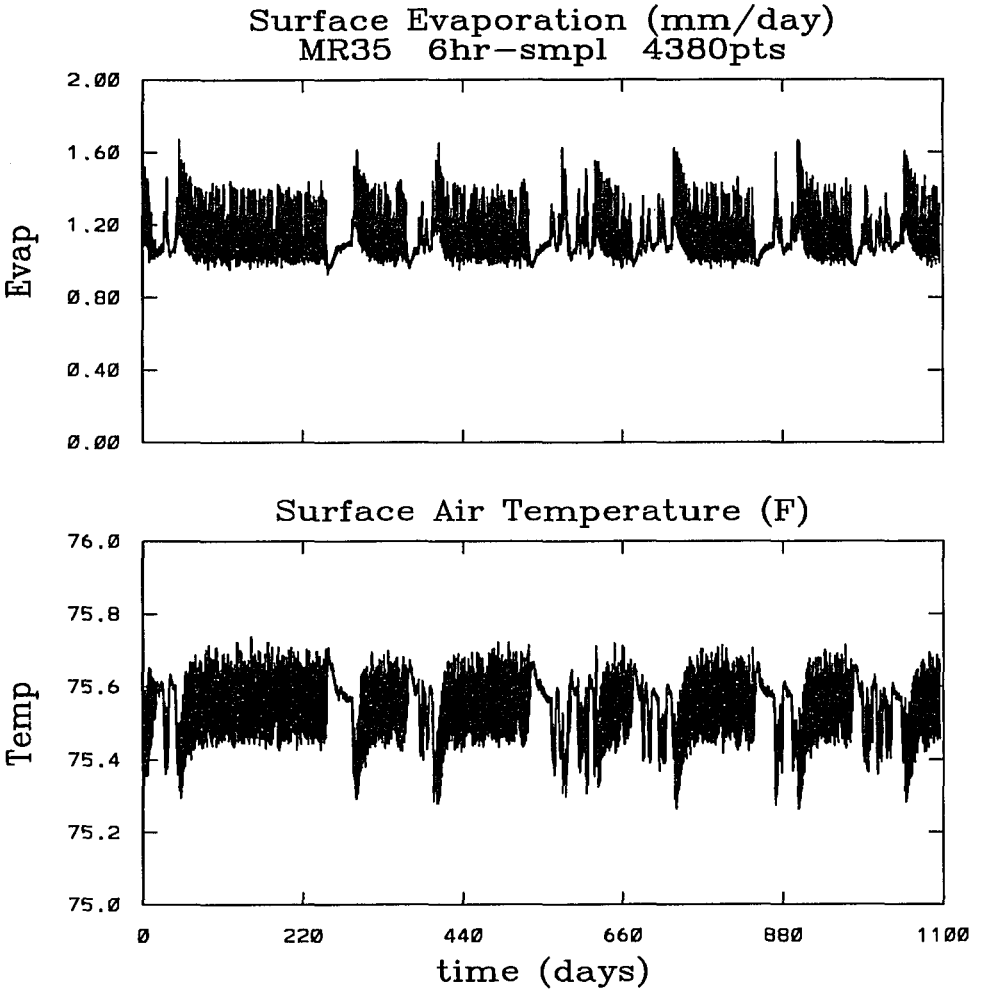

Figure 3.14 – Surface air temperature and evaporation for MR35.

the cooler regime; (ii) during the recovery transition occurs the largest variation of short time scale in the evaporation within the range of 1.1 to 1.7 mm/day. Both aspects of the surface evaporation time series are also characteristic of the experiment MR37, but are hidden in the diurnally induced variability.

Hence, the time series of the surface diagnostic variables for both experiments with and without the diurnal and seasonal forcing do present similarities. The simulated cyclic solar forcing exerts modulating effects, but do not change the fundamental nature of the interactions within the simulated atmospheric column. The results from experiment MR35 indicate the importance

of the sustained convective processes in the gradual depletion of the water vapor from the entirely active atmospheric column. Another fact that is highlighted in the simpler experiment MR35 is the radiative response of the simulated upper troposphere to the presence of water vapor aloft. It would be interesting to enhance the water vapor profile of the column under similar thermal boundary conditions, and examine this radiative response.

3.3.0 The numerical experiment MR38

The surface evaporation depends on three factors: the surface boundary winds, the difference between the air specific humidity and its saturation value at the surface, and the surface air temperature. For these numerical experiments the prescription of a higher surface boundary temperature implies a higher saturation specific humidity. This is a non-linear control on the evaporation. With the current parameterization, the wind dependence of the surface evaporation is also non-linear, but rather monotonically increasing. The numerical experiments MR36 and MR38 were designed to investigate the response of the simulated troposphere to an enhanced mean surface evaporation, in terms of the interactions between the cumulus convection and the radiative forcing. The means to attain a higher surface evaporation without a direct prescription of the same, is to prescribe higher surface winds. Several experiments were performed with higher upper air wind components with speed values in the range of 2.5 and 15 m/s, but in this work only the experiments with wind speed values of 3.5 and 12 m/s are reported, as they serve to present clearly the most noticeable differences.

The following conditions describe the numerical experiment MR38. The temperature at the surface boundary is kept constant at 30°C, for a simulated atmosphere over an oceanic grid point at the geographical location of (180°W, 2°N). The upper air horizontal wind components are kept at a constant and uniform 12 m/s throughout the troposphere. This is the high wind case, or high surface evaporation case. The experiment includes a simulation of the diurnal and seasonal cyclic insolation at the top of the atmosphere. The initial temperature and moisture profiles are similar to the ones used in the low evaporation experiments.

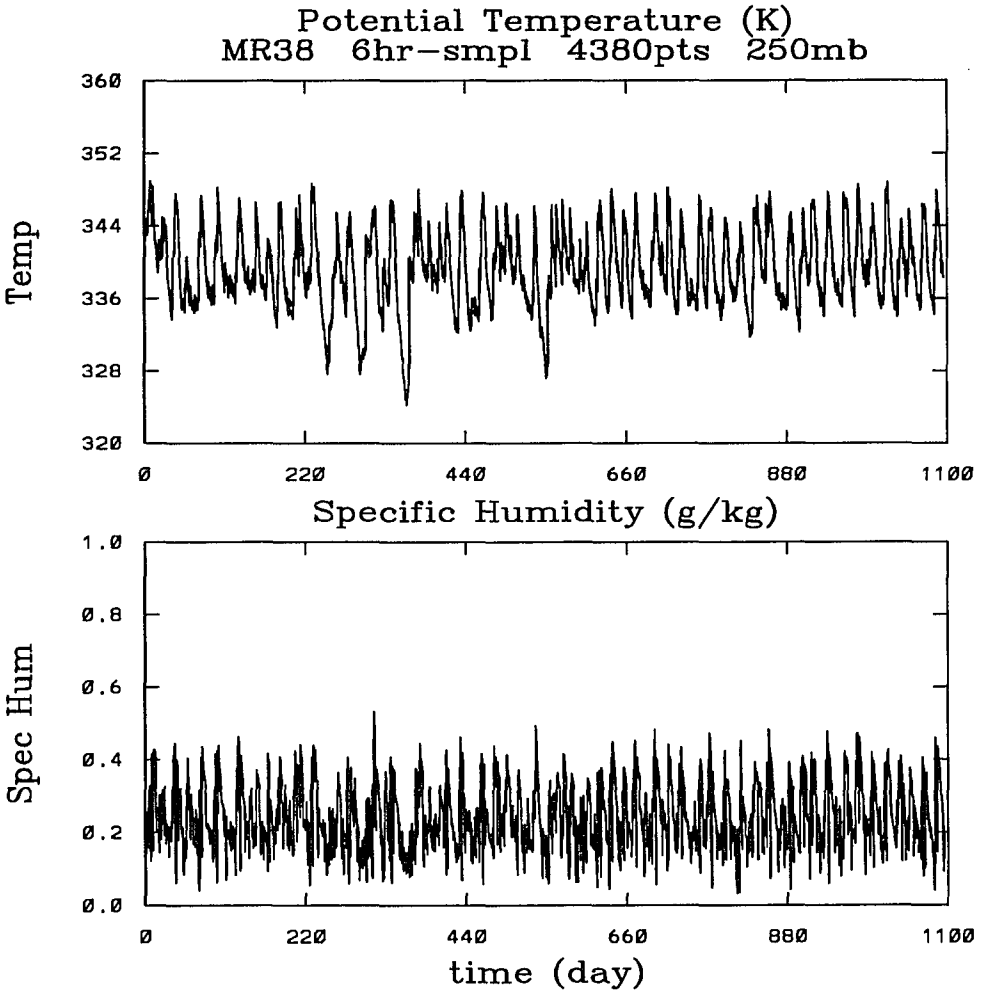

Figure 3.15 – θ and q at 250 mb for MR38. Time series for the experiment with high surface evaporation and cyclic solar forcing, at the upper troposphere.

3.3.1 The upper troposphere

Fig. 3.15 (top) illustrates the time series for the potential temperature, θ_{250}, at 250 mb. The relevant features of this figure are: (i) a non-drifting climate mean of 340 K during the full record; (ii) the simulated troposphere fluctuates some 14 K, between a regime at a low temperature of about 334 K and a regime at a high temperature of about 347 K; (iii) the transitions between regimes occur at time scales in the range of 20 to 60 day throughout the whole 1100 days of the simulation; (iv) there is a weak seasonal modulation of the 20 to 60 day phenomena; (v) the

cooler regime has a slightly longer residence time than the warmer regime; (vi) the transitions to the warmer regime are quicker than the transitions to the cooler regime; (vii) there are some strong cooling events with a peak-to-peak amplitude of about 23 K, but lesser in number than for the experiments MR35 or MR37.

Fig. 3.15 (bottom) illustrates the time series of the specific humidity, q_{250}, at 250 mb. The relevant features of this figure are: (i) the simulated upper troposphere fluctuates between a dry regime of about 0.08 g/kg and a moist regime of about 0.42 g/kg; (ii) the fluctuations occur in the time scales of 20 to 40 days; (iii) the dry regime has a slightly longer residence time; (iv) most of the drying events occur in phase with the cooling events identified for θ_{250}; (v) there is a weak seasonal modulation; (vi) most of the time the warm regime is in phase with the moist regime; (vii) the dry to moist transition is quicker than the transition into the dry regime.

Hence, during the numerical experiment MR38, for a prescribed high sea surface temperature of 30°C, high uniform upper air winds of 12 m/s, and in the presence of the seasonal and diurnal modulations of the insolation at the top of the troposphere, the simulated atmosphere oscillates between a dry and cold regime and a warm and moist regime, as it occurs in the low surface evaporation cases. As opposed to the simulations MR37 and MR35, however, the case of the high upper air winds has the longest residence time in the cooler regime, and the dominant phenomena are in the 20 to 60 day time scales. The upper troposphere is warmer than for the low wind case: for the experiment MR37 the range of temperature variability is 330 K to 341 K, while for the experiment MR38 it is 328 to 348 K. The amount of water vapor is also higher: 0.05 to 0.35 g/kg for MR37, while it is 0.05 to 0.5 g/kg for MR38. For both low and high uniform upper air wind cases there are some strong transitions, although lesser in number for the high wind cases.

Fig. 3.16 (top) illustrates the time series for the long wave radiative cooling rate at 250 mb, δT_{250}^{LWR}. The most relevant features of this figure are: (i) there are frequent transitions between a faster cooling regime of about -0.20 K/day, and a mildly cooling regime of about -0.05 K/day; (ii) the dominant phenomena is in the 20 to 60 day time scales; (iii) the strong cooling

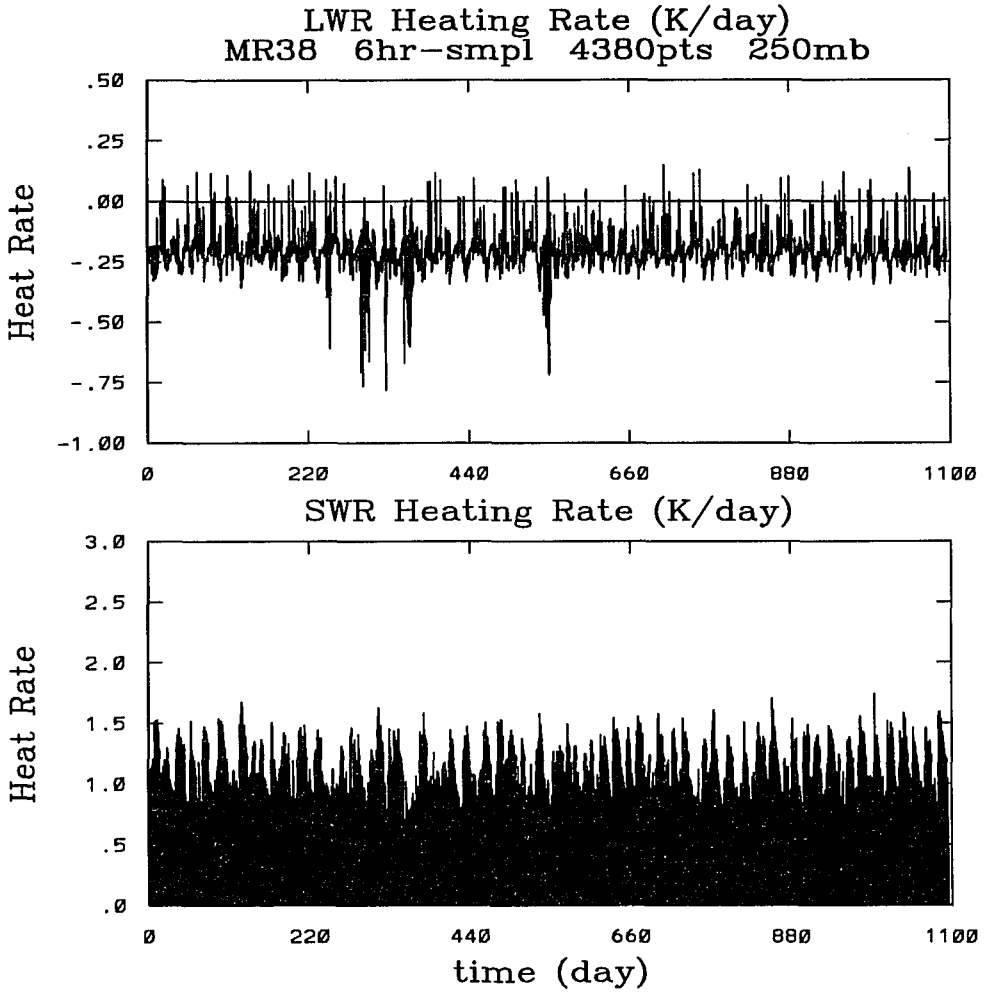

Figure 3.16 – δT_{LWR} and δT_{SWR} at 250 mb for MR38.

events are characterized by LWR rates of up to -0.30 K/day; (iv) there are sparse events of upper tropospheric warming by LWR, up to 0.05 K/day, coincident with the coolest portions of the 20 to 60 day phenomena of θ_{250}.

Fig. 3.16 (bottom) is a plot of the time series for the short wave radiative heating rate, δT_{250}^{SWR}, at 250 mb. The relevant features of this figure are: (i) the upper troposphere warms up at a rate of up to 1.5 K/day; (ii) the 20 to 60 day phenomena modulates the daily maxima of the SWR rate in phase with the moisture variability at those time scales; (iii) the peak values for δT_{250}^{SWR} coincide with the warm and moist regime; (iv) the strong cooling events are in phase

with the low daily maxima of the SWR rate.

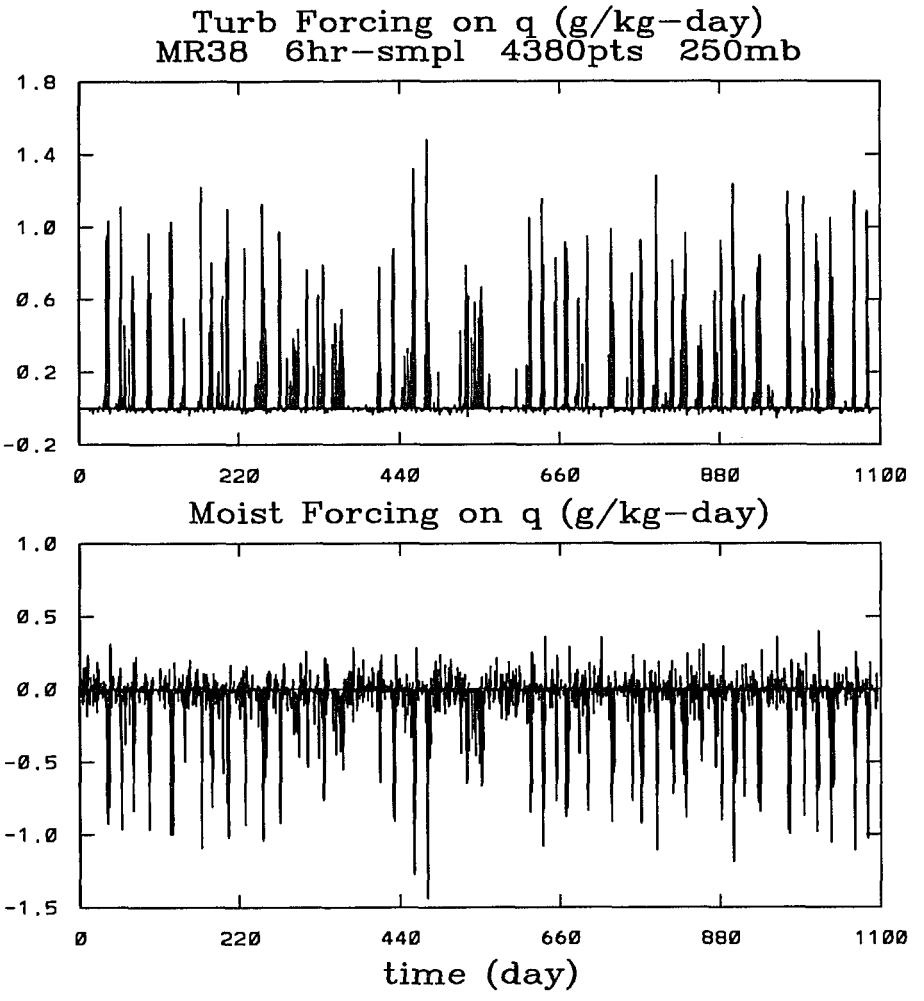

Figure 3.17 – δQ_{trb} and δQ_{mst} at 250 mb for MR38.

Fig. 3.17 (top) is a plot of the time series for the turbulent forcing term on the specific humidity, δQ^{trb}_{250}, at 250 mb. The relevant features of this figure are: (i) most of the time there is deposition of moisture at the upper troposphere in the range of 0 to 1.4 g/kg/day; (ii) moisture is depleted during a significant number of days up to -0.05 g/kg/day; (iii) there are sharp increases in the turbulent transport of moisture in time scales of 20 to 60 days; (iv) the recovery phase of the strong cooling events is characterized by sustained deposition of water vapor by turbulent transport.

Fig. 3.17 (bottom) is a plot of the time series for the moist processes forcing on the specific humidity at 250 mb, δQ_{250}^{mst}. The relevant features of this figure are: (i) most of the time the moist processes deplete water vapor from the upper troposphere up to -1.3 g/kg/day; (ii) there are a significant number of days with positive forcing by the moist processes, of up to 0.3 g/kg/day; (iii) the 20 to 60 day phenomena deplete water vapor in short duration events; (iv) there is deposition of moisture at the upper troposphere by the moist processes for a significant fraction of the warmer's regime residence time.

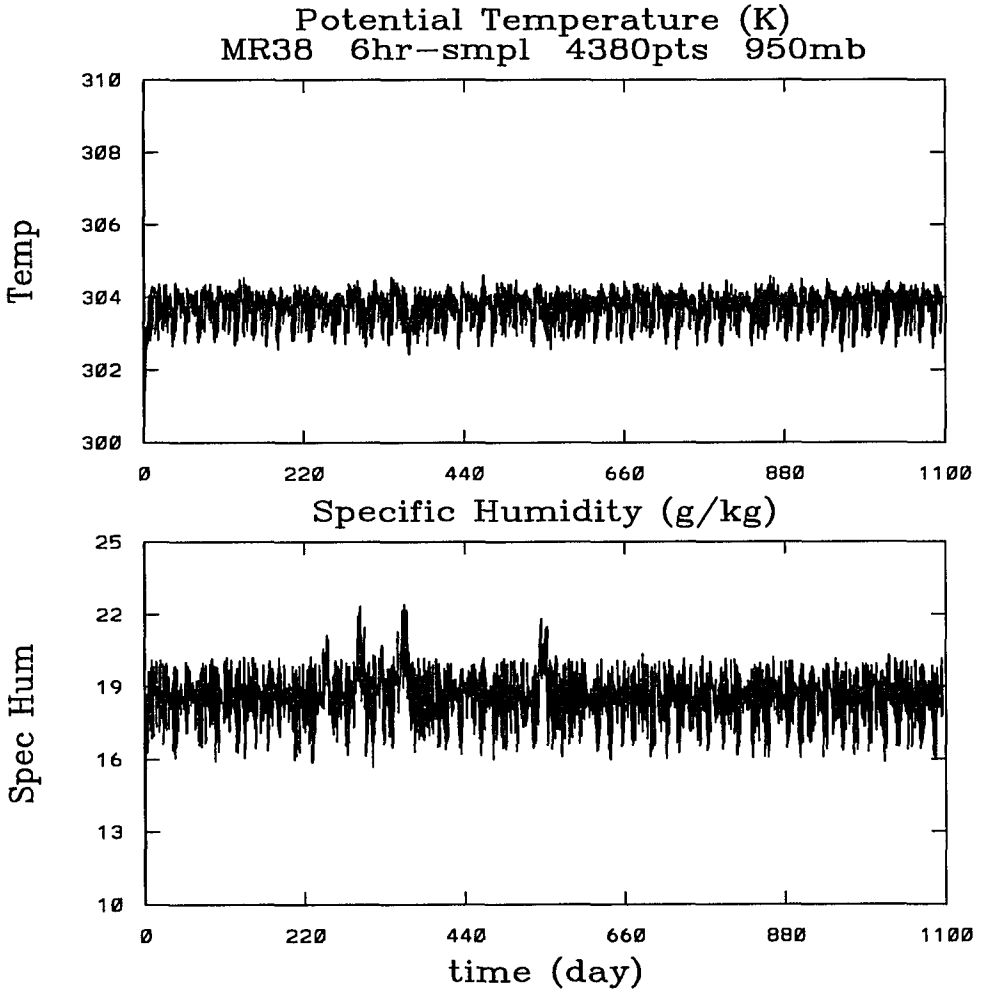

Figure 3.18 – θ and q at 950 mb for MR38. Time series for the experiment with high surface evaporation and cyclic solar forcing, at the surface layer.

3.3.2 The lower troposphere

Fig. 3.18 (top) is a plot of the time series for the potential temperature at 950 mb, θ_{950}. The relevant features of this figure are: (i) the temperature variability seems dominated by the 20 to 60 day time scales in the range of 302.5 to 304.5 K; (ii) the warm regime has the longest residence time at about $304 \pm 0.2K$; (iii) the upper air strong cooling events are also surface cooling events.

Fig. 3.18 (bottom) is a plot of the time series for the specific humidity at 950 mb, q_{950}. The relevant features for this figure are: (i) q_{950} varies mostly in the range of 16 to 21 g/kg, without long term trends; (ii) the upper air strong cooling events of 14 K are characterized by a moist surface layer with q_{950} varying in the range of 19 to 22 g/kg; (iii) there seems to be a strong modulation of the daily variability in the 20 to 60 day range.

Fig. 3.19 (bottom) illustrates the time series for the surface evaporation, E_v. The relevant features of this figure are: (i) the evaporation varies in the range of 0.7 to 2.7 mm/day; (ii) the dominant time scale of the variability is in the 20 to 60 day; (iii) the 20 to 60 day fluctuation in the evaporation is in phase with the temperature variation at the upper troposphere, and with sharp increases during the recovery phase towards a warmer regime; (iv) the most common value is in the range of 1 ± 0.2 mm/day.

Fig. 3.20 contain plots for the time series of the stratiform (top) and convective (bottom) precipitation types. The relevant features of these figures are: (i) the stratiform precipitation occur sparsely in time, within the range of 0 to 0.5 mm/day; (ii) the strongest events of stratiform precipitation are in phase with the strong upper tropospheric cooling episodes; (iii) the convective precipitation occur most of the time within the range of 0 to 4 mm/day; (iv) the 20 to 60 day phenomena are characterized by sustained convective precipitation rates of about 0.5 to 1.5 mm/day.

3.4.0 The numerical experiment MR36

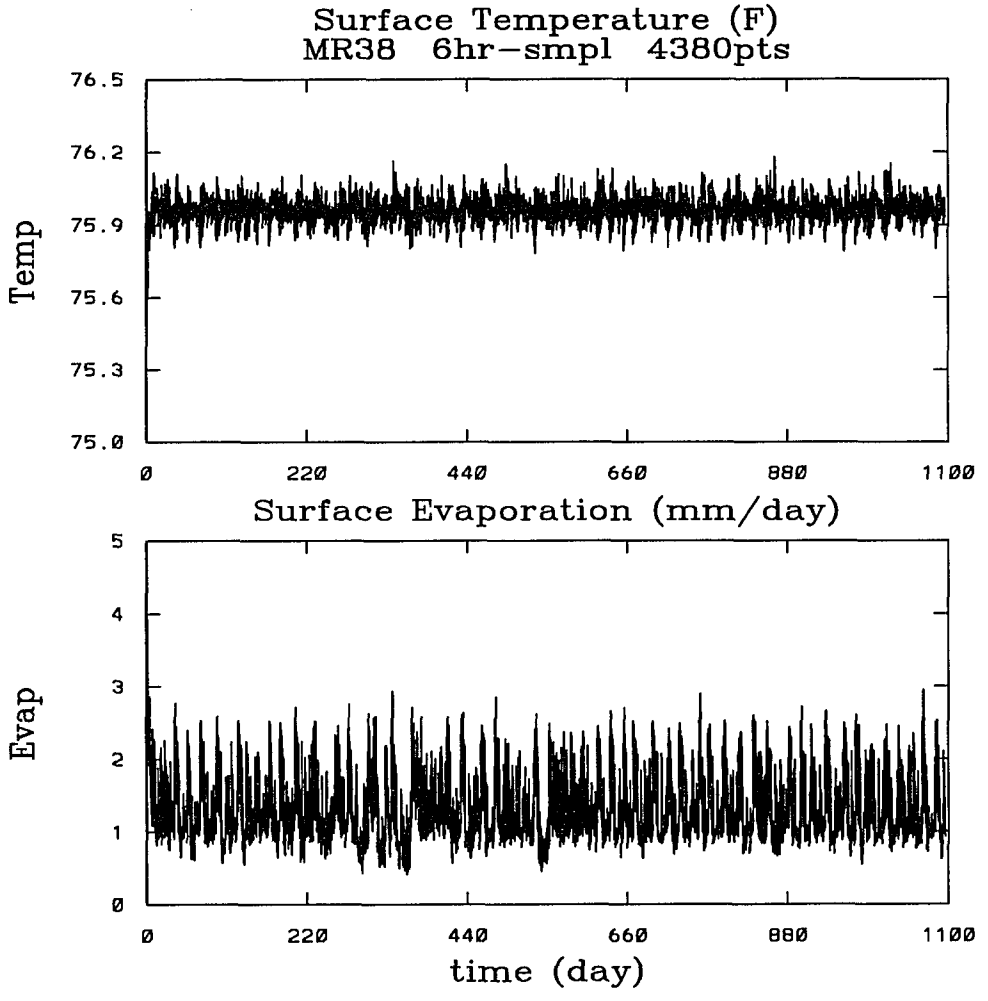

Figure 3.19 – Surface air temperature and evaporation for MR38.

The following conditions describe the numerical experiment MR36. The temperature at the surface boundary is kept constant at 30°C, also, for a simulated atmosphere-oceanic environment. As for the previously described experiment, the upper air winds are prescribed at a constant and uniform 12 m/s throughout the troposphere. There is no inclusion of the diurnal and seasonal solar forcings at the top of the simulated troposphere. The initial temperature and specific humidity profiles were the same as the ones used in experiment MR38. It has been mentioned that the removal of the cyclic solar forcing in the low surface evaporation experiment helped clarify the existence of non-solar forced variabilites for the isolated atmospheric column. It is

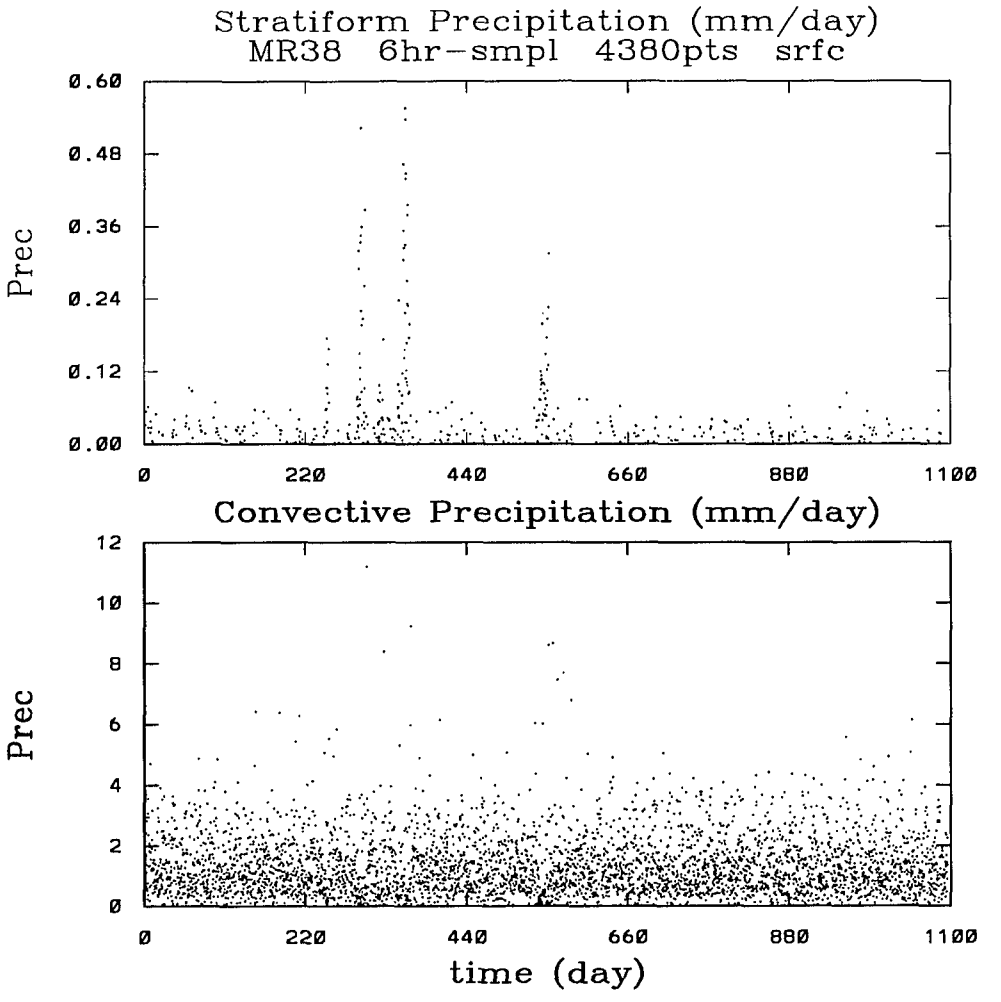

Figure 3.20 – Stratiform and convective precipitation for MR38.

expected that for a higher surface evaporation case, some variabilities, not induced by the cyclic solar forcing, will remain active in the atmospheric column as well.

3.4.1 The upper troposphere

Fig. 3.21 (top) illustrates the potential temperature at 250 mb, θ_{250}, during the full simulation. Some features of this graph are: (i) a non-drifting climate mean of about 340 K; (ii) fluctuations between the 336 and 348 K levels, with time scales of about 30 days; (iii) the coldest temperature levels have a longer residence time than more warmer levels.

Fig. 3.21 (bottom) is a plot of the specific humidity at 250 mb. Similar to the equivalent plot

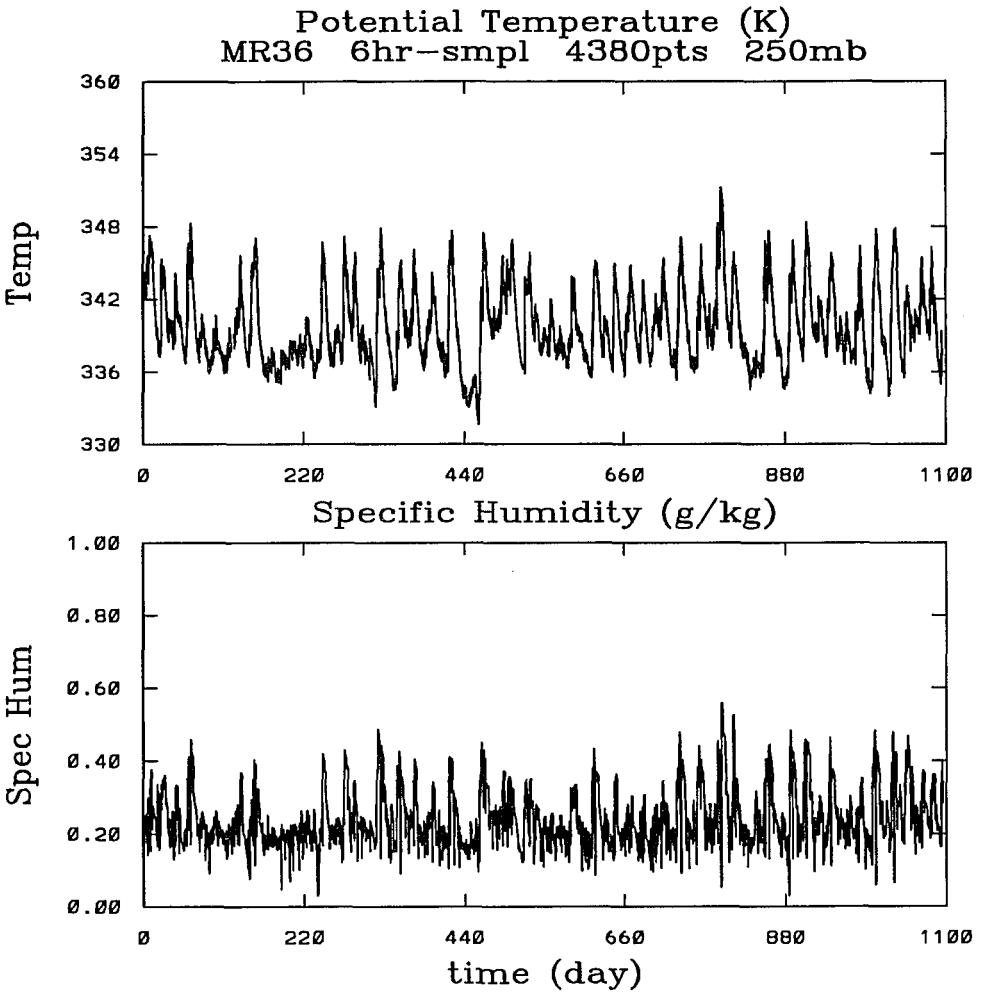

Figure 3.21 – θ and q at 250 mb for MR36. Time series at the upper troposphere for the experiment with high surface evaporation, and without cyclic solar forcing.

in experiment MR38, some relevant features of this figure are: (i) the non-drifting mean level of about 0.22 g/kg; (ii) the drier levels have a longer residence time; (iii) fluctuations of about 0.2 to 0.3 g/kg, with time scales of about 30 days.

Fig. 3.22 illustrate the radiative heating rates at the upper troposphere in MR36. Some noticeable features of these graphs are: (i) the most typical level for the LWR heating rate (top) is about -0.20, with a variability in the range of -0.28 to 0.09 K/day, similar to the mean level in MR38; (ii) the mean level for the SWR (bottom) is about 0.7 K/day; (iii) the SWR heating

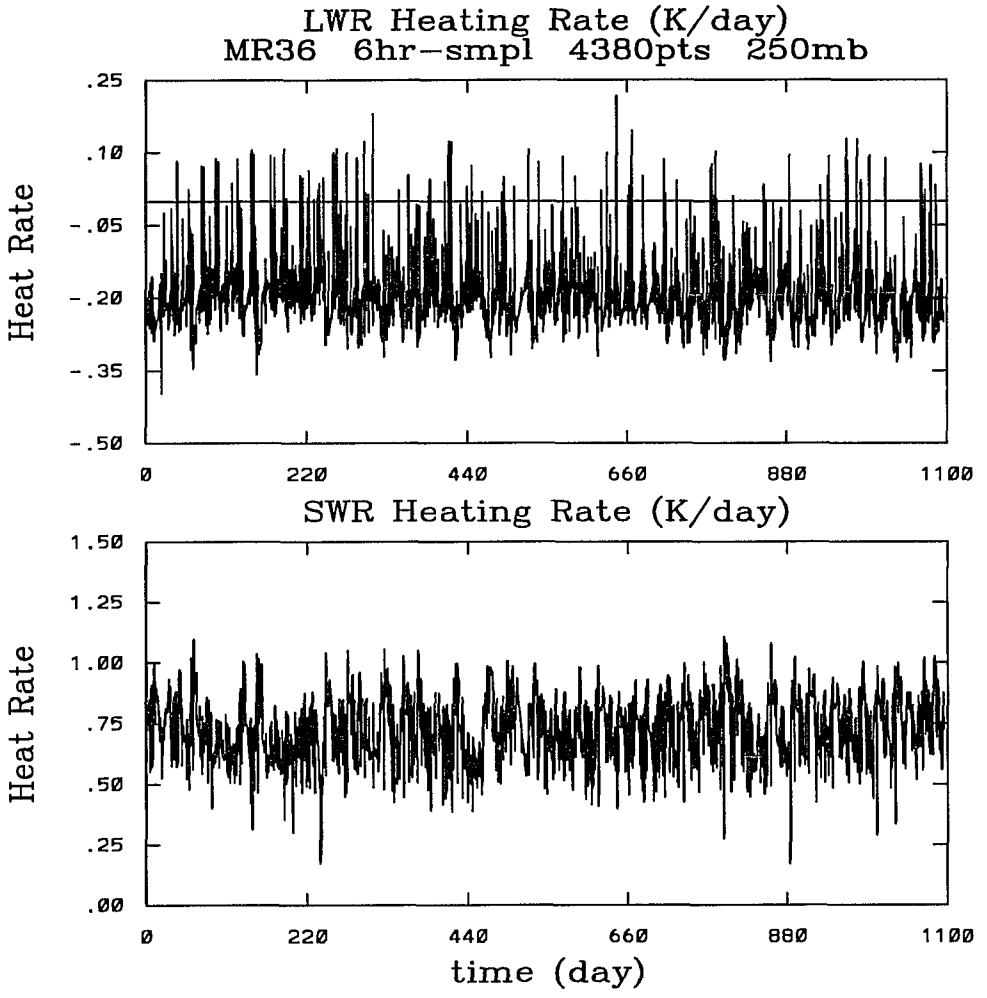

Figure 3.22 – δT_{LWR} and δT_{SWR} at 250 mb for MR36.

rate also seems related to the presence of water vapor in the upper troposphere.

Fig. 3.23 illustrates the time series for the turbulent (top) and moisture (bottom) processes forcings on the specific humidity at 250 mb. Some features of these graphs are: (i) except during the rare strong cooling episodes, turbulent forcing of the humidity at higher layers is mostly nonexistent; (ii) the few occasions for which $\delta q_{trb} \neq 0$, reach levels of about 0.8 g/kg/day; (iii) moisture processes forcing fluctuates within 0.15 g/kg/day about zero most of the time, but strong depletion of water vapor at 250 mb occurs coincident with the strong pumping of vapor by turbulence. In essence, the upper troposphere is convectively active most of the time in these

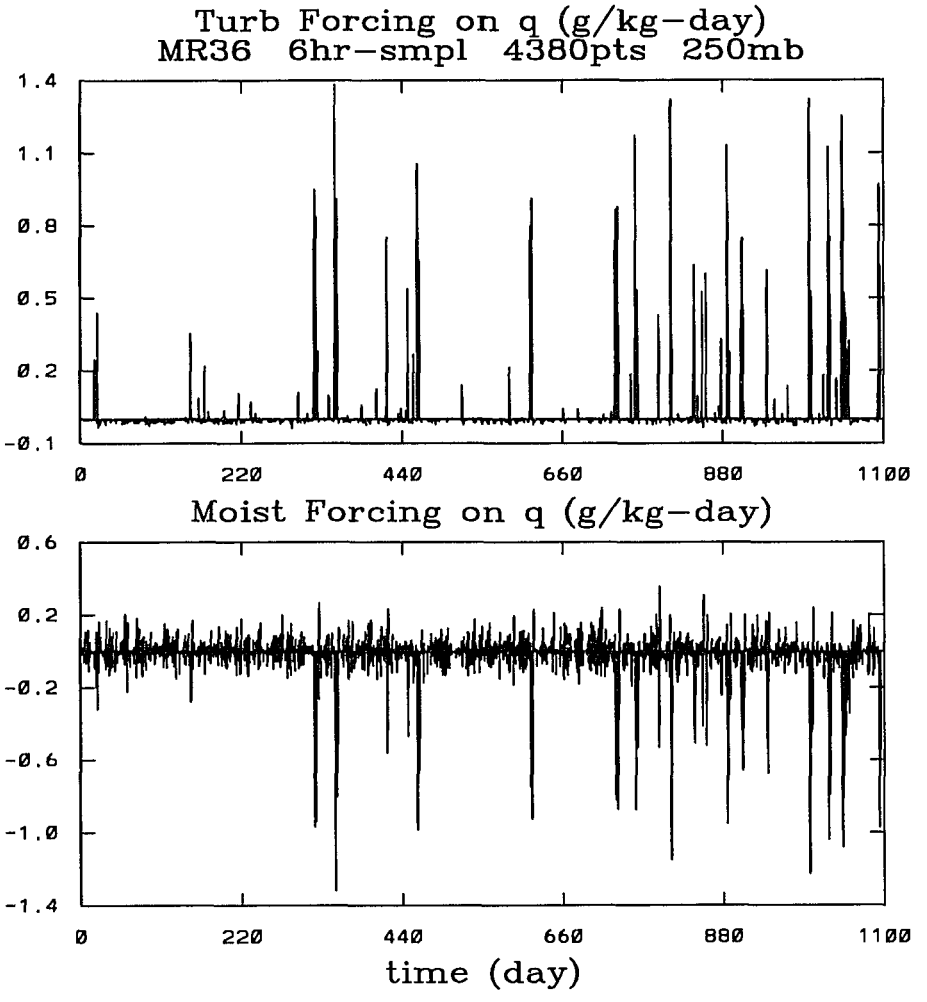

Figure 3.23 – δq_{trb} and δq_{mst} at 250 mb for MR36.

high surface evaporation cases.

3.4.2 The lower troposphere

Fig. 3.24 illustrate the time series for the potential temperature (top) and the specific humidity (bottom) at the layer near the surface for the experiment with high evaporation and without cyclic solar forcing. Some features of these plots are: (i) the mean temperature is about 303.6 K and the mean specific humidity about 18.5 g/kg; (ii) the most likely level for θ is about 303.8 K, while for q is about 18.5 g/kg; (iii) while aloft (as seen for θ_{250} and q_{250}) the most likely regime is characterized by colder temperatures and dryer air, near the surface the most likely

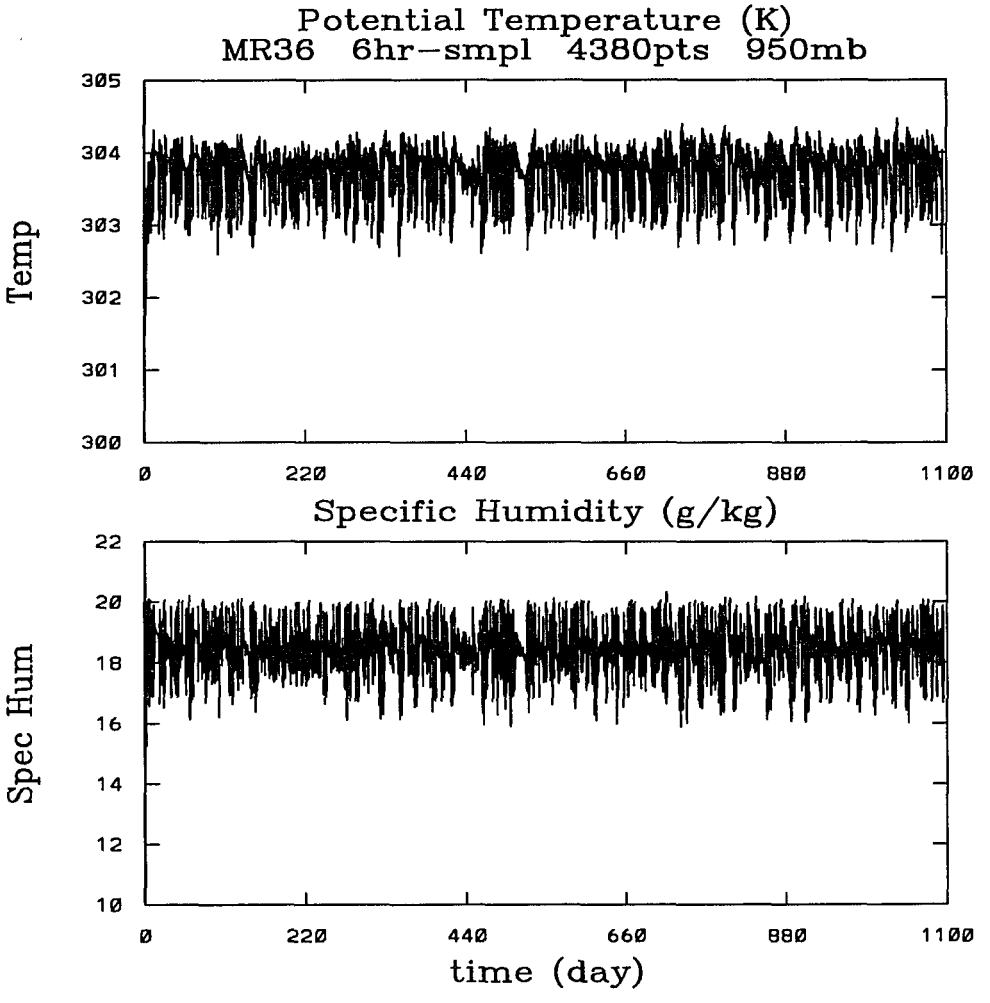

Figure 3.24 – θ and q at 950 mb for MR36. Time series near the surface layer for the experiment with high surface evaporation and no cyclic solar forcing.

regime is characterized by warmer temperatures; (iv) the stronger cooling episodes of the upper troposphere occur simultaneously with lower tropospheric cooling.

Fig. 3.25 (top) is a graph of the time series for the surface evaporation during the numerical experiment MR36. The most relevant features of this figure are: (i) the most likely value for the evaporation is about 1.2 mm/day; (ii) upper air transitions between regimes are coincidental with enhanced evaporation; (iii) during the strong cooling events aloft the evaporation increases nearly monotonically in the range of 0.8 to 1.4 mm/day.

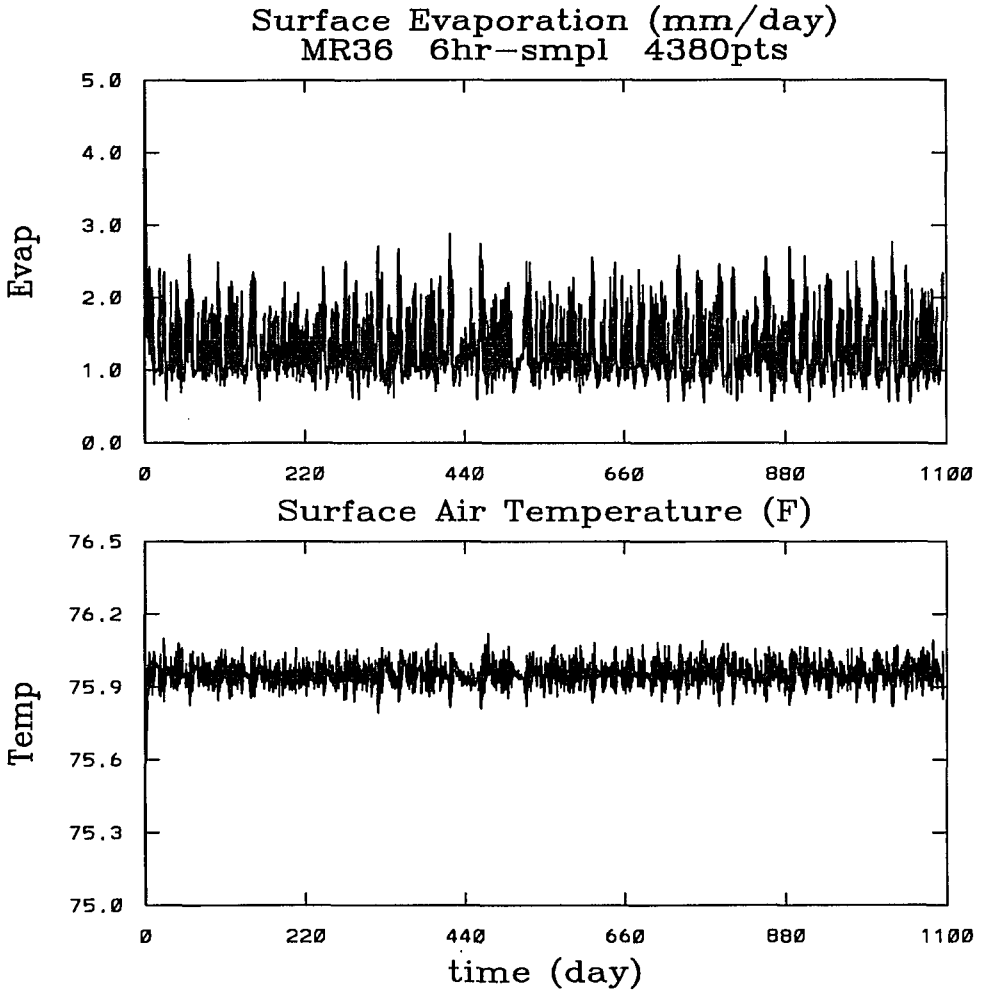

Figure 3.25 – Surface air temperature and evaporation for MR36.

As seen from Fig. 3.26 most of the time for this experiment, there is only convective precipitation, that fluctuates in the range of 0.5 to 2.0 mm/day. The strong cooling episodes were characterized by a reduced range in the precipitation of about 1 ± 0.2 mm/day.

3.5.0 The Time Evolution of the Vertical Structure

It has been shown that the simulated troposphere with a higher surface evaporation fluctuated also between two regimes. The cold and dry regime of the high evaporation case, with its enhanced convective activity and a sparse stratiform precipitation, is similar to the cold and dry regime of the low evaporation cases. Close similarities are also recognized for the warm and moist

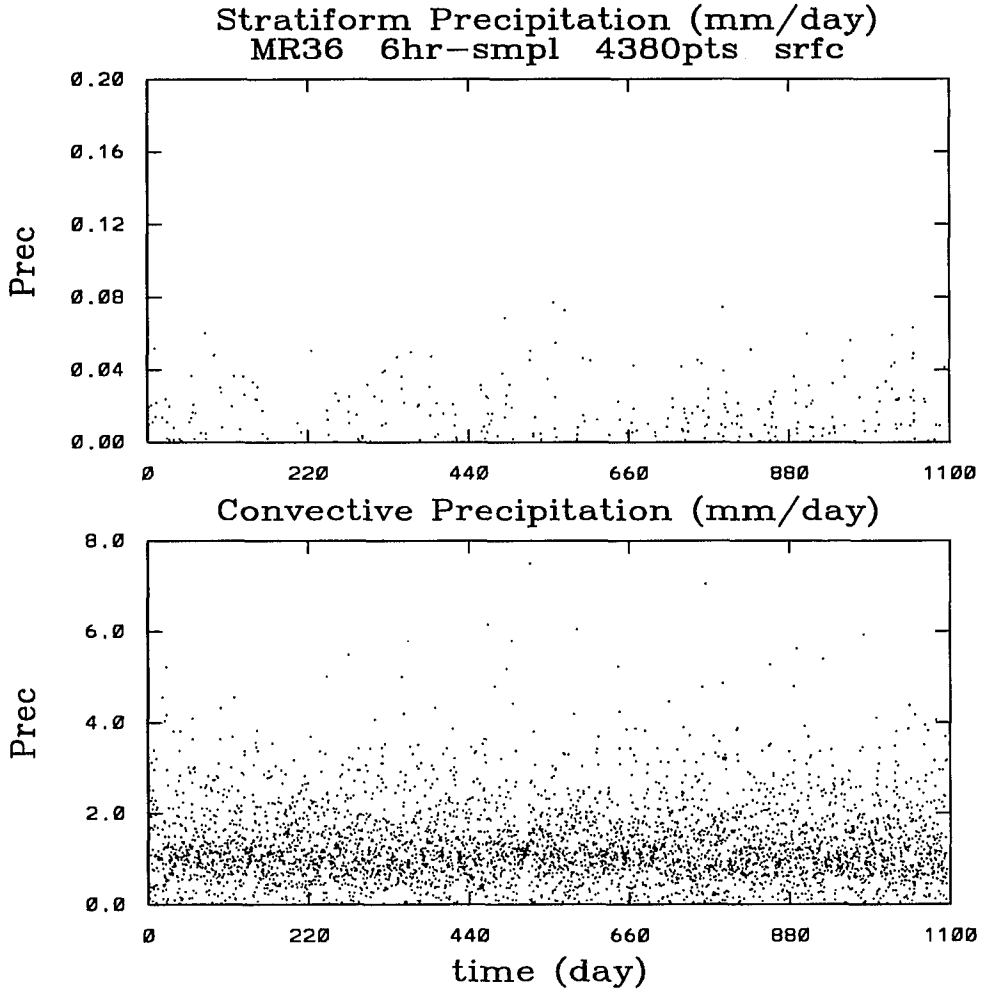

Figure 3.26 – Stratiform and convective precipitation for MR36. The values of the precipitation are averaged at 6 hours intervals.

regimes for the low and high surface evaporation cases. It seems that in this simplified model, with essentially two prognostic variables, the variability in the climate is dominated by transitions between two regimes with coincidental higher and lower values for both variables. Each regime is composed of a large number of states, but under yet unspecified conditions a transition might occur between these regimes. The time scales dominant for these transitions seem to be dependent upon the availability of moisture throughout the simulated troposphere, and not on the diurnal and seasonal solar forcing. This is not like saying that short and long time scales

are not interacting to favor transitions between the most likely regimes. The vertical structure must then be compared to ascertain the similarities that in a more or less moist atmosphere will induce the transitions in this model.

This section is a description of the vertical structure typical of each regime. The procedure is to describe the most likely (i.e., the modal) profiles of the prognostic variables for each regime; and in particular, comparing these with the typical profiles of the physical forcing terms.

3.5.1 The Most Likely State for low E_v

Fig. 3.27 is a combined plot of the modal potential temperature for the cold and warm regimes in experiments MR35 (top) and MR37 (bottom). Any one single curve in the set from Fig. 3.27 through Fig. 3.34 is constructed as follows. A time range within one regime is subjectively selected from the original time series. At each layer, and sampling at 1 hour intervals, the values of the temperature were stratified in 10 equally spaced bins, between the corresponding minimum and maximum values. The mid-range value of the bin with the highest number of counts is the value presented at each layer as the modal value. The idea is to represent the "most likely state" of the temperature profile, while avoiding the problem of the excursion of the mean value from the range of values most likely to occur. Given the fact that the warm regime in the potential temperature time series for the low wind experiments is characterized by a narrow range of values, the plot represents the "typical state" of such regime. As a comparison, a similar curve is built for the colder regime, and drawn on the same set of axes.

Fig. 3.27 illustrate some of the striking similarities between the results for the experiments with (bottom) and without (top) seasonal and diurnal cycles, for the low surface evaporation cases. The temperature profile for the warmer regime is quite similar in both experiments and, even the stability index, as related to the vertical gradient of the potential temperature, is also very similar. For both experiments, the temperature of the PBL in the cooler regime is higher than the corresponding one for the warmer regime. This is due to an enhanced latent heating

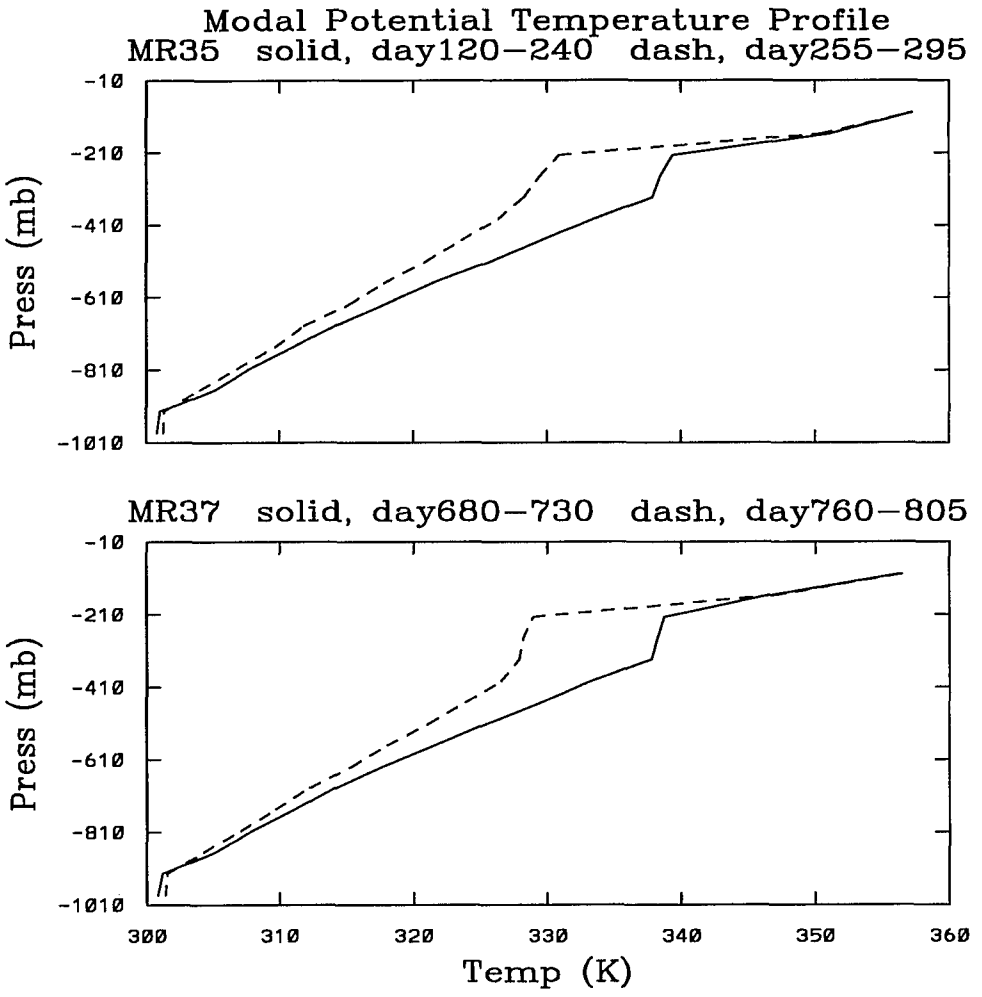

Figure 3.27 – Modal profile for θ during MR35 and MR37. The most likely value for the potential temperature, for the experiments with low surface evaporation: (upper panel) without, (lower panel) with cyclic solar forcing. For both templates: (solid) warmer, (dashed) cooler regimes.

in the lowest troposphere, as can be seen from Fig. 3.31. Above the 300 mb layer, both regimes exhibit a drastic change in the lapse rate. The experiment with the cyclic solar forcing includes a sharper change in the lapse rate at about 350 mb. This is due to a stronger gradient in the latent heating rate, and to a much reduced SWR heating (see Fig. 3.31 and Fig. 3.30).

Fig. 3.28 is a combined plot of the typical water vapor profiles during the warmer and

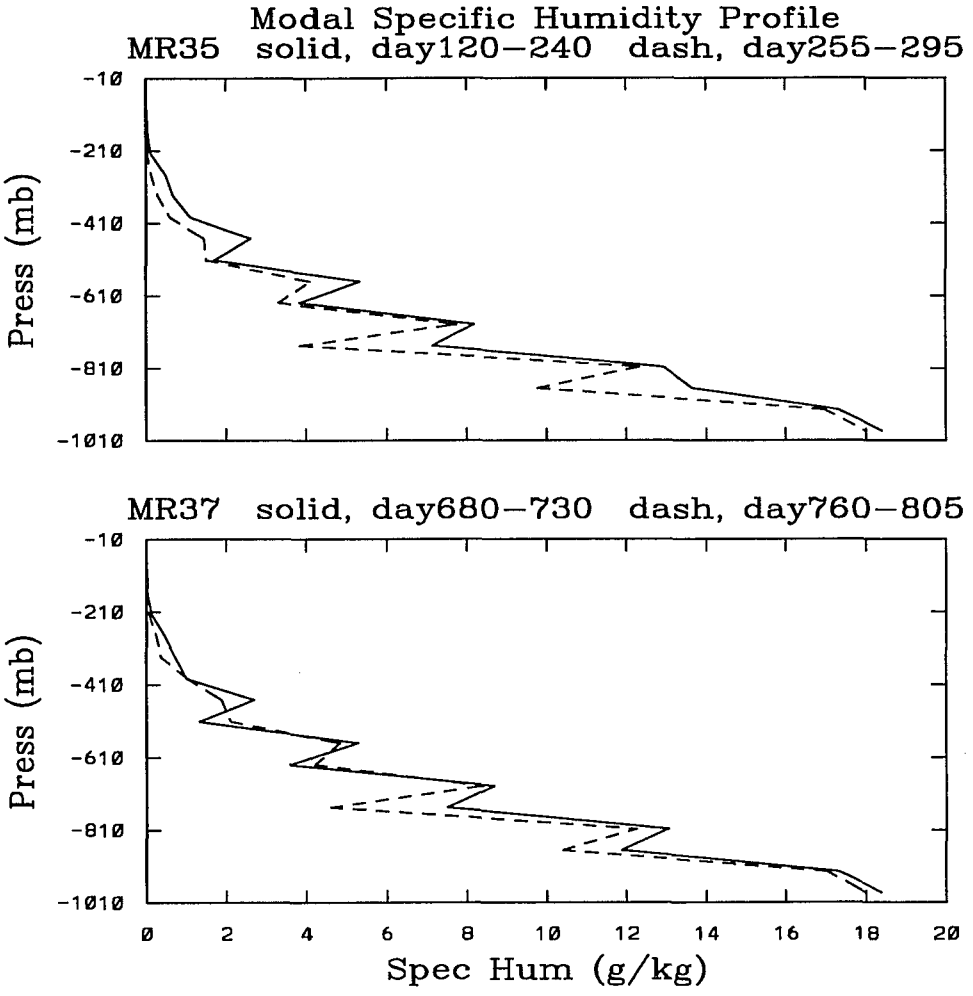

Figure 3.28 – Modal moisture profiles for MR35 and MR37. The arrangement of the curves is similar to that of the previous figure.

cooler regimes of the experiments MR35 (top) and MR37 (bottom). It is constructed similarly to Fig. 3.27. The moisture profiles for the warmer regimes are quite similar for both experiments. The specific humidity at the 800 mb layer of the experiment without cyclic solar forcing is slightly larger. The upper troposphere in the layer of 300 to 500 mb has a slightly larger specific humidity in the experiment with cyclic solar forcing, during the cooler regime. Convective transport of water vapor accounts for both differences (see Fig. 3.33).

It can be seen from Fig. 3.28 that the upper troposphere above 500 mb is certainly dryer

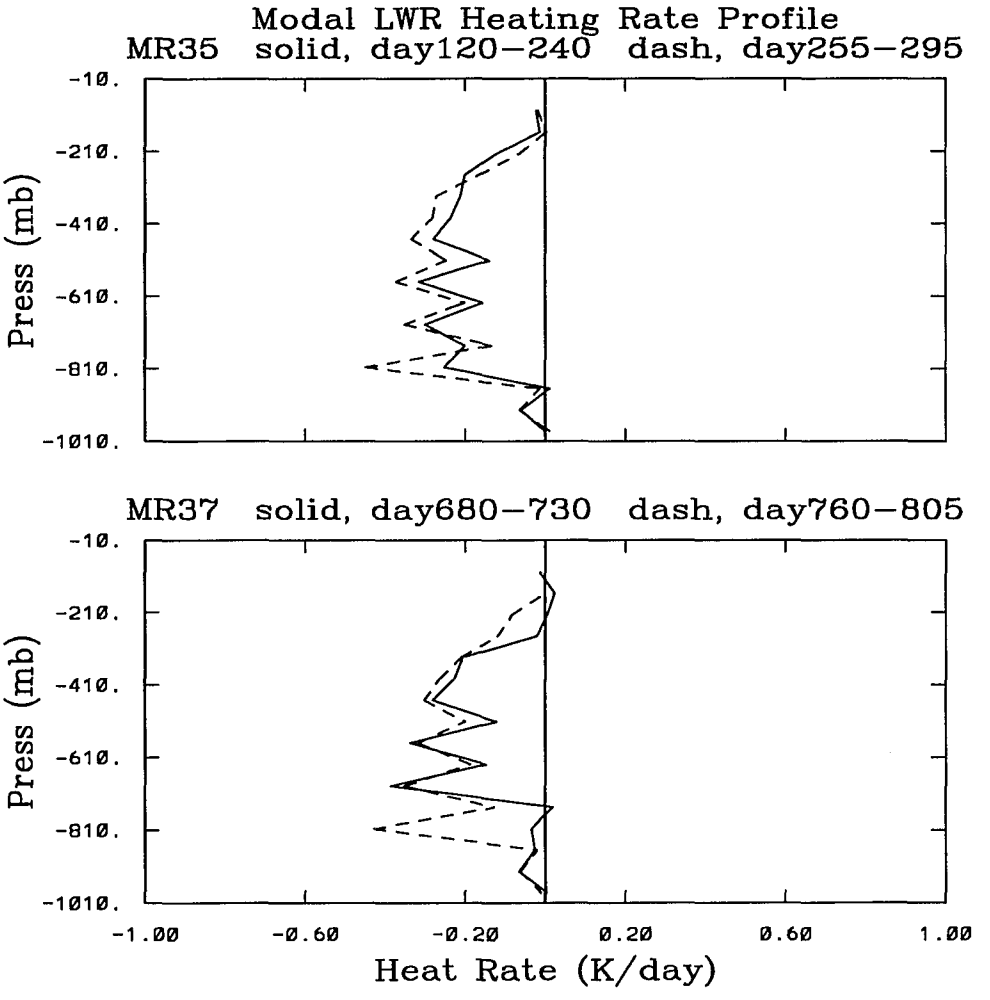

Figure 3.29 – LWR modal heating rates for MR35 and MR37.

in the cooler regime, but that the sharpest differences between regimes occur below the 600 mb layer. The typical values of specific humidity in the PBL are about 18 g/kg, but at 850 and 750 mb the differences between regimes are as large as 3–4 g/kg. Convective activity induces steeper gradients in the moisture profile (see Fig. 3.33) below the 650 mb level. Convection depletes water vapor from the lowest troposphere during a warm regime, but loads up the layers above 550 mb. During the cooler regime the convective activity becomes stronger in the lowest 150 mb, with larger fluctuations in the layer above the PBL. Indeed, this enhanced convective activity during the cooler regime releases latent heat in the lowest 600 mb, in net larger amounts than

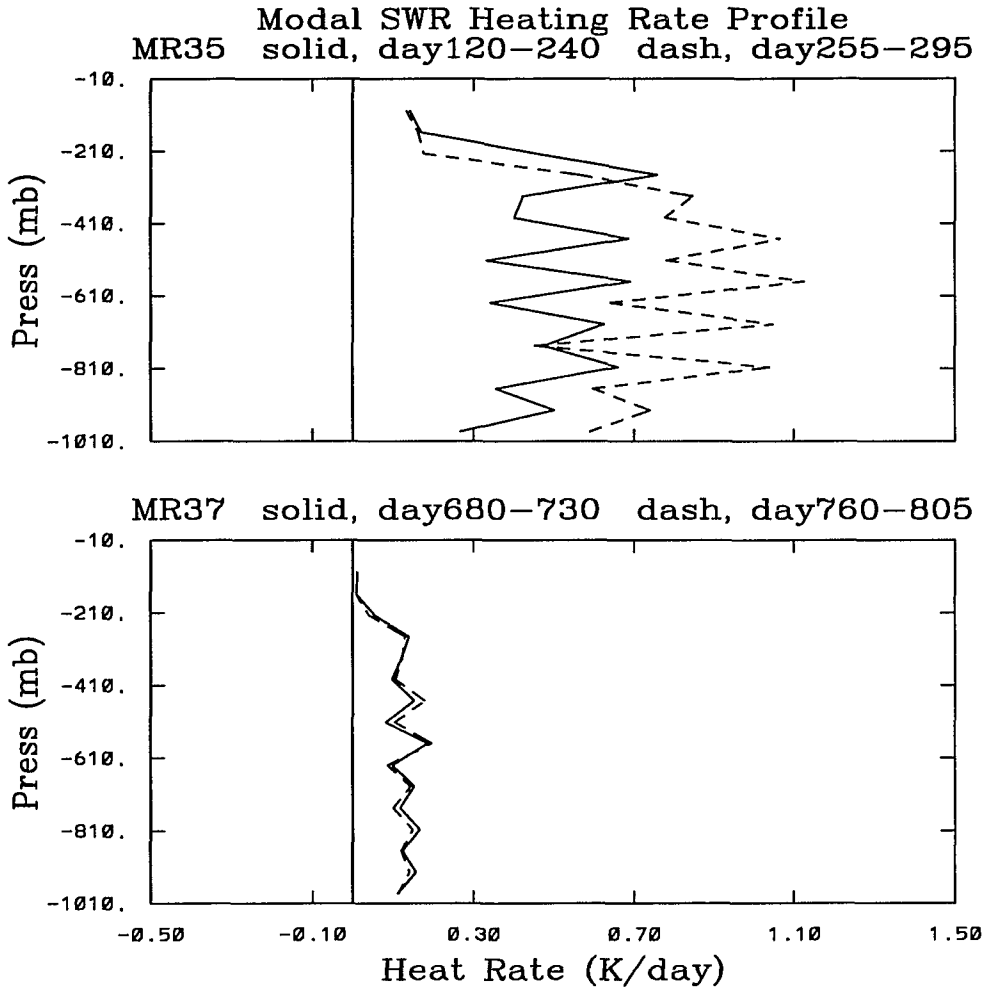

Figure 3.30 – SWR modal heating rates for MR35 and MR37.

during the warmer regime (see Fig. 3.31). The warmer regime is characterized by latent heat release in the lower 500 mb and by absorption of water vapor in the next 300 mb, while the cooler regime is characterized by an entire convectively active column. Hence, one of the main differences between the two regimes is the extent to which the simulated atmospheric column is convectively active. The other main difference concerns the radiative interactions with the atmospheric moisture.

In the presence of the cyclic solar forcing, there is radiative cooling in most of the cloud layer in both regimes. The LWR cooling rate diminishes with height above 300 mb. The cooler

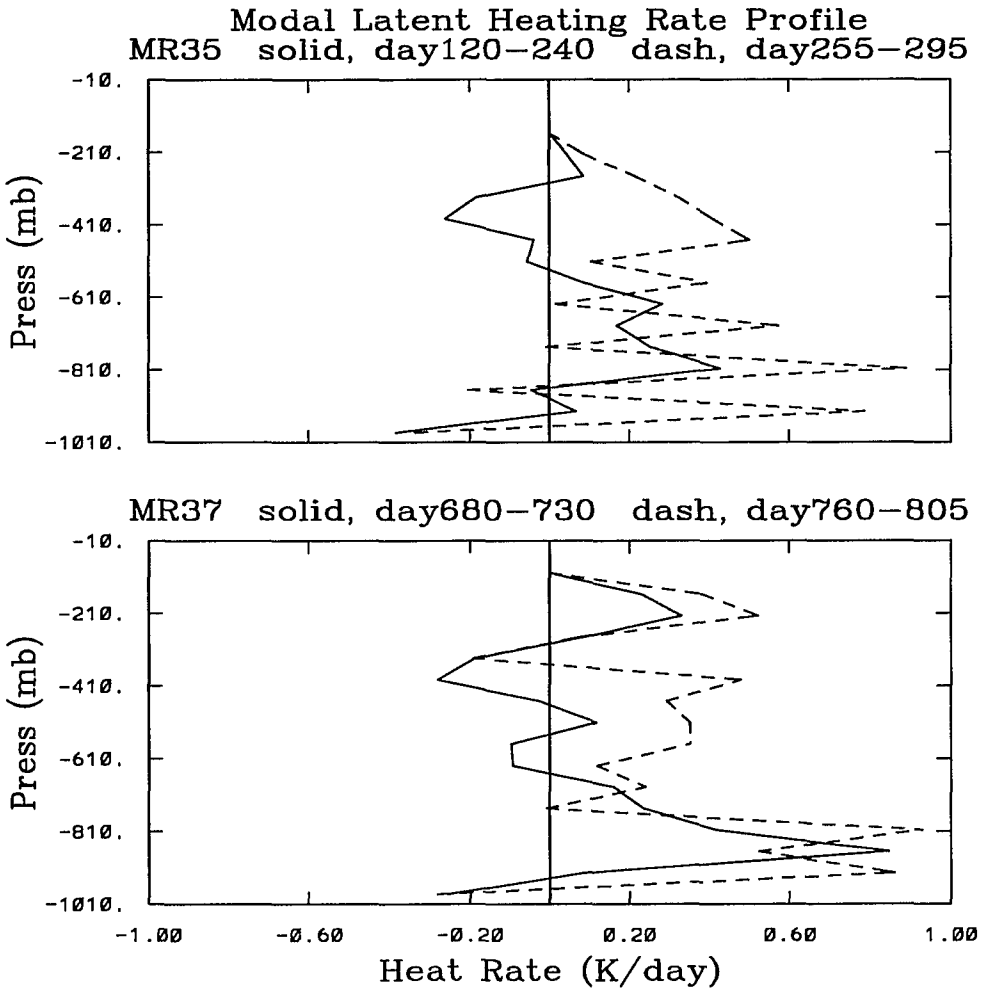

Figure 3.31 – Modal latent heating rates for MR35 and MR37.

regime also cools off radiatively throughout the full troposphere, but the LWR rate reduction with height is slower above the 300 mb.

In the absence of cyclic solar forcing, the drier regime's LWR rate is larger mostly everywhere, but above 300 mb the cooling rate is smaller than the corresponding rate of the moistier regime. The SWR heating rate is smaller for the cooler regime than for the warmer regime only above 300 mb. Hence, the top of the simulated troposphere cools off less and warms up less (see Fig. 3.29 and Fig. 3.30). The stronger convective activity during the cooler regime is sustained by an enhanced latent heat release at the lower troposphere, a reduced LWR cooling and a reduced

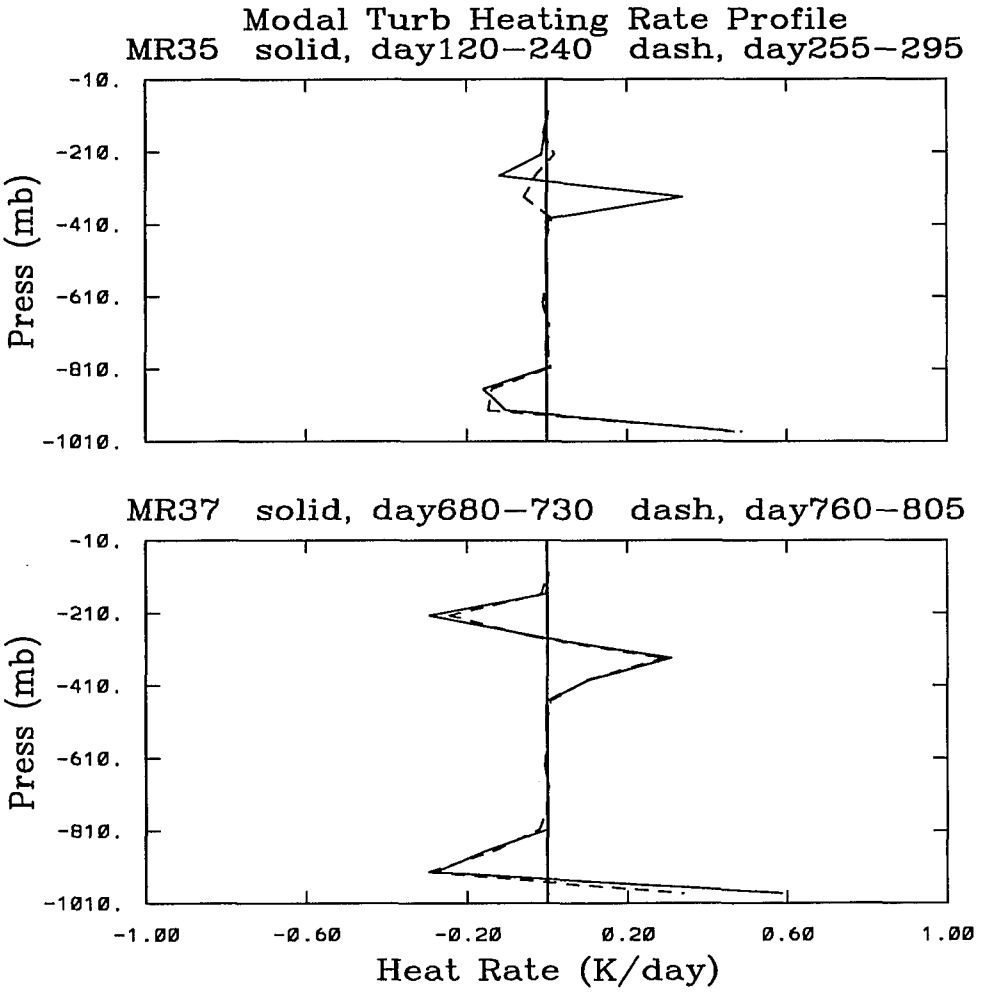

Figure 3.32 – Modal sensible heating rates for MR35 and MR37.

SWR heating near the top of the troposphere, for the low surface evaporation cases.

3.5.2 The Most Likely State for high E_v

As can be seen from the time series for θ_{250} at MR36, for a high surface evaporation and a high surface boundary temperature, the modelled atmosphere responds in a succession of transitions between cold and warm regimes, with time scales of about 30 days. It is seen from Fig. 3.26 (bottom) that almost all the precipitation is convective in nature. This section is a description of the changes in the vertical structure of the simulated atmosphere that favor such events. Since the residence time in each regime is not as long as for the E_v cases, the analysis

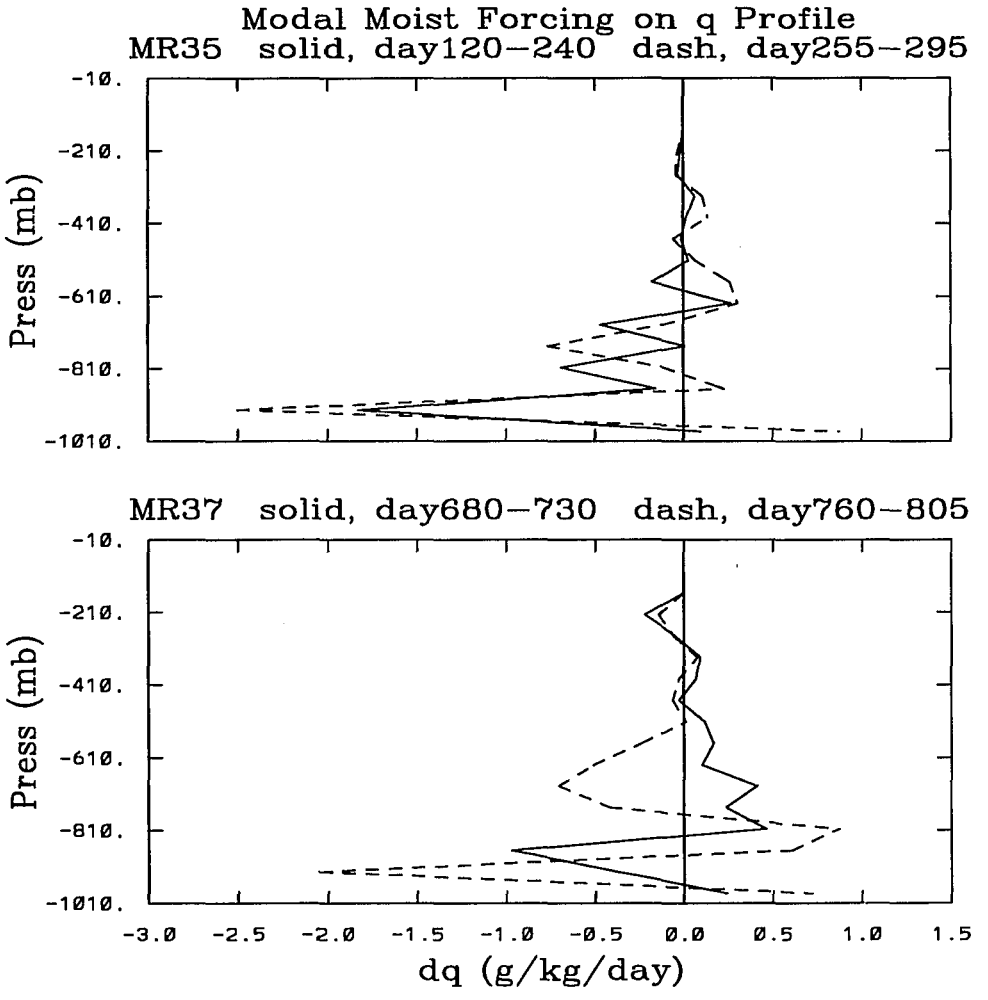

Figure 3.33 – Modal convective forcing of q for MR35 and MR37.

proceeds differently: first, a discusion of the modal vertical profiles for the prognostic variables and some of the forcing terms is included; second, a discussion of the evolution of the vertical structure, leading to the transitions, is presented.

Fig. 3.35 (top) is a plot of the distribution of all the values for the potential temperature at 334 mb, between days 601 through 1050, for both experiments with and without cyclic solar forcing (MR38 and MR36, respectively). Each graph is constructed by stratifying the values in the temperature between the minimum and maximum values, in 10 equally spaced intervals. There are 10800 sample points in this time range for each experiment. It is seen from Fig. 3.35

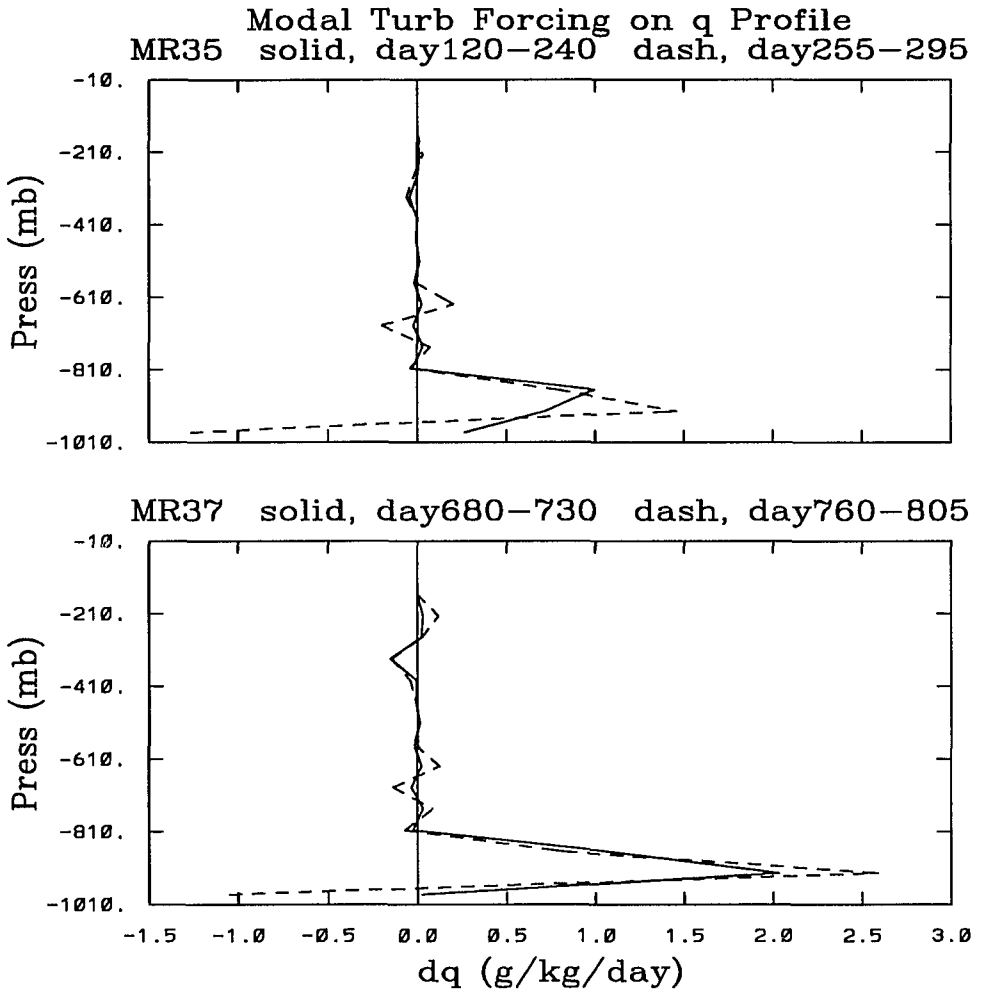

Figure 3.34 – Modal turbulence forcing on q for MR35 and MR37.

(top) that in the experiment without cyclic solar forcing (solid line, for MR36) there is one modal value, closer to the lower temperature limit. This is an indication that the colder regime has a longer residence time for the high E_v cases. Indeed, from Fig. 3.19 (top) it is seen that the potential temperature in the upper troposphere fluctuates with time scales of about 30 days, but that the colder regime has a longer residence time. The other curve in Fig. 3.35 (top) shows the distribution of values for the potential temperature at 334 mb, for the experiment with cyclic solar forcing (dash line, for MR38). There are two peaks in the distribution curve, the biggest one corresponding to the colder temperatures. Fig. 3.35 (bottom) illustrates the modal potential

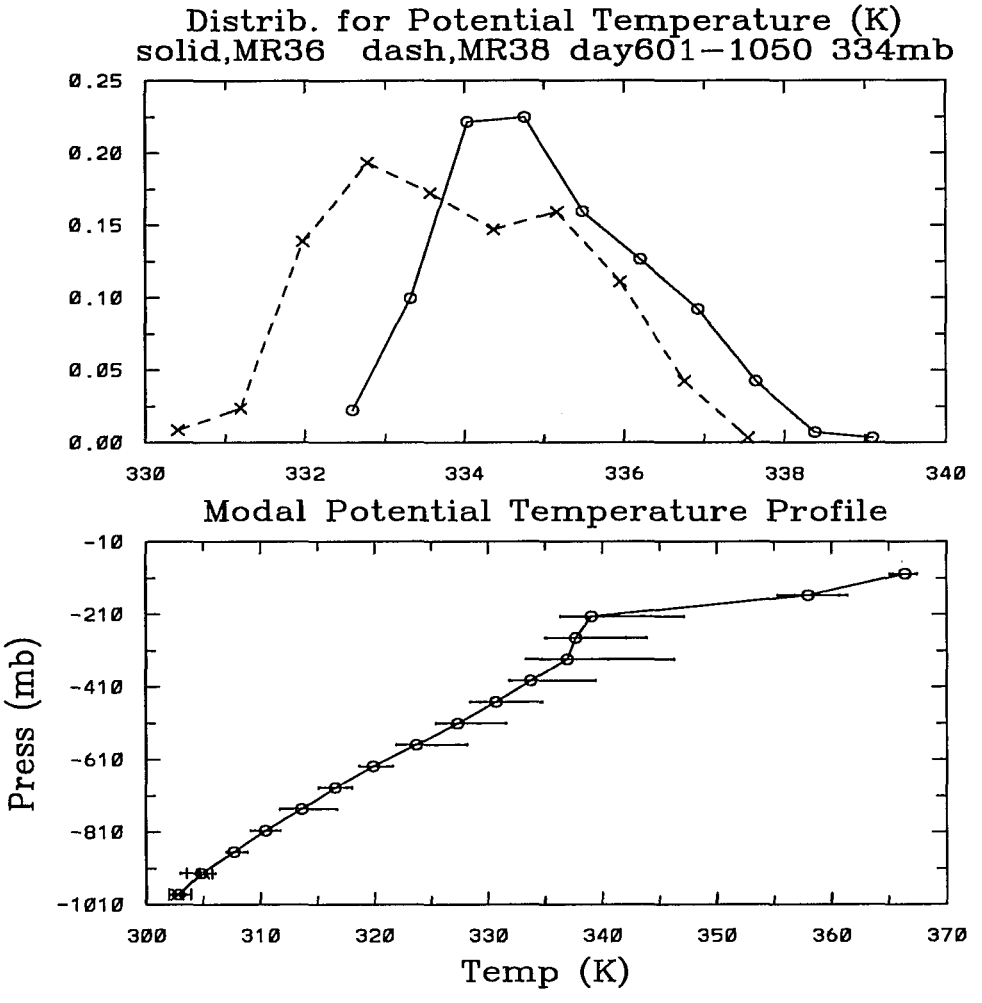

Figure 3.35 – Probability distribution of θ for MR36 and MR38. (top) Probability distribution for θ at 334 mb, for the experiments with high surface evaporation, with (dashed) and without (solid) cyclic solar forcing; (bottom) Modal θ profile for MR36, with horizontal bars indicating the spread of the values.

temperature profile for experiment MR36, and the spread of the values about the mode. The largest variability in the temperature occurs in the upper middle troposphere, and towards the warmer temperatures.

Fig. 3.36 are plots of the potential temperature (top) and the specific humidity (bottom), comparing the modal profiles for the experiments with and without cyclic solar forcing. The

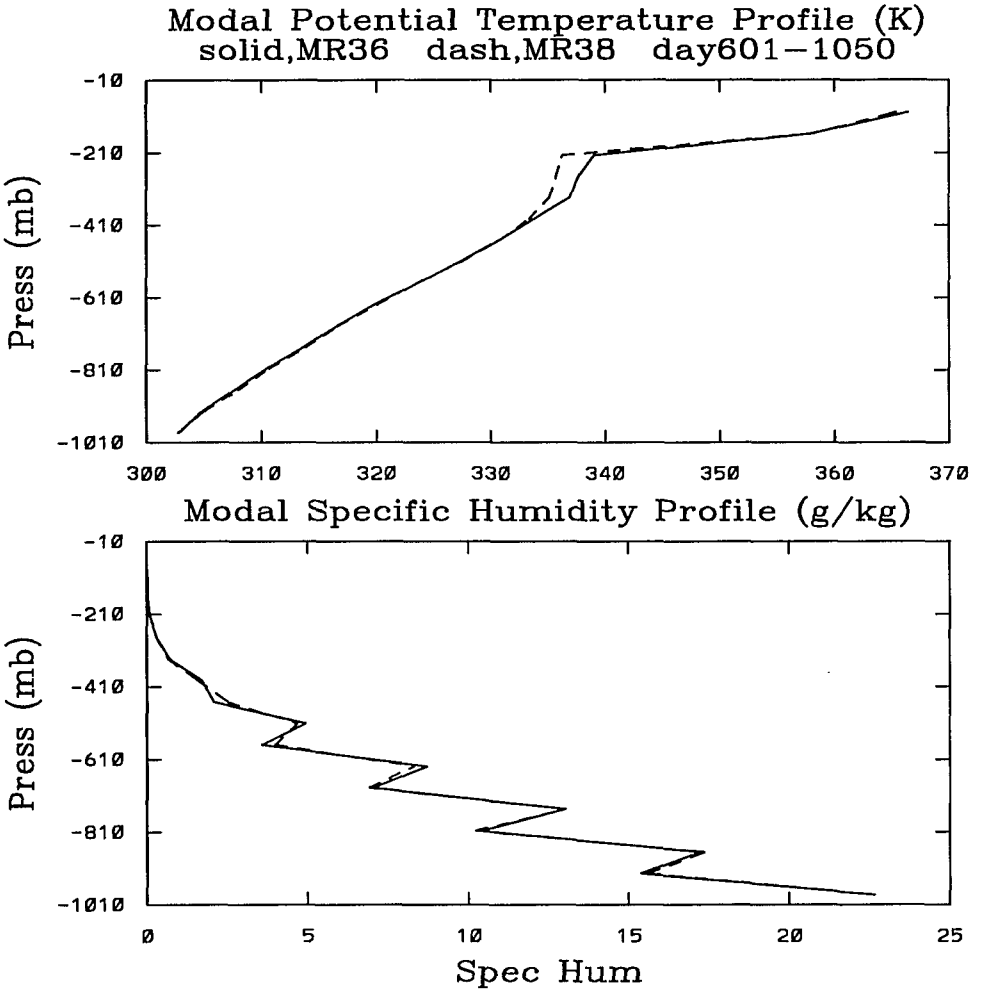

Figure 3.36 – Modal θ and q profiles for MR36 and MR38. The figures compare the typical profiles for the experiments with high surface evaporation, with (dashed) and without (solid) cyclic solar forcing.

temperature profiles are quite similar, except for the layers at 200–400 mb, and at the bottom of the cloud layer at 800–900 mb. The specific humidity profiles are very similar, with very minor differences in the layers at 400–700 mb, and at 800–900 mb. This is an indication that in this simplified model the typical specific humidity profile is strongly determined by the availability of moisture at the surface. The upper troposphere for MR38 is colder than in MR36, and is slightly warmer at the bottom of the cloud layer. It is also moistier at both layers. The extra amount

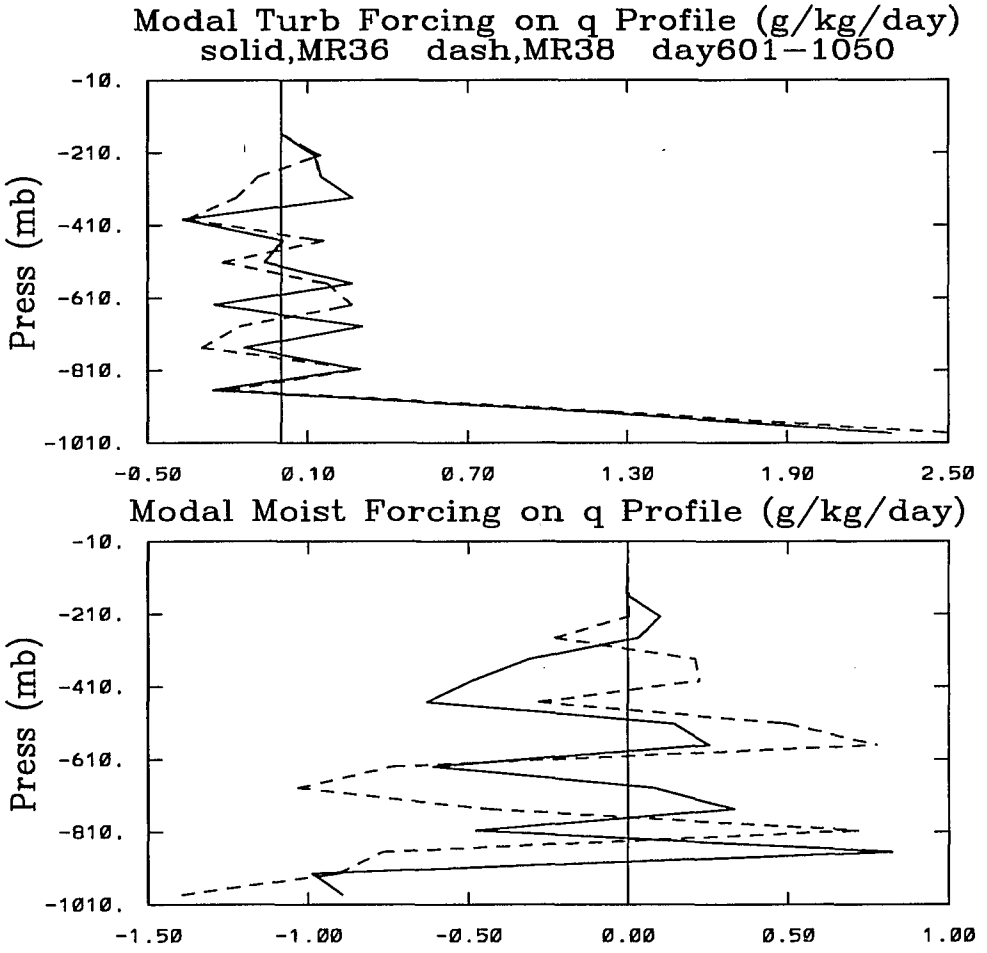

Figure 3.37 – Modal δq_{trb} and δq_{mst} for MR36 and MR38. Curves arrangement is similar to the previous figure.

of moisture in the upper troposphere is due to convective pumping, while at the cloud bottom is due to turbulent transport, as can be seen from Fig. 3.37. Absorption of solar radiation accounts for the higher temperature in the upper troposphere in experiment MR36, as seen from Fig. 3.39 (bottom). In the presence of the cyclic solar forcing, the lowest 200 mb are more active in the release of the latent heat, but the middle troposphere (i.e., the layer covering 500–700 mb) tends to evaporate more water than in MR36. The LWR cooling in the lowest 700 mb is quite effective for both experiments. For MR36 there is a window at the layer of 600–700 mb, with very little

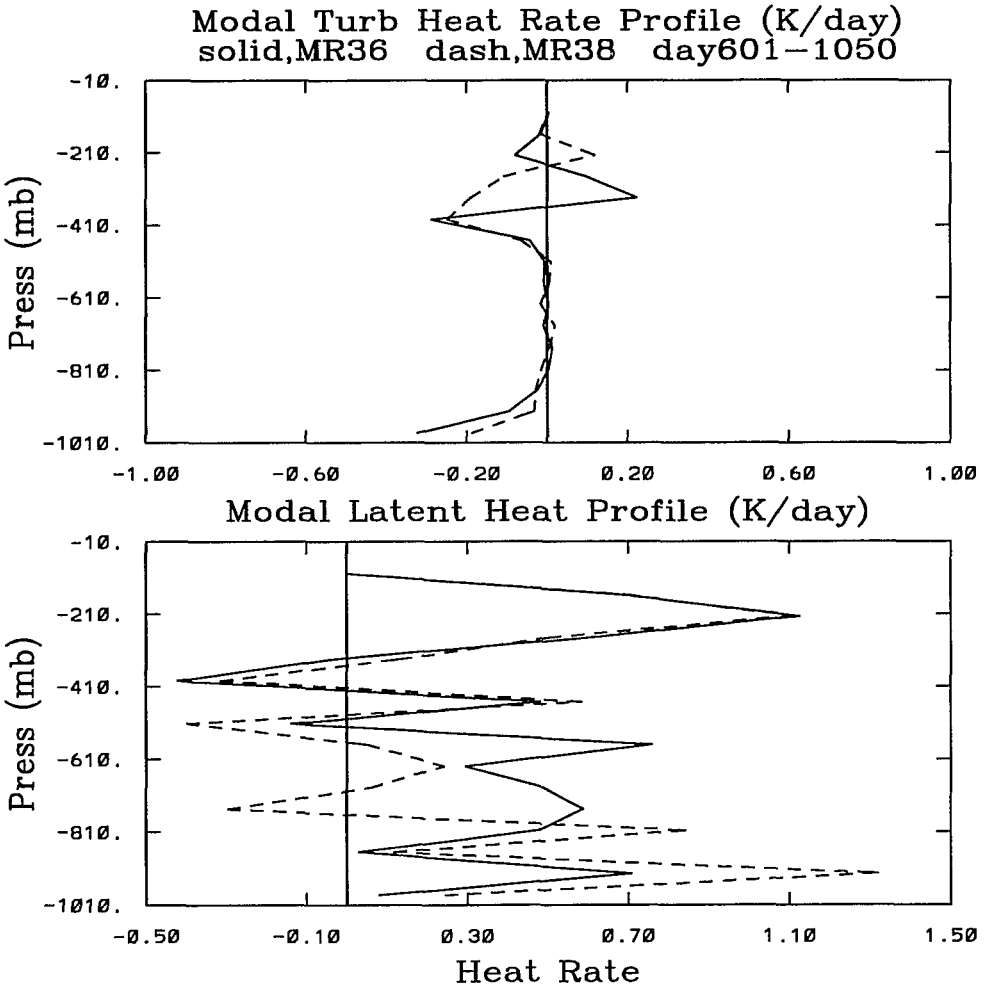

Figure 3.38 – Modal δT_{trb} and δT_{mst} for MR36 and MR38.

LWR cooling. In both experiments, the layers above 300 mb, either, cool off very little or warm up in the LWR range. Hence, the high surface evaporation cases are driven by moderately strong latent heating in the lower troposphere, radiative cooling by LWR or reduced SWR heating in the upper middle, and reduced SWR heating and LWR cooling at the top. This combination of thermal forcings provide the differential heating that excites the climate variability observed from the time series.

A comparison of the specific humidity profiles between the experiments with low and high surface evaporation, E_v, reveals that the whole troposphere gains a substantial amount of water

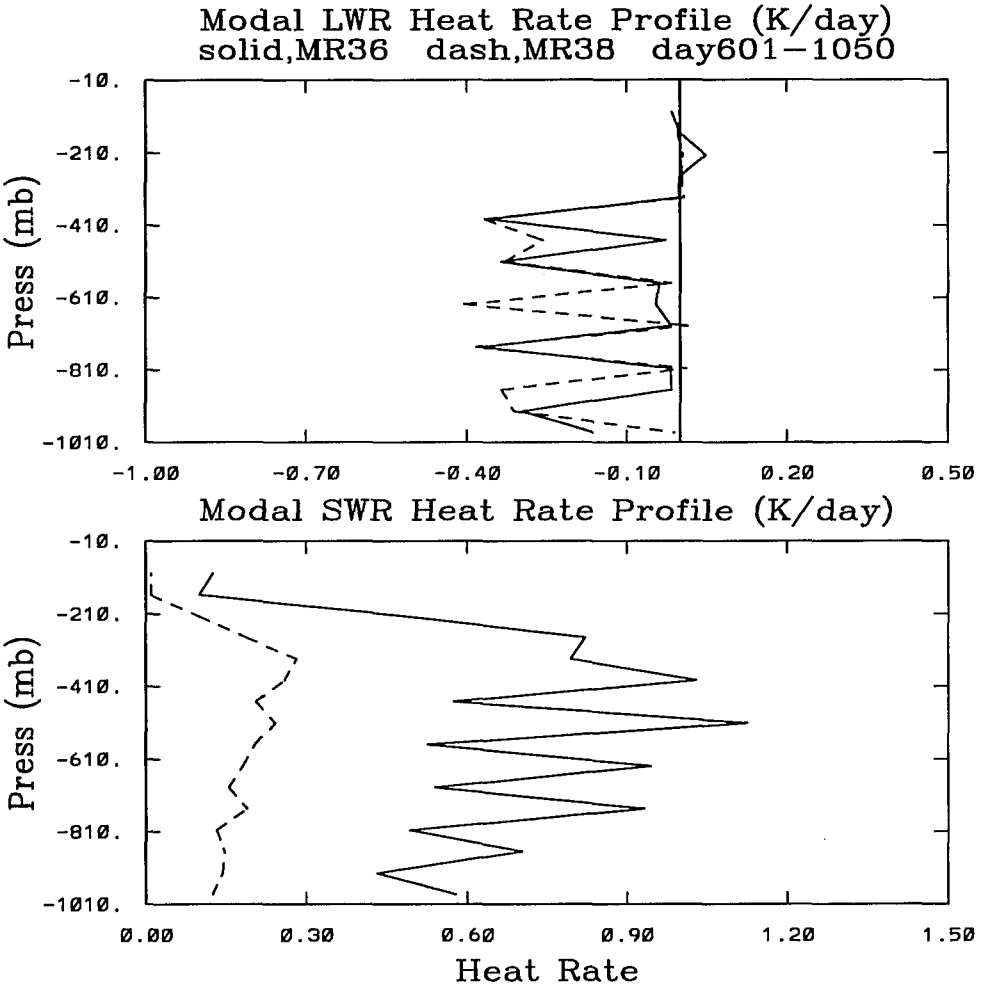

Figure 3.39 – Modal radiative heating rates for MR36 and MR38.

vapor in the high E_v cases, but the fractional increase is the largest in the upper troposphere. The largest actual increase occurs in the lowest 200 mb.

In summary, the increased water vapor of the lowest layers cause the sustained convective activity, that in turn transport more moisture to the middle troposphere. Turbulent and convective transport carry the water vapor to the topmost layers (see Fig. 3.37). The presence of the extra water vapor enhances the absorption of solar wavelengths (see Fig. 3.37, bottom panel).

This picture is, in essence, dynamically similar to the one for the low surface evaporation cases. The time of the interactions are certainly different. These seem to be dependent on the

proper accumulation of moisture in the simulated upper troposphere.

Chapter 4.

Spectral analysis of the time series

4.0 Spectral Analysis of the Time Series

The time series generated during the simulations discussed in previous chapters contain a multiplicity of time scales, most of which are not indicative of strong periodic signals. The results for those simulations with similar surface boundary conditions and upper air winds, but with different cyclic solar forcing, are similar in the mean levels of each regime, in the fluctuations within the regime with the longest residence time, in the amplitude of the fastest fluctuations, in the nature of the largest amplitude transitions, in the phase relations between different variables, and in the apparent characteristic time scales. A spectral decomposition of the time series is used to characterize quantitatively these time scales. The purpose of this section is to present the method used for the spectral analysis, the steps that were taken to ensure the self-consistency of the analysis, and some of the results.

4.1 Spectral Density Estimation

It is assumed that the time series have a continuum of component frequencies whose relative amplitudes are to be determined. Periodogram analysis can give an estimate of the mean spectral

density associated with a narrow frequency range, for which the Fast Fourier Transform (FFT) procedure is used to calculate the amplitudes. These spectral amplitudes can be used to construct weighted means of the initial spectral density estimates at desired frequency values. The new estimates are a representation of the spectral density function (SDF) for the time series. The routines of the International Mathematical and Statistical Libraries (referred to as IMSL, and documented by Gentle and Sallas in 1991) for spectral density estimation, with different spectral windowing functions, provide a flexible tool for this decomposition and analysis work. The procedure is sometimes called power spectrum analysis. In particular, only the Bartlett-Priestley window function, as defined by Gentle and Sallas [1991], is used for the results discussed in this work. Another part of the analysis is to investigate the statistical significance of the spectral estimates. The analysis of the autocorrelation function as described in Mitchell *et al.* [1966] serves this purpose.

Some terms are defined in what follows. Suppose a function of time, $Q = Q(t)$, recorded for d days at a rate of n_r records per day. The total number of existing samples values, Q_i, for $Q(t)$ is $n = n_r d$: $Q_i, i = 0, 1, 2, \ldots, n$. Suppose that a smaller set of the Q_i's is constructed from the original set, covering an equivalent **total observation time**, $\Delta t = n\delta t$, but at a slower **sampling rate**, $n_c \leq n_r$. Here $\delta t = 1/n_r$. The new **sample size** has been reduced to $N = n/n_c + 1$. The use of the FFT routines from the IMSL allows the sample size to be $N = 2^p * 3^q * 5^r$, where the set $\{p, q, r\}$ are all integers such that $p + q + r \leq 19$. Henceforth, there is quite a range of possible values for the sample size, N. In practice, however, only a few thousand points are used at a time in the FFT analysis.

From the point of view of the analysis there are three adjustable parameters for this FFT spectral estimation: the starting point of the time series, the sampling rate n_c, and the length of the series N. The first parameter is related to the **phase** of the spectral estimates, the second to the highest representable frequency (i.e., the **Nyquist critical frequency**, $f_{max} = 1/2\delta t$), and the third to the **resolution** of the frequency axis, $f_1 = 1/\Delta t$. It should be tested whether

for a particular time series the selection of the three parameters is the proper one.

The first step is to test the assumption that the length of the series is enough to describe the relevant time scales. A first trial spectral decomposition is determined from the longest possible time series for particular variables to identify the most prominent peaks of the spectral density function. A peculiarity of these spectral estimates is that the standard deviation associated with them is of the order of 100% (Press *et al.*, 1986, p. 422). There are, however, ways to overcome this defficiency partially. A spectral decomposition is performed on smaller subsets of the full time series, each one long enough to contain one or more fluctuations of the longest relevant time scales. Attention is payed to the tails of the density function for both, the smallest and largest frequencies. It is expected that some variation could occur in the location of the peaks, and that the red end of the spectrum could look somehow distorted from the first estimate. In the absence of major disagreements between the longest and the shortest time series, the ultimate goal is to obtain an average spectral density curve as suggested in Press *et al.* [1989] from the different subset's spectra. The average spectrum calculated from K separate estimates would have a smaller standard deviation than any of the original ones by a factor of $\sqrt{K}$, if they were all to have the same sample size.

The next step is to test the assumption that the decomposition algorithm does not affect the red end of the spectrum. The IMSL algorithm calculates the spectral density in a two step process: first, initial estimates are obtained from an FFT procedure on the original data; second, the spectral continuum at specified frequencies is calculated as the weighted mean of the initial estimates. The weighting function or **spectral window** uses a subset of the initial estimates, in the vicinity of the desired frequencies. One adjustable parameter is used to select the width of this subset, in frequency space. The Bartlett-Priestley window is used in the analysis because it is computationally efficient. The attention focuses on the location of the spectral peaks at the red end of the spectrum for different widths of the spectral window. The Bartlett-Priestley

window function is defined as,

$$W(x) = \begin{cases} \frac{3M}{4\pi}\left[1 - \left(\frac{Mx}{\pi}\right)^2\right] & , \text{ for } |x| \leq \pi/M \\ 0 & , \text{ otherwise} \end{cases} \tag{4.104}$$

with M an arbitrarily defined parameter, and x the difference between the desired frequency, and the actual frequency from the periodogram analysis. Notice that M defines the actual bandwidth that enters the averaging procedure: a very large value of M will imply that only a very narrow region about the desired frequency enters the calculation.

The next step is to investigate whether the sampling rate is the appropiate one to resolve the relevant time scales, particularly at the largest frequencies. The problem of the commensurability of the relevant time scales relative to the sampling rate is addressed in two ways. For strong signals with a narrow bandwidth, the sampling rate can be selected at their modal frequency to filter them out of the subsequent analysis. By filtering out the fastest frequencies the slowest frequencies are enhanced relative to the "background noise". The other alternative is to sample fast enough to resolve the shorter time scales. The use of different sampling rates is a test of the spectral estimates, particularly at the higher end of the spectrum.

Any subset of the original time series that is to be analyzed must pass a two conditions test: (i) that the sample size for the subset be of the form, $N_i = 2^p * 3^q * 5^r$; (ii) a weighted mean of the initial, $\overline{Q}_0$, and final, $\overline{Q}_N$, values of the segments must be equal, within some arbitrarily specified tolerance factor, η, $|\overline{Q}_0 - \overline{Q}_N|/\overline{Q}_0 \leq \eta$, $\eta \sim 1\%$. Hence, an algorithm was designed to select the proper subsets in accordance to the above criteria. The algorithm is started with the initial time of the subsets, and an initial estimate of the length of the series, $N_i^{(0)}$. Then, N_i is adjusted automatically until the two conditions are satisfactorily met.

The original time series are over 1.09×10^3 days long, with each variable written out at one hour intervals. These appear to have no visible trends or long term modulations that could not be resolved by a spectral analysis. For those simulations with a cyclic solar forcing, the seasonal

cycle appears to be the slowest modulation, but, still, one that is resolved within the length of the series.

4.2 Statistical Tests

The spectral density functions are tested against different kinds of "null continuum hypothesis" (Mitchell *et al.*, 1966) and statistics of significance.

Suppose N values of a generic variable Q, sampled at equally spaced intervals, of length δt, $Q_i, i = 1, 2, \ldots, N$. Define the **autocovariance of lag** m as:

$$C_m = \frac{1}{N-m} \sum_{i=1}^{N-m} (Q_i - \overline{Q})(Q_{i+m} - \overline{Q}) \tag{4.105}$$

where $\overline{Q}$ is the mean value of the series. For $m = 0$, the autocovariance is proportional to the variance of the series. The **autocorrelation function of lag** m is defined as,

$$r_m = C_m / C_0 \tag{4.106}$$

These can be calculated up to a count of $m = m_x$. A spectral decomposition of the new series for r_m, $m = 0, 1, 2, \ldots, m_x$ yields (Mitchell *et al.*1966) estimates of the spectral densities, s_k, at the frequencies $f_k = k f_1$, $k = 1, 2, \ldots, m_x$, where $f_1 = 1/2(N-1)\delta t$.

An estimate of the **equivalent white noise** level of the original series is given by,

$$\overline{s} = \frac{1}{m_x} \sum_{k=1}^{m_x} s_k$$

If the amplitude estimated at the frequency f_k is much larger than $\overline{s}$, then it can be said that there is spectral power at f_k significant beyond purely random noise.

Another test is performed to find out whether the spectral density function is a random permutation of the spectrum of an associated Markov process. For those cases when $r_1 \sim 1$, an **equivalent red noise** spectrum (or the spectrum for a process inherently dominated by persistence) can be estimated with

$$R_k = \overline{s}\, \frac{1 - r_1^2}{1 + r_1^2 - 2 r_1 \cos\left(\frac{\pi k}{m_x}\right)} \qquad \text{for} \quad k = 1, 2, \ldots, m_x \tag{4.107}$$

In principle, the relevant signals are considered to be those for which the ratio $s_k/R_k \gg 1$, whenever $r_1 \sim 1$. This criteria must be examined further. If the current spectral estimates, $s_k = s(f_k)$, are a random permutation of $R_k = R(f_k)$, then, roughly, half of the spectral estimates s_k would appear randomly distributed above and below the level indicated by R_k throughout the full frequency range. If the probability distribution for R_k is known, then an additional reference curve, $R'(f_k)$, can be constructed that includes a broader fraction of the possibly random permutations of R_k. If $\chi \equiv R'(f_k)/R(f_k)$ is chi-square distributed, then for a unique value of the cummulative probability function, $P_\nu(\chi)$, with ν the **number of degrees of freedom** in the spectral estimation, the factor χ and the 95% **confidence limits**, $R'(f_k)$, are obtained from the inverse of $P_\nu(\chi)$ and the known values R_k. A 5% confidence limit, $R''(f_k)$, is calculated as well. An estimate for the number of degrees of freedom is obtained from the total number of points used from the series, N_{tot}, and the number of spectral estimates, m_x, (Mitchell *et al.*,1966)

$$\nu = \frac{2N_{tot}}{m_x} - 1/2 \tag{4.108}$$

A more rigorous test of the statistical significance of the spectral estimates s_k above the associated red noise levels is the 95% confidence limit curve, $R'(f_k)$.

The spectral density graphs presented are all constructed in a similar way. The original time series for each variable is sampled at 3 hours intervals, each sample being the mean value for each 3 hours period. This sampling should cancel out all significant signals with a frequency of about 4 cycles/day, or multiples of it.

As seen from Fig. 4.2 (top) for θ_{250} in experiment MR35 and from Fig. 4.5 (top) for θ_{950} in experiment MR36, the spectral estimates decrease down to the white noise level for frequencies higher than about 0.6 cycles/day. For the series shown in this chapter there are no signals that stand out above the purely random noise, for frequencies above 2 cycles/day. Thus, this sampling scheme, or any other like 6, 4, or 3 samples per day (none of these is shown) is sufficient to resolve the faster time scales significant above the white noise level.

Each time series is divided in subsets, some of which may overlap. Press *et al.*[1986] suggest

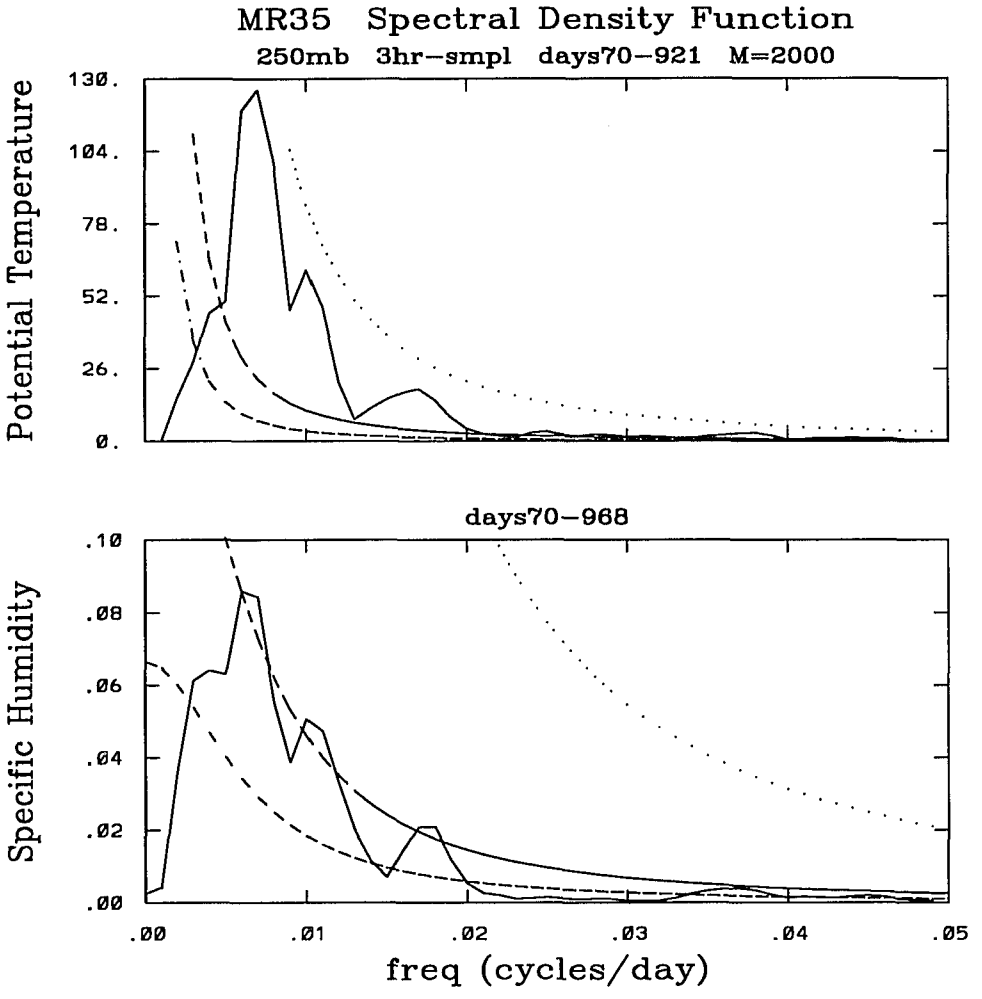

Figure 4.1 – Low frequencies SDF for θ and q at 250 mb in MR35. Spectral density function (solid) compared to the equivalent red noise curve (dashed), and to the 95% (dotted) and 5% (dash-dotted) confidence limits for θ_{250} (upper panel) and q_{250} (lower panel), for the experiment with low surface evaporation and no cyclic solar forcing. The units are K^2 – day and $(g/kg)^2$ – day for the spectral densities of θ and q, respectively, for all subsequent figures in this chapter.

the division of long time series into subsets to construct mean spectral estimates with reduced variance. Although not excluding unevenly sized subsets, they recommend the use of evenly splitted subsets with a size that is a power of two, and with overlapping halves. This technique is

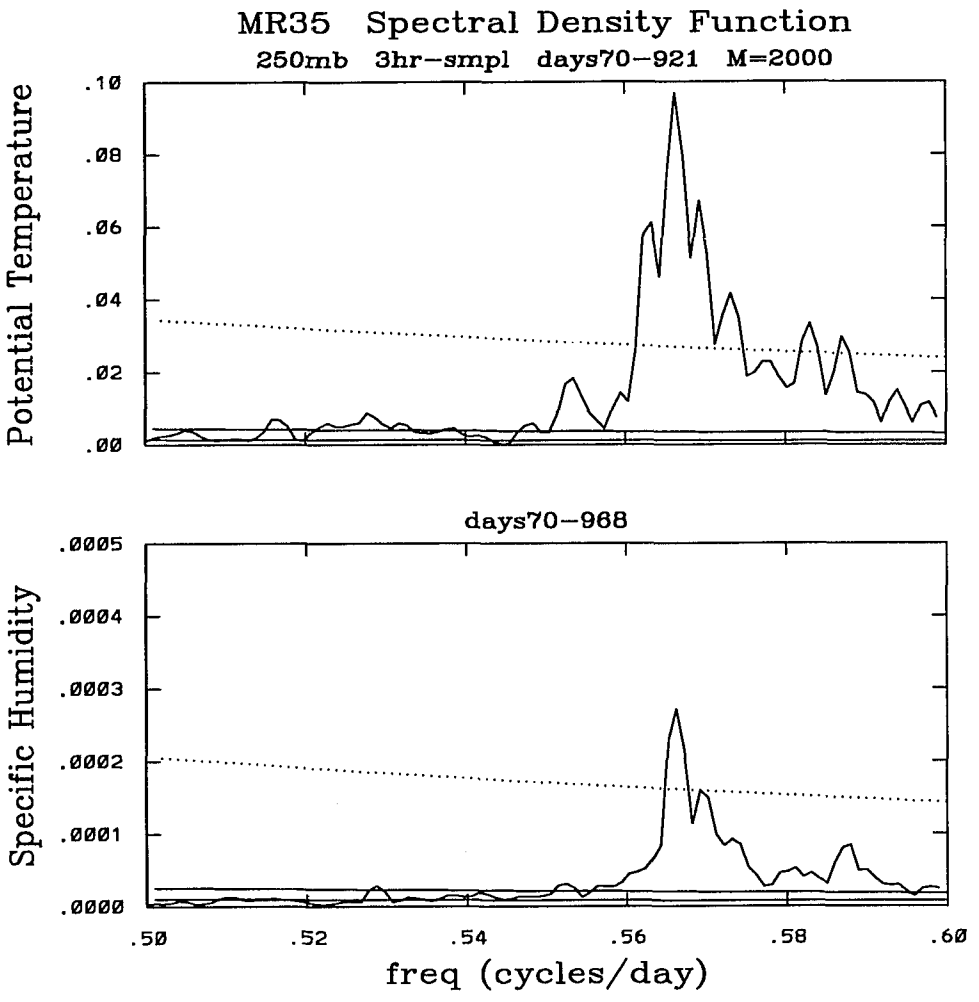

Figure 4.2 – High frequencies SDF for θ and q at 250 mb for MR35. Spectral density function (solid) compared to the equivalent red noise curve (dashed), and to the 95% (dotted) and 5% (dash-dotted) confidence limits for θ_{250} (upper panel) and q_{250} (lower panel), for the experiment with low surface evaporation and no cyclic solar forcing.

not used, in order to avoid jump discontinuities due to differences in the endpoints of the subsets, or the use of a tappering function at the ends of the subsets. For each spectral estimate shown, two to six subsets are used, each with a length adjusted according to the conditions specified in previous paragraphs.

Each of the figures contain at least three graphs: the spectral estimates, s_k (solid line); the

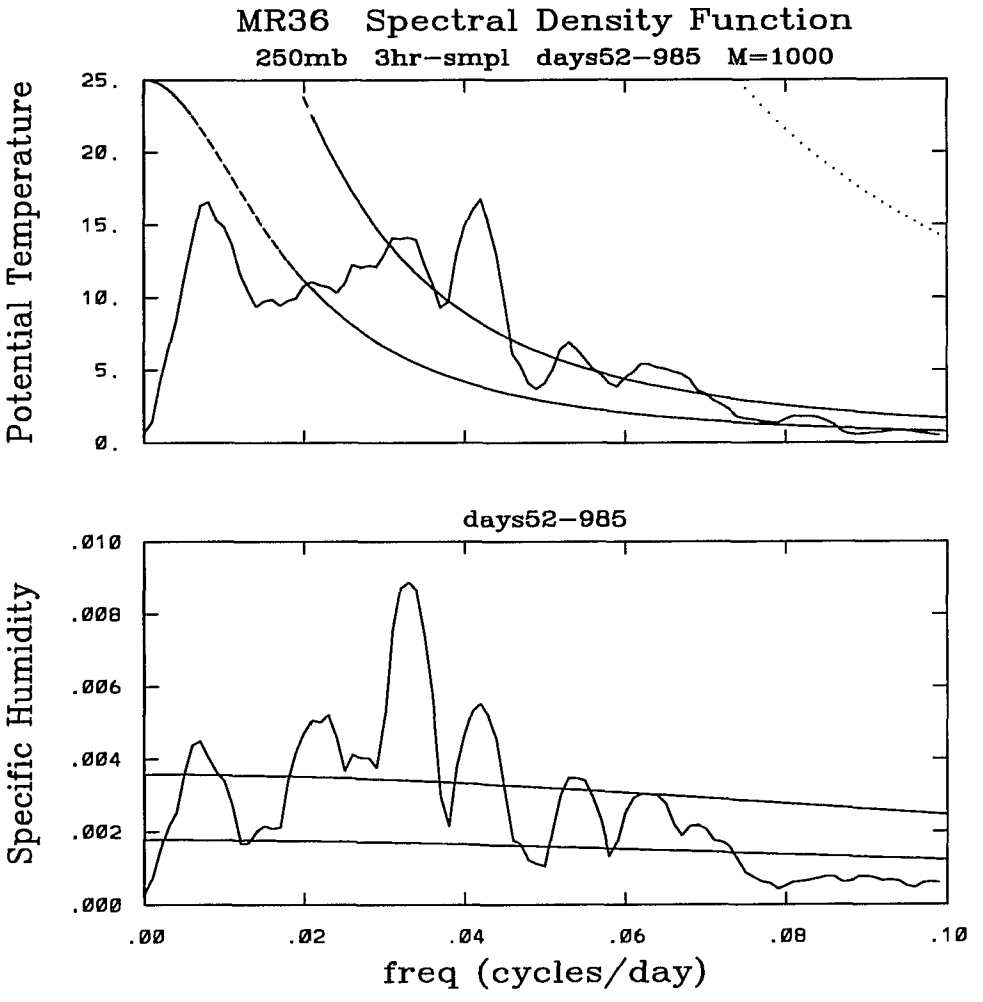

Figure 4.3 – Low frequencies SDF for θ and q at 250 mb for MR36. The identity of the curves is similarly arranged as in previous figures, but for the experiment with high surface evaporation and no cyclic solar forcing.

associated red noise spectrum, R_k (dashed line); the 5% confidence level, R_k'' (dash-dotted), and; possibly the 95% confidence level, R_k' (dotted). In some of the figures, the 95% confidence limit is not shown, as it is too high when compared to the spectral estimates for the range of frequencies on display. There are 1000 spectral estimates per unit frequency range in the figures shown.

The question may arise: why to show the figures "comparing" actual spectral estimates with their associated red noise estimates, if the comparison denies the statistical significance of the

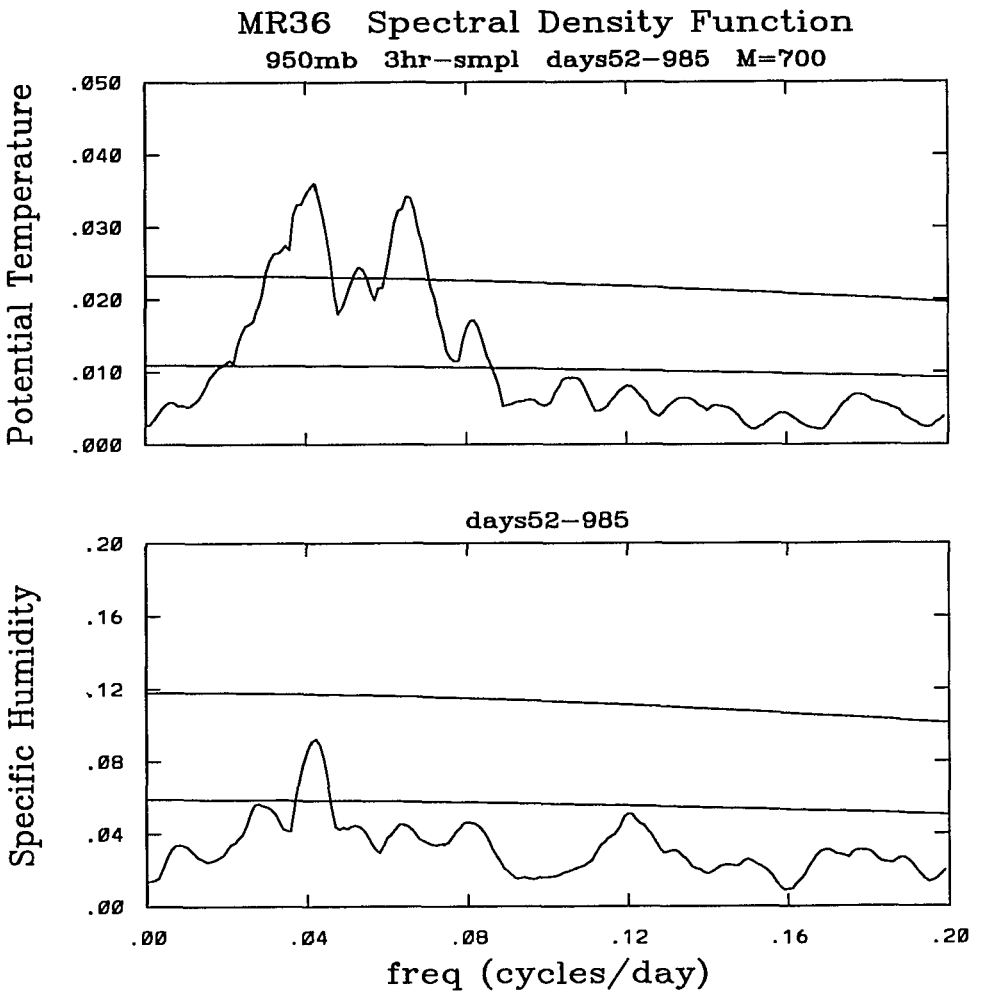

Figure 4.4 – Low frequencies SDF for θ and q at 950 mb for MR36. The identity of the curves is similarly arranged as in previous figures, but for the experiment with high surface evaporation and no cyclic solar forcing.

former? Beyond the point of making as complete a presentation of the numerical experiments' results as possible, an additional purpose may reside in several facts. On the first hand, some of the spectral estimates peaks are common to the two variables presented (as well as to others not displayed). Secondly, a visual inspection of the time series calls attention to a modulation of about one month duration, but that are not much stronger than the very short time scale variations (say, of the order of a day), or the strong episodic events discussed before. Hence, in

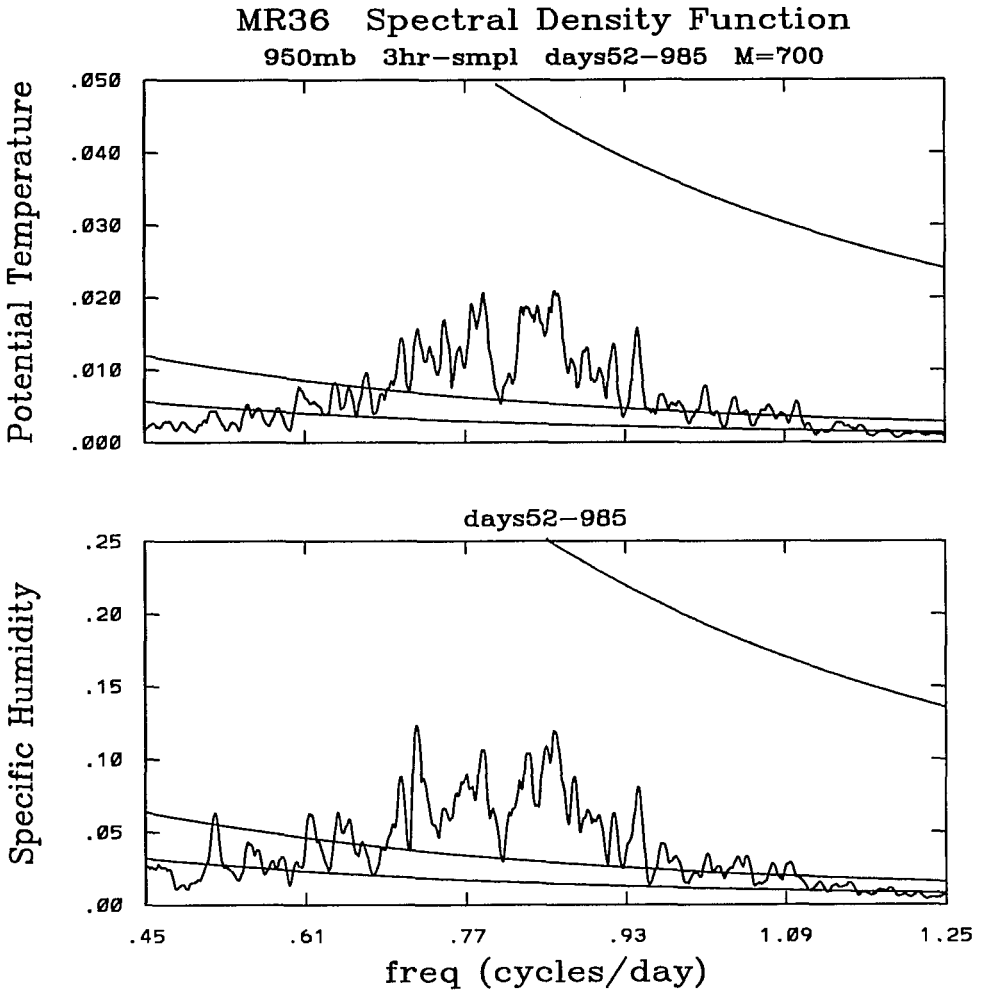

Figure 4.5 – High frequencies SDF for for θ and q at 950 mb for MR36. Upper panel for θ and lower panel for q, for the experiment with high surface evaporation and no cyclic solar forcing. The identity of the curves is similar to the previous figure.

that sense, the spectral density curves serve to quantify common time scale variabilities in the prognostic variables of these numerical experiments. Last, some spectral estimates conform to a broad band peak, that is unlikely to occur as a random permutation of an essentially flat region of the red noise. In that sense, the comparison with the red noise curve can be used as a statistical tool to judge the significance of the spectral estimates, but in addition to other comparisons and pieces of information that the original data may provide.

4.3 Spectral Density Estimates

According to Mitchell *et al.* [1966], if the non-randomness part of the spectrum for a time series are dominated by persistence, then it would be expected that the first orders of the serial correlation coefficient, $r_i, i = 2, 3, 4, \ldots$, will be comparable to the corresponding powers of r_1, $(r_1)^i$. Then, it is expected that the figure of merit $\gamma_i \equiv r_i/(r_1)^i$ should be close to unity for the case of persistence, as i is increased. For purely random signals, γ_i should increase as the successive powers of r_1 become smaller, and r_i stays constant for $i \geq 1$.

Table 4.1

Ratio of the serial correlation coefficients to persistence terms

Variable	Days	r_1	γ_2	γ_3	γ_4	γ_5
Experiment MR35						
θ_{250}	70–921	0.9996	0.9994	0.9985	0.9975	0.9965
q_{250}	70–968	0.9976	0.9991	0.9982	0.9973	0.9966
θ_{950}	28–867	0.8967	0.8702	0.6821	0.4702	0.2949
q_{950}	28–1037	0.8653	0.7921	0.4607	0.0642	-0.3326
Experiment MR36						
θ_{250}	52–985	0.9930	0.9934	0.9857	0.9777	0.9697
q_{250}	52–985	0.9432	0.9775	0.9638	0.9563	0.9563
θ_{950}	52–985	0.8341	0.6859	0.1898	-0.2667	-0.4504
q_{950}	52–1033	0.8263	0.6362	0.0284	-0.5828	-0.9209

Table 4.1 gives the values for γ_i for two different experiments without cyclic solar forcing, and low and high surface evaporation, MR35 and MR36, respectively. The two variables presented, θ and q, are examined at the upper simulated troposphere (250 mb) and nearby the

surface (950 mb). As mentioned before, the statistics of this chapter are calculated with eight (8) samples per day, which gives thousands of points intervening in the calculation of each number in Table 4.1.

For the low evaporation case, at the upper troposphere γ_i decreases very slowly for higher orders of the correlation coefficient. At the surface layer, the figure of merit decreases quite rapidly, with even an indication that the fastest time scales are of the order of 20 to 30 hours, at least, because of the sign change in γ_i. For the high evaporation case, γ_i decreases faster at the higher layer, than in the low evaporation case. The surface layer may have dominant short time scales on the order of 15 to 20 hours, but not persistence as the main form of non-randomness. It can also be seen that the moisture field near the surface is the most rapidly changing field for both experiments.

Fig. 4.1 (top) illustrates the low frequency end of the spectrum for θ_{250} in the low surface evaporation experiment. There are three signals that rise above the red noise level, centered at about 0.0071, 0.010 and 0.0175 cycles/day. The fastest frequencies with significant amplitudes are a broad band peak centered at 0.565 cycles/day, as is seen from Fig. 4.2 (top). The graphs for q_{250}, Fig. 4.1 (bottom) and Fig. 4.2 (bottom), show weaker signals at the same frequency bands. For both, θ_{250} and q_{250}, the low frequency signals do not rise above the 95% confidence level, but the fact that they appear as broad band peaks for both variables seem to suggest their significance. The higher frequency signals rise well above the 95% confidence level.

At 950 mb, the spectrum for θ_{950} has peaks at slightly higher frequencies: 0.0057, 0.0108, 0.0178 and 0.569 cycles/day, as seen from Fig. 4.6 (top) and Fig. 4.7 (top). These translate to signals centered at about 140, 100, 56, and 1.75 days. The high frequency signal has a larger amplitude at the surface layer than at 250 mb. Similar peaks can be identified for the specific humidity at the same frequency bands, although these are slightly weaker than the potential temperature ones (see Fig. 4.6 and Fig. 4.7, bottom panels).

The following paragraphs describe the spectral analysis for the potential temperature and

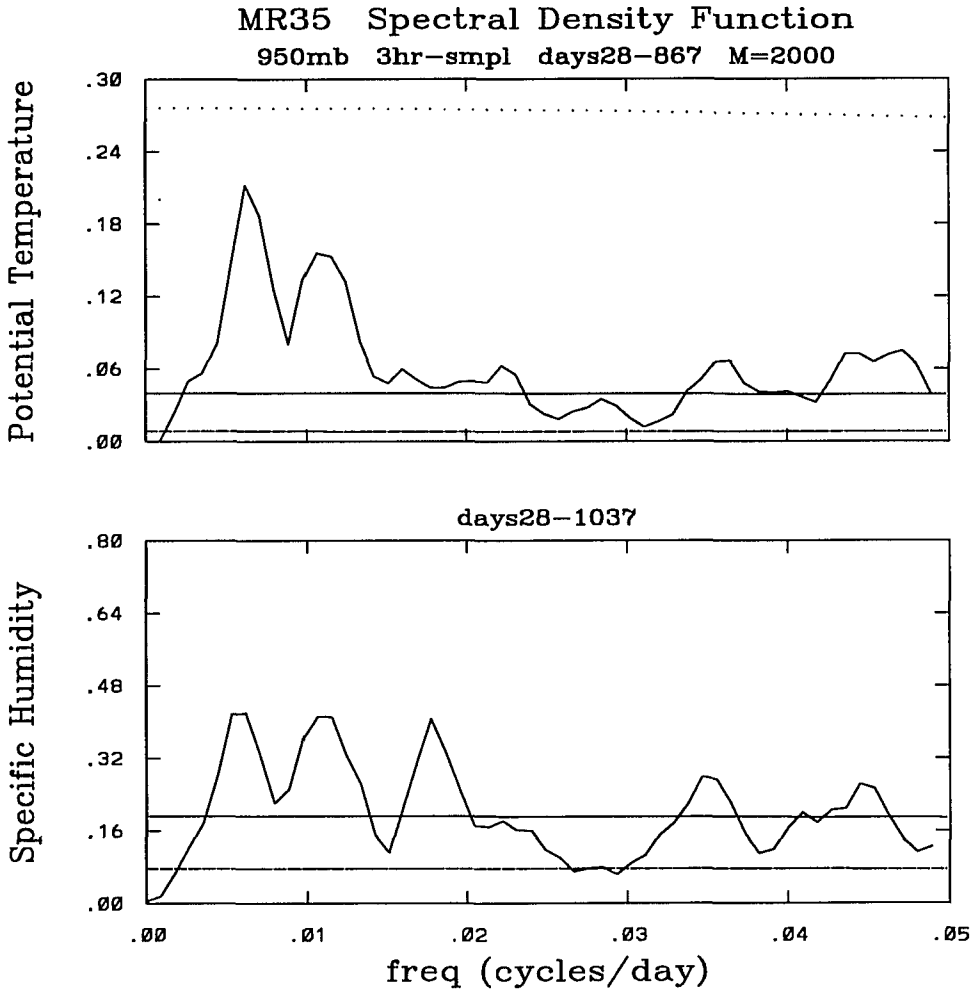

Figure 4.6 – Low frequencies SDF for θ and q at 950 mb in MR35. The identification of the curves is similar to the previous figure.

the specific humidity at the top of the simulated troposphere and near the surface layer, in the experiment with high surface evaporation and no cyclic solar forcing. The spectral density datasets were generated with 6 subsets for θ_{250} and 4 subsets for q_{250}; 6 subsets for θ_{950} and 5 subsets for q_{950}, from the original time series. Fig. 4.3 illustrates the low frequencies part of the spectrum for θ_{250} (top) and q_{250} (bottom), respectively. The most prominent peaks at 250 mb appear centered at 0.022, 0.035, 0.042 and 0.055 cycles/day. These translate to peaks centered at about 45, 28, 24 and 18 days. There are no significant signals at higher frequencies.

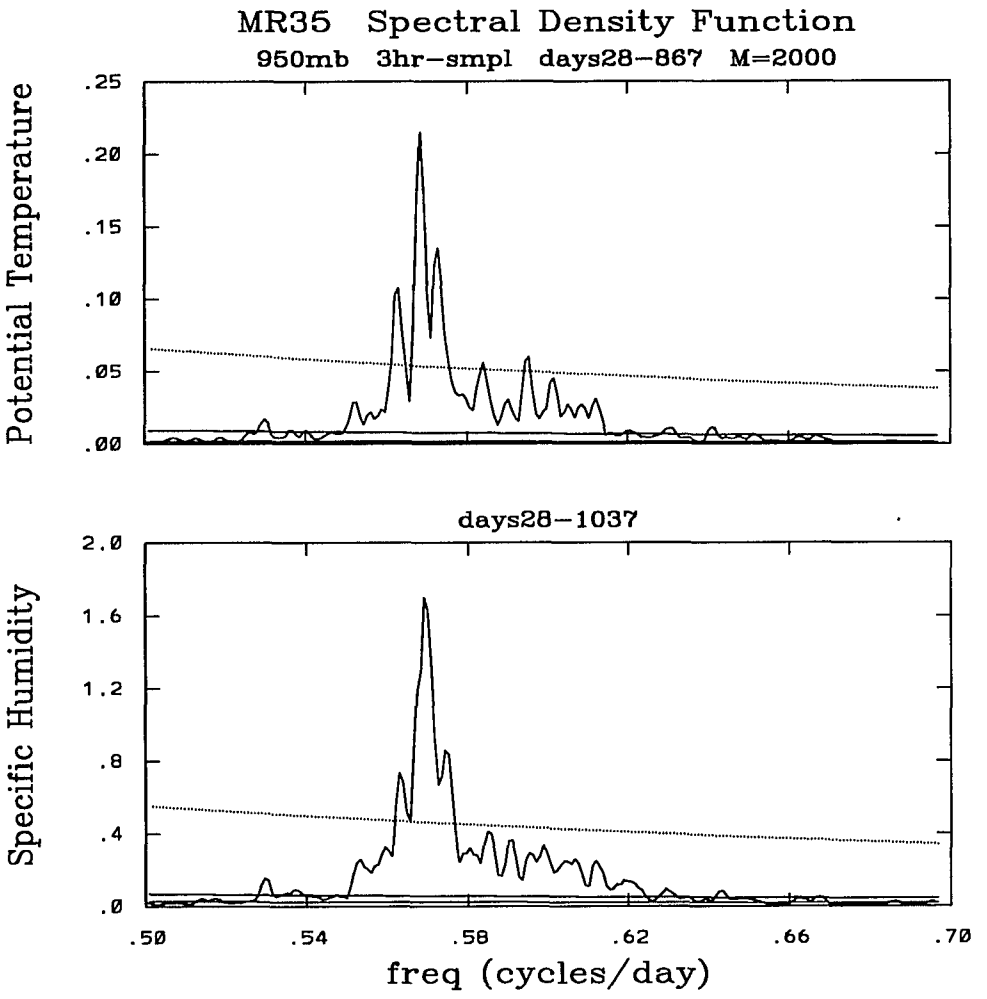

Figure 4.7 – High frequencies SDF for θ and q at 950 mb in MR35. The identification of the curves is similar to the previous figure.

Near the surface layer, Fig. 4.4 for the low frequencies, and Fig. 4.5 for the higher frequencies, illustrate the spectral density functions of θ_{950} (top) and q_{950} (bottom), respectively. Only two signals rise above the red noise level, centered at about 0.040 and 0.065 cycles/day. The higher end of the spectrum encompasses a broad number of signals in the range 0.69 to 0.97 cycles/day, rising above the red noise level, but not above the 95% confidence level.

This simple spectral analysis has confirmed the presence of variabilities in the order of 40–60 days, for both, low and high surface evaporation experiments. It must be noticed, though,

that many of these spectral peaks do not pass the 95% red noise confidence interval criteria. There is also, a rather strong short convective adjustment time scale of about 1–2 days in the low evaporation case. The high evaporation case does contain a broad band peak in the same frequency range, but it is not so sharply defined. In both cases, the surface signature of the high frequency signals is stronger than the upper troposphere's.

The spectral estimates could have covered a broad range of frequencies, from the 4 cycles/day down to the 0.005 cycles/day, because of the extra care taken in obtaining long enough time series with good time resolution. It has been shown that the signals, if any of relevance that could appear by using this type of analysis, were constrained to narrow regions. The consequence of this is that the actual fraction of the total variance explained by these spectral estimates is rather small.

Chapter 5.

Physical processes and the transitions between regimes

5.0 Physical Processes for the Generation of the Cooling Episodes

The results for the numerical simulations have been characterized for all cases as oscillations between two convective regimes. These fluctuations appear to have time scales between 20 to 50 days under prescribed conditions of high surface evaporation and warm surface water at $T_s = 30°C$, even in the absence of the simulated periodic forcing of the seasonal and the diurnal solar cycles. These convective climate regimes of the entire column can be described in simple terms as: (i) a warm and moist regime; (ii) a cooler and drier regime. There are, however, many other differences in the properties of the two regimes. As an example, in the low wind cases, MR35 and MR37, the warm and moist regime has a longer residence time. In the high wind cases, MR36 and MR38, both regimes have similar residence times. The purpose of this chapter is to characterize the transition between the regimes in terms of the physical processes that take place in the simulated atmospheric column, with the underlying intention of clarifying an understanding for the particular dominant time scales.

In general, either of two points of view could be adopted upon trying to explain these

transitions: (i) the aperiodicity in the rate of change of the system variables is the cause for the transitions; (ii) the favorable dynamical conditions and the vertically coherent variations along the atmospheric column is the cause for the transitions. The following paragraphs will clarify what is meant by each one of these points of view.

Lorenz [1965] asserted, in general, that atmospheric time series tend to be aperiodic. The perturbations of varying short and extended time scales, from the long term mean, are perceived as the aperiodicity of the time series. Any given variable used to describe the general circulation of the atmosphere can be resolved into a mean flow, plus the periodic components, plus the anomalies. For any such variable the problem lies in the non-negligible amplitudes and spatial structure of all its components. The concept was that the aperiodicity came from the instability of the mean flow, from the instability of the periodic circulations (whether annual, diurnal, etc.), and from the persistence of certain physically based dynamical conditions. Quoting from Lorenz [1965]:

> "It thus appears that extended-period fluctuations of the type appearing in Figure 1 and Figure 2 are to be expected in any aperiodic process in which high persistence, as measured by a high serial correlation coefficient at a single lag, is present. The only required physical cause, other than the cause of the aperiodicity itself, is the cause of the persistence."

The second point of view considers the atmosphere as a dynamical system. The states of this dynamical system are represented by some statistical properties that obey a number of conservation laws at any given instant, although the system can appear chaotic. The transitions between different states or between different regimes follow specific, albeit unknown, dynamical laws. The discussion of results contained in this chapter will adhere to the second point of view, with the intention of identifying the physical mechanisms that drive the transitions between regimes and the relevant time scales for the simulated system.

It should be mentioned, parenthetically, that the two points of view are not mutually ex-

clusive. Lorenz [1965] asserted that any physical process causing extended-period fluctuations in the circulation of the atmosphere also will lead to the persistence of the time series.

The time series for the potential temperature, θ, at 250 mb during the experiment with high boundary temperature, low upper air wind speed, and no seasonal or diurnal solar forcing (i.e., MR35), clearly depict the climate regimes and the transitions between them. The time series for MR35 can be separated into: (i) a slow build-up phase during the warm regime; (ii) a fast cooling phase; (iii) a slower cooling and final cooled phase; (iv) and a fast warming and build-up phase. The relatively long residence time in each regime allows for a consistent definition of the statistical properties of each regime and the typical chain of events that comprise each regime in MR35, as shown in section 3.5.1. The discussion will be focused on the results of this particular experiment.

Fig. 5.1 summarizes a description of the two regimes in terms of θ_{250} and the vertically integrated mass of water vapor in the column for experiment MR35. Each point coordinates represents the mean value for a 42 hours period, during the whole integration time. As it is seen the regimes appear as a region or area of limited extent in phase space, where the system is most likely to be found. Other points are representative of the transitions between regimes.

The strong cooling episodes of the numerical experiment MR35 are generated as an interaction of surface processes and an upper troposphere's radiative response to the presence of larger amounts of moisture aloft. The presence of water vapor has a double effect in the thermodynamic response of the simulated atmosphere: it enhances the thermal inertia by means of a larger specific heat of the moist air, while, at the same time, it also enhances the absorption of long and short wave electromagnetic radiation. The transitions are described in terms of the general features that characterize the surface signature of the regimes, and in terms of a simplified conceptual model of five layers to visualize the vertical dynamics that give rise to the events.

In essence, the AGCM-1D for experiment MR35 has a fixed air mass areal density for the simulated atmospheric column, Π/g, and a fixed surface temperature, T_s. For high enough

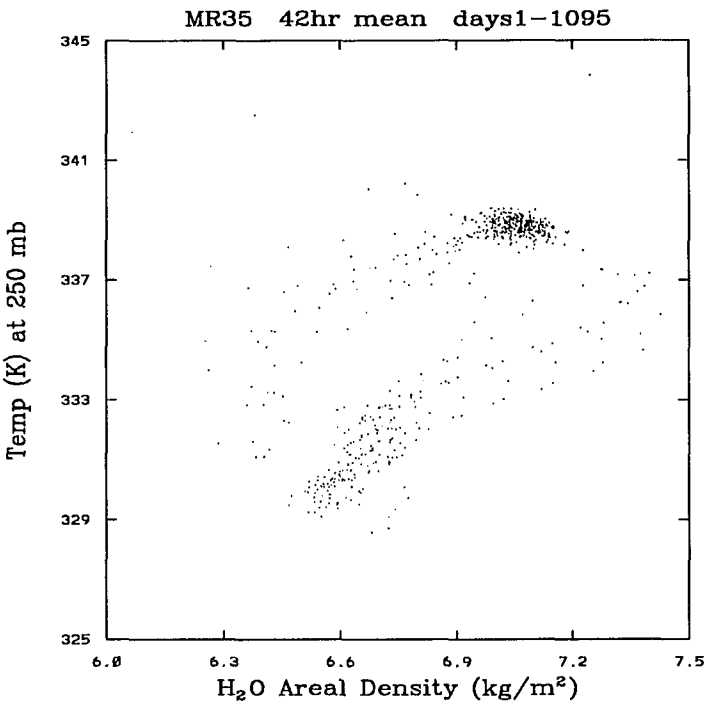

Figure 5.1 – θ_{250} and the water vapor areal density for MR35. The coordinates of each point are the potential temperature at 250 mb, and the vertically integrated water vapor mass in the simulated atmospheric column, both quantities being the mean over a 42 hour interval.

surface temperature, $T_s \approx 303$ K, and moderate winds aloft ($||\vec{U}|| \approx 3.5$ m/s), the non-vanishing surface evaporation maintain a moist planetary boundary layer (PBL) in the lowest layers, with a typical specific humidity of about 18.5 g/kg at 950 mb (see Fig. 3.28). The surface moisture is transported upwards to the higher layers by turbulence and thermal instabilities during the warmer phase (see Fig. 3.33 and Fig. 3.34).

The surface evaporation in the warm regime has a mean of 1.1 mm/day, a maximum of 1.45 mm/day, and a minimum of about 0.98 mm/day. The evaporation has the lowest values during the cooling regime, but increasing monotonically from 0.98 mm/day up to 1.1 mm/day. The evaporation suddenly increases to 1.6 mm/day during the initial warming up phase.

The water vapor areal density can be defined as the vertically integrated water vapor density

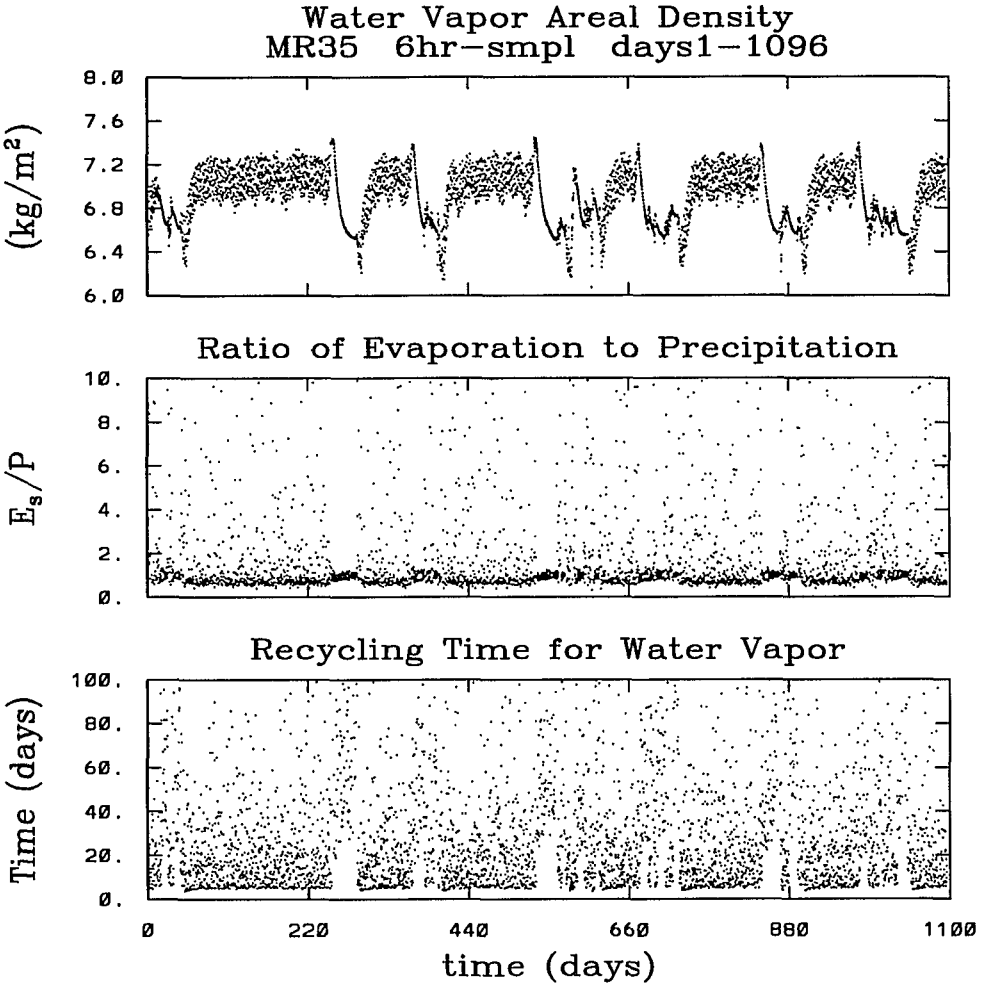

Figure 5.2 – Water vapor areal density for MR35. Time series for the total precipitable water (upper panel), the ratio of the evaporation to precipitation (middle panel), and the recycling time for water vapor (lower panel), for the low wind experiment.

(and sometimes called **precipitable water**). Two distinct regimes can be recognized in the areal density plot with a mean of about 7 kg/m^2, as seen from Fig. 5.2 (top). The warm regime has a mean areal density of about 7.1, a minimum of about 6.9, and a maximum of about 7.25 kg/m^2. This is a relative variation of less than 5% during the warm regime. The small slope of the areal density as a function of time during the warm regime is indicative of the net moisture build-up in the column. During the other regime the areal density decreases monotonically from about 7.4

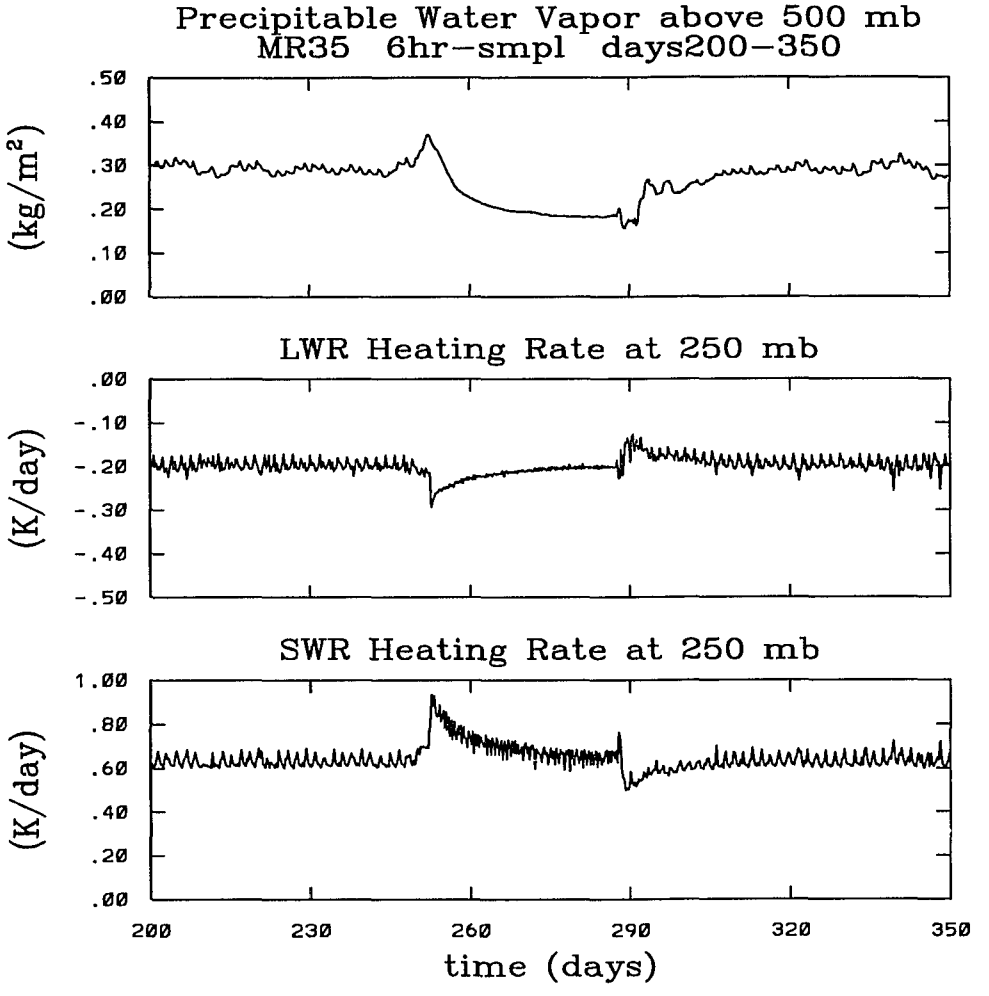

Figure 5.3 – Upper tropospheric precipitable water vapor in MR35. Precipitable water vapor above 500 mb (upper panel), LWR (middle panel) and SWR (lower panel) heating rates for MR35, during days 200 through 350.

to 6.5 kg/m^2. This is a monotonic reduction of about 8%, as seen, also, from Fig. 5.2 (top). The cooling phase is preceded by a fast increase in the areal density at the end of the warm regime, that extends for about 10 days (see top of Fig. 5.3). The upper troposphere gains 30% more water vapor mass in the 10 days period. At the end of the transition it has lost some 50% of its total water vapor mass.

During this fast moisture building phase, the nearly regular variability (of about 42 hours)

in the short and long wave heating rates at 250 mb is disturbed (see middle and lower panels of Fig. 5.3). While the mass of water vapor in the upper troposphere builds up, δT_{250}^{SWR} is enhanced significantly by about 30%, and $|\delta T_{250}^{LWR}|$ by some large fraction as well (about 50%). Hence, the upper part of the simulated troposphere warms up radiatively while it gains moisture rapidly. This is an indication that water vapor in the column increases after a positive feedback is established between the water vapor at the upper troposphere, the upper troposphere's temperature, and mostly, the absorption of SWR (see Fig. 5.3). It is seen, also in the same figure, that the initial warming phase is preceded by a noisy but significant reduction of the water vapor areal density beyond the lowest level attained during the initial cooling phase, that last for about 5 days. The same period is accompanied by lower LWR cooling (a 25% enhancement) and a weakened SWR heating rate (a reduction of about 25%). In terms of the radiative forcing, the upper troposphere is not warming up as well in the absence of substantial amounts of water vapor. Thus, this dry upper troposphere cools off or warms up faster than a moist troposphere because of the lower specific heat, and a lesser efficient radiative heat trap at the top.

The analysis of the surface evaporation and the water vapor areal density allows the following conclusions: (i) the entire column of the simulated atmosphere dries out substantially during the cool regime; (ii) the warm regime is a moisture loading phase under a rather sustained evaporation; (iii) hence, although the evaporation is non-vanishing, the water vapor is recycled by the column with different characteristic time scales during each regime.

Three questions arise: (i) what is the typical recycling time for the water vapor in the column?; (ii) how is the moisture being transported to higher levels?; (iii) what are the storage layers for the extra moisture gained during the warm loading regime?

From a comparison of Fig. 5.2 (top) and Fig. 5.3 (top), it can be concluded that half the variation of the total water vapor areal density during a transition between regimes occur above the 500 mb layer. The simulated upper troposphere appears as the storage layers for the extra water vapor. On the other hand, a comparison of the same figures also indicates that the

variability of the total mass of water vapor in the column during the warmer regime occurs mostly in the lowest 500 mb of the simulated troposphere.

A conservation equation for the total mass of water vapor per unit area, can be phrased as follows, in the absence of horizontal moisture convergence through the lateral boundaries of the vertical column,

$$\frac{\partial Q}{\partial t} = \rho_w (E_s - P), \qquad Q \equiv \frac{\Pi}{g} \int_0^1 q d\sigma$$

Here Q is the areal density of water vapor in kg/m^2; E_s is the surface evaporation and P is the net precipitation, both in mm/day; ρ_w is the water density at the surface in kg/m^3; and q is the specific humidity at the level σ. To obtain a definition of the **recycling time** for Q, τ_w, assume that the net precipitation is proportional to the amount of water vapor in the column,

$$P = \alpha Q + \beta,$$

with α, β, and E_s constants. This assumption can be justified as follows: for small amounts of water vapor in the atmospheric column the precipitation can be at most equal to the evaporation (i.e., $\beta \leq E_s$), and as Q slowly increases, so should P under a near equilibrium condition. In the real atmosphere, other processes intervene to increase or deplete the mass of water vapor in the column, like the horizontal convergence of moisture, the vertical transport of moisture, or the evaporation of the precipitation. In these simulations the horizontal convergence and the vertical transports are not included. In this formulation of the conservation principle for the areal density of water vapor $(\rho_w \alpha)^{-1}$ plays the role of an e-folding time for the areal density. This is a measure of the recycling time, τ_w, for Q. An estimate of τ_w can be posed as,

$$\tau_w \equiv (\rho_w \alpha)^{-1} = \frac{Q}{(P - E_s)\rho_w}$$

For $E_s \neq P$, both constant, τ_w is larger for a moist atmospheric column, and small for the driest atmosphere; during intense precipitation events with E_s and Q constant, τ_w will be small; as $P \rightarrow E_s$, then $\tau_w \rightarrow \infty$ (i.e., the case of an efficient moisture depleting atmosphere). This quantity, τ_w, characterize the efficiency of these moisture depletion processes.

The convective processes during the cool regime are highly efficient in depleting water vapor from the simulated atmospheric column, as seen from Fig. 5.2 (bottom). The warm regime has a typical recycling time of about 5 to 10 days. During the warm regime there are instances when moisture depletion occurs quite rapidly as seen from many small values for τ_w. The values of τ_w during the colder regime are typically in the 40 to 60 day range. As seen before, there is no stratiform precipitation during the cool regime. Even though, as seen from Fig. 5.1, the region of phase space corresponding to the colder regime is wider than the region corresponding to the warmer regime, the (surface) precipitation signature is rather narrowly defined. The colder regime is more of a collection of coherent convective states, in which $P \approx E_s$ (see middle panel of Fig. 5.2).

Several features are noticeable from a plot of the ratio of the evaporation to the convective type of precipitation, E_s/P_c, like: (i) during the warm regime E_s is at times much larger than the precipitation; (ii) most of the time, in either warm or cool regimes the ratio is about 1.0 ± 0.7; (iii) during the cool regime the ratio has a much narrower range of values of about 1.0 ± 0.3, and very seldom any values larger than 4. In the cool regime the moisture is depleted in a sustained phase of convective precipitation, with an intensity of about 1.2 ± 0.3 mm/day and not in individual rain events that flush the water out of the column.

Hence, as it has been discussed, whenever the simulated atmosphere is warmer on the average for an extended period of time, it tends to be moistier, and the variability in the total mass of water vapor occurs mostly in the lowest part of the troposphere, with typical recycling times of about 5 to 10 days for the vapor in the column. As the upper troposphere gains water vapor, the system is driven towards a different region of phase space where the typical recycling times for water vapor are much larger. Roughly, then, half the variability in the total mass of water vapor occur in the driest parts of the troposphere. In the new regime, the entire column seems to be convectively active in the recycling of the input vapor from the surface. As a consequence, each layer looses water in a sustained precipitation process. It is noted, also, that these convective

processes exchange water vapor between neighboring layers, still transporting water vapor to the upper layers.

At this point in the presentation, it would be convenient to develop a simplified conceptual model of the dynamics of these regimes, and of the transitions between them. This simplified model will consist of some five layers distributed between the surface and up to about 100 mb. Each layer, with an extension still unspecified, have uniform properties, but perhaps distinct from the other layers. In the process of describing these, it will become clear how the radiative processes enter the dynamical picture.

During the warm regime the lowest two layers load up to near saturation sooner than the upper ones; the precipitation of convective and stratiform types unloads a large fraction of the excess moisture gained during the "day". The convection restores stability to the simulated atmospheric column, but does not extend frequently all the way to the top of the moist column at about the 200 mb level. The convective activity extends most of the time only to the lowest 600 to 700 mb of the column. The upward transport of moisture continues as fueled by the surface evaporation and, in part, by local instabilities that induce mixing and local overturning of the lowest layers. The convective activity is dominated by short time scales and consequently, the signature of the surface evaporation, the surface air temperature, the convective scale precipitation, the stratiform precipitation, and the sensible heat flux are rather noisy and without noticeable long term trends. The short time scales of this regime are, perhaps, referred to as the *adjustment time* of the column in Arakawa and Schubert [1974]. The spectral analysis of the time series for the evaporation shows that the dominant time scales of the surface phenomena are about 1 to 2 days (see Fig. 5.5). The amplitudes for other smaller frequencies are recognized, but none is as large as the 1 to 2 day signal. These lowest layers extend to about the 800 mb level. Between 900 and 500 mb the net heating is dominated by the latent heat released from the convective activity (see Fig. 3.31).

The saturation specific humidity during the warm and moist regime fluctuates between 18.8

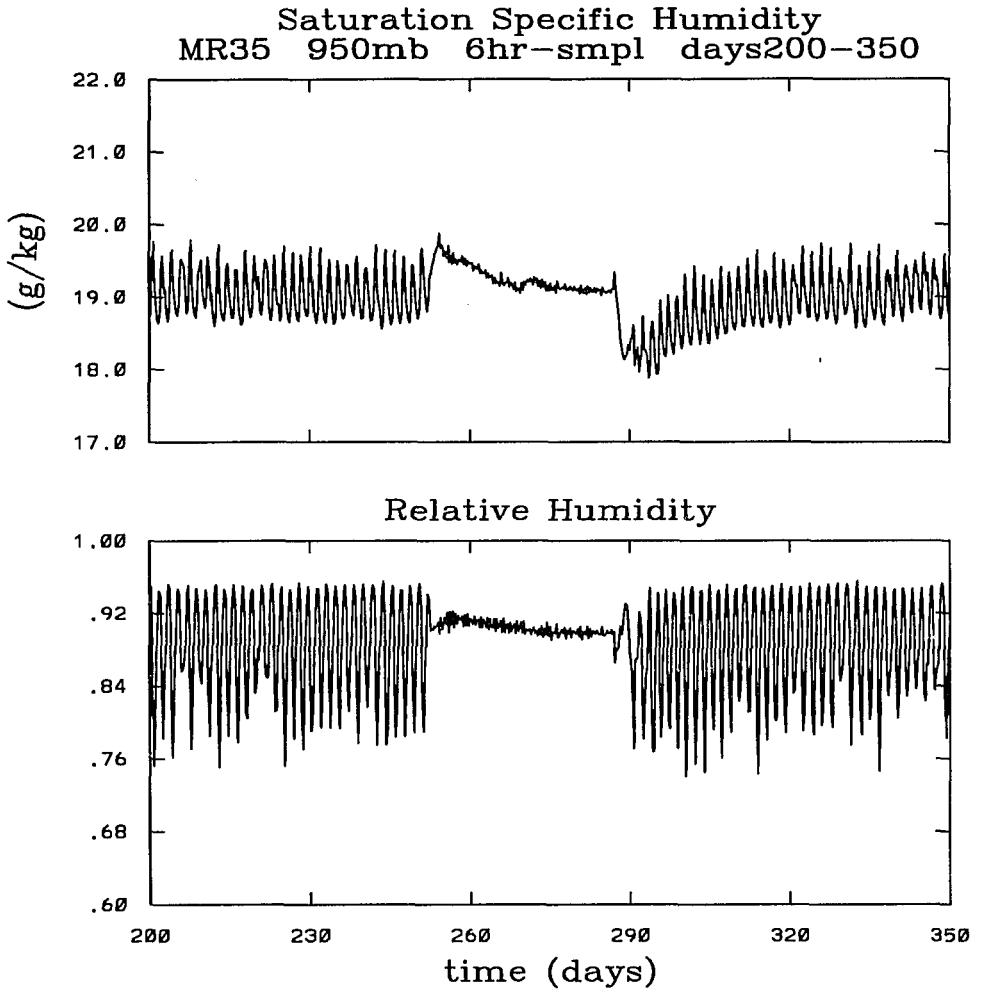

Figure 5.4 – Saturation and relative humidity at 950 mb for MR35.

and 19.8 g/kg at 950 mb (see top panel of Fig. 5.6). During the fast cooling phase the saturation specific humidity decreases monotonically from 19.9 to 19.3 g/kg, and with a very small variability of about 0.1 g/kg. The relative humidity at 950 mb during the warm regime fluctuates in the range of 76 to 96% and during the cooling episodes only fluctuates within the 91 to 95% range, with a decreasing trend. The variability in the relative humidity near the surface during the warm and moist regime occurs simultaneously to the large fluctuations in the evaporation rate. The high relative humidity at the surface layer during the cooled regime induces a reduced mean evaporation rate (see center panel of Fig. 5.6). The relative humidity at 750 mb is at 60%

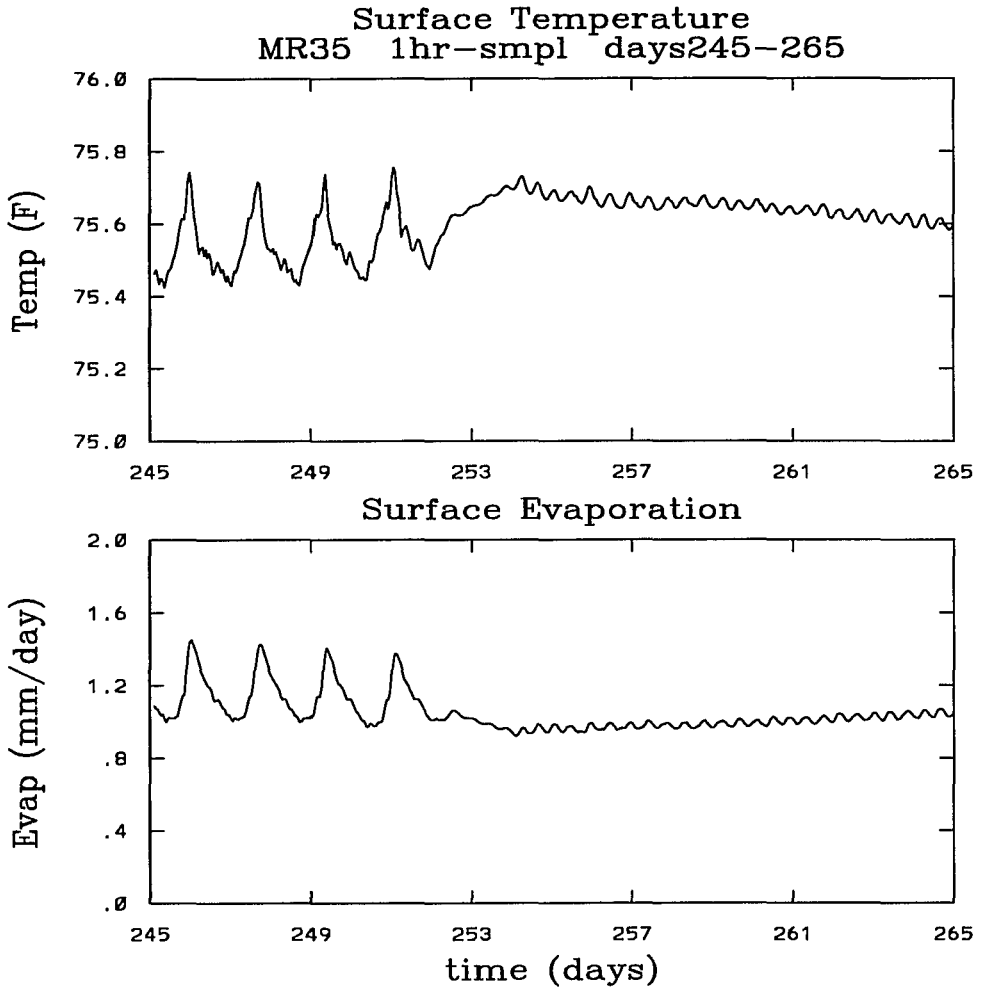

Figure 5.5 – Surface air temperature and evaporation during a transition between regimes.

during the warm regime, but reduces to about 35% in the colder regime (see bottom panel of Fig. 5.6). With a smaller evaporation, and consequently a reduced latent heating rate of the lower troposphere, during the fast cooling phase, it can be concluded that the moderately strong convective activity that depletes the moisture from the column is not solely forced by thermal instabilities in the lowest layers (see top panel of Fig. 3.31).

The next two layers, which could be called the middle troposphere, served as buffer layers for the dynamics of the upper atmosphere as they react to the lower troposphere's events. Whenever the convective activity extend to the second buffer layer the upper troposphere warms

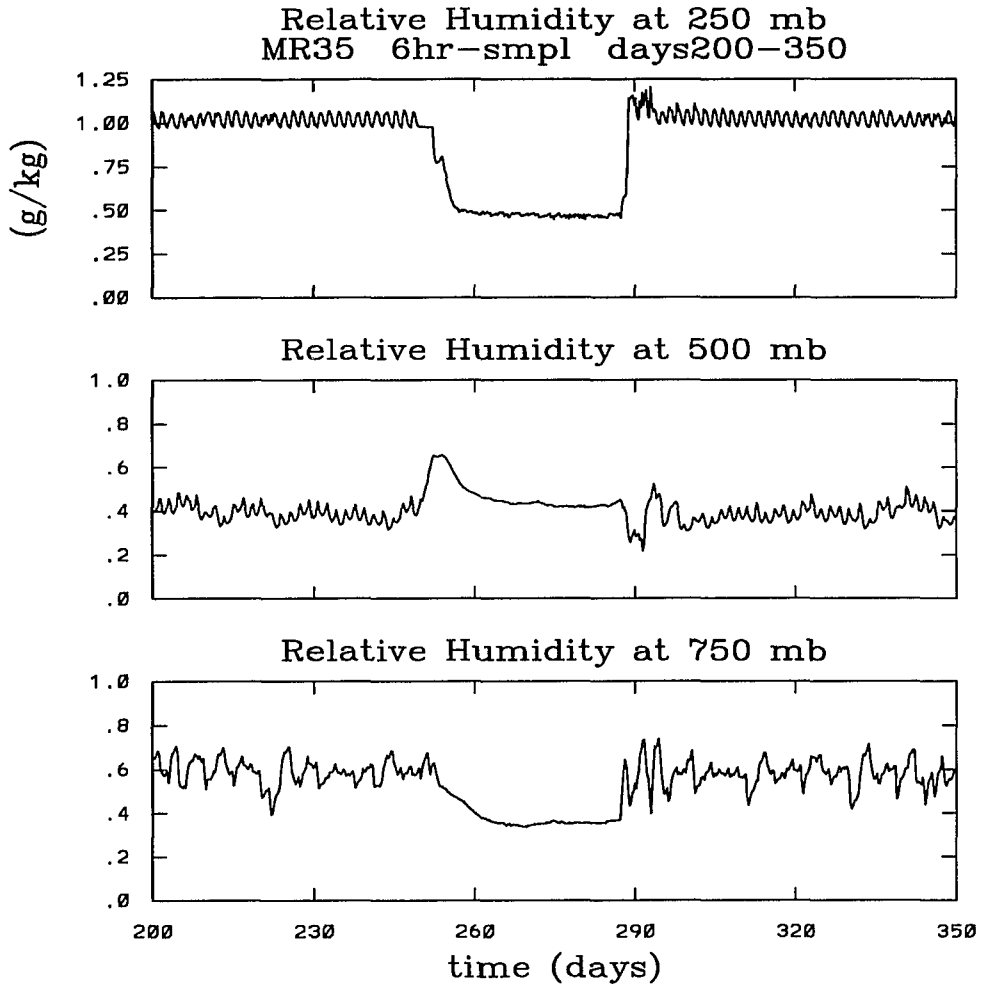

Figure 5.6 – Relative humidity in middle layers for MR35.

up by means of the released latent heat. In the absence of the mean vertical motion forced by convergence and because of its dryness, the upper troposphere slowly warms up by means of a convectively forced exchange of thermal energy and moisture, and with time scales of about 10 to 20 days. The layers 2 and 3 occupy from 800 to 400 mb. In a real atmosphere these layers have the maximum vertical velocities and the largest radiative heating terms. The net heating for these layers is mostly determined by the LWR, and by the latent heat released from the convective activity.

The relative humidity at 500 mb (as in the center panel of Fig. 5.6) has rather low values

in the range of 35 to 50% during the warm regime, that increased to about 65% just before the transitions, and then decreases monotonically to 45% during the cool and dry regime. Two features deserve careful attention: (i) the middle troposphere is essentially dry always, but during the cool regime it gains a slightly larger amount of water vapor; (ii) there is a sudden increase in the relative humidity after the slow build up phase of the warm regime. This sudden increase in the relative humidity is a similar feature to the sudden increase in the water vapor areal density, also, just before the strong cooling phase. It can be inferred from this similarity and from the increase in water vapor at 500 mb that the moisture loading process at the middle and upper troposphere is strongly related to the transition between regimes. These layers are the most likely place to look for radiative interactions not commonly occuring in the warm regime.

The two layers between 400 and 100 mb are radiatively dominated. The amount of water vapor in these layers is 1 g per kg of dry air or less, but significantly enhanced the absorption of both the incoming solar radiation and the infrared radiation emitted by the surface. The increased precipitable water in the upper midtroposphere during the end of the warm regime begins a positive feedback with the SWR (see top and bottom panels of Fig. 5.3). The net heating rate is strongly dependent upon the SWR heating rate in the upper troposphere. The "daily" increases in the specific humidity due to an enhanced temperature, and in the temperature due to an enhanced absorption of SWR are rather small, because the convection quickly depleted the water vapor and neutralized the local thermal instabilities of the upper part of the column. The slow net buildup in the column's specific humidity results in cloud formation in the upper midtroposphere and in a reduction of the SWR heating in the middle troposphere. An upper midtroposphere loaded with water vapor and cooled at a higher rate than the layer directly below it produce an unstable local lapse rate and, consequently, overturning. The released latent heat from the convection produce an unstable lapse rate with respect to the upper tropospheric layer, and the upward propagation of the convective perturbation. The column starts the drying episode from the top down, as opposed to the warm regime's convective episodes that transport

moisture from the bottom up. This is how the transition to the colder regime is triggered.

The relative humidity at 250 mb during the cool regime (see top of Fig. 5.6) decreases to 40%, from the nearly fully saturated warm regime. The loss of water vapor mass is very small, but the relative differences in the specific humidity at this level are very large. Notice that the initial transitional reduction in the relative humidity at 250 mb is followed by a small increase, and then by a further reduction. The small increase is induced by the overturning of contiguous layers at the start of the drying episode. In the real atmosphere there are important effects due to cirrus clouds, like the increase in the albedo or the trapping of the outgoing LWR, but that are not included in this model, and may cause similar effects. The cirrus clouds would be formed when moisture rise above the freezing level in the presence of a vertical shear of the horizontal wind, and tend to remain suspended for a long period of time. The absence of ice clouds and its radiative and thermodynamical implications is one of the limitations of this model.

Only the upper layers above 250 mb show a reduced net radiative heating rate during the fast cooling phase. The convective clouds with small cross sectional area extend to higher levels during the cool regime, but in the dry upper troposphere the absorption of SWR is drastically reduced (see top and bottom panels of Fig. 5.3). This in turn, favors the overturning in the column, and a drier middle simulated troposphere. The net radiative heating rate for the layers below 350 mb is higher during the cool regime.

There is no stratiform precipitation during the cool regime because the layers in the column are unsaturated. The only sink for the moisture at any level is the convective precipitation. During this regime the clouds extend to higher levels because of the local instability at both the lowest and the highest levels (i.e., the moist static energy for a cooled upper troposphere is similar in magnitude to the available moist static energy at the surface). Hence, the overturning of the layers throughout the column is induced by a cascade cooling from the upper layers, rather than by the successive warming of the layers from below.

The water vapor areal density is reduced because of both, the reduced surface evaporation

and the convectively precipitating tropospheric column during the cool regime. The water vapor is processed efficiently in the cooler regime, as shown before. A smaller specific humidity at every layer implies a reduced specific heat, which accounts for a larger radiatively induced temperature change by LWR emission. The cooling of sucessive layers from the top down locally changes the lapse rate and induces drying from the top down. The non-vanishing surface evaporation builds up an enhanced moisture profile from the bottom, during the final phase of the cold regime. The moistening of the layers from the bottom up allows: (i) a better absorption of SWR in the upper layers, but a reduction in the SWR reaching the lower layers; (ii) an increase in the specific heat. The initial warming up or recovery phase is faster than the initial cooling phase because of the lower specific heat for dry air. As the layers gain water vapor the thermal response of the lower troposphere become sluggish.

Chapter 6.

Conclusions

The phenomena discussed in the previous chapters is a class of atmospheric fluctuations that modulate the simulated convective activity within this 1D version of the GLA-AGCM. With warm oceanic temperature and low surface evaporation conditions, the modelled system tends to reside for a longer period of time on a regime where most of the convective activity takes place in the lowest troposphere, with occasional outbursts of deep convection, causing intense precipitation events. This is identified as a warmer and moistier regime. The top of the troposphere seems to be closer to saturation at all times during the warm regime, but not the entire upper middle troposphere. Moisture loading is achieved by lower middle tropospheric convection. As the upper middle troposphere moistens, radiative interactions (of both LWR and SWR wavelengths) with the water vapor induce a transition to a different regime: one in which the entire column of the simulated atmosphere is convectively active for a longer period of time. The troposphere, although convectively active in its entirety, does not produce intense precipitation events as before, but a moderate and sustained convectively precipitating regime. Rain evaporation accounts for the absence of heavy rainfall. The transitions are characterized by temperature changes that are in phase for all layers. In that sense, these transitions to a different convective regime are similar to the vertically uniform temperature transition identified

in Madden and Julian [1971,1972] for the intraseasonal oscillations. However, within the context of the current work, it is not possible to identify the associated pressure and wind modulations refered to in their work. For these numerical experiments the temperature fluctuations induce the sustained convective precipitation phase. The entire column looses moisture during this new convective regime, and also because of a slightly reduced surface evaporation. During the warmer regime the middle troposphere, at about 500 mb, has a minimum amplitude for the specific humidity fluctuations. In the colder regime, specific humidity fluctuations are still small at 500 mb, but the relative humidity is larger than for the moist regime, due to a combined effect between the reduction in the layer's temperature and the evaporation of the precipitate from the upper layers. Spectral analysis of the time series for the potential temperature and the specific humidity at 250 mb reveal broad spectral peaks centered about 1.77, 55, 83, and 150 days, although only the first one is above the corresponding 95% confidence level of the red noise curve. Nearby the surface (950 mb) the spectral analysis reveals very weak peaks centered at about 15 days, and the very strong signal at 1.75 days.

As seen in chapter 3, for the case of a higher surface evaporation, the simulated system oscillates between two convective regimes whose surface signature (i.e., temperature, precipitation and evaporation) is similar to the convective regimes of the low evaporation cases. The regimes now have similar residence times, although the colder regime appears to be longer lived. The time series seem to indicate fluctuations in the time scales of 20 to 50 days between the regimes, but the spectral analysis does not reveal clearly the predominance of such time scales. The temperature fluctuations are in phase for all the layers, too. The specific humidity fluctuations for this rather moist simulated atmosphere have a nodal point at about 500 mb.

The fundamental time scales for the convective adjustment of the column seem to be independent of other cyclic forcings, like the diurnal and seasonal cycles of the solar insolation at the top of the model atmosphere. This convective adjustment time for the low surface evaporation case is about 42 hours, and a broad band peak in the 1–1.44 days range for the high evaporation case. The typical vertical structure of the regimes seem independent of the presence of a cyclic

solar forcing, but not the phase of the transitions between regimes.

Qualitatively, at least, the transitions between regimes for this simulated tropical oceanic atmosphere are similar to the characteristics identified in chapter 1 for the stationary enhancement of the intraseasonal oscillations in the real atmosphere. It is not implied that the two phenomena are the same because there are important differences. Among these are the known Northern Winter intensification of the Madden-Julian oscillations, the upper air wind signature, the pressure variations, and other features not treated in this work. Other numerical experiments might be of interest: to include a more interactive oceanic surface in terms of its temperature and moisture flux; a horizontal mass convergence scheme that is responsive to the pressure variations induced in the column by the temperature fluctuations; a finer vertical grid with a more complete description of radiative interactions; and, finally, a prescribed horizontal moisture convergence profile. If the transitions between regimes for such also idealized experiments were to remain within the proper time scales and with similar vertical structure as the present simulations, then it might be asserted that the observed localized enhancement of the intraseasonal phenomena, and these simulated fluctuations between regimes correspond to a similar class of atmospheric variabilities.

From the current simulations, it is seen that a warm surface with enhanced evaporation induces a fully convectively active column, that tends to reduce the surface input of moisture. The use of an interactive surface evaporation and a horizontal moisture convergence profile can identify whether the time scales for these intraseasonal variabilities are dependent upon the surface availability of moisture (and the resultant lower middle troposphere warming), or on the precipitable water at the upper middle troposphere. The use of a horizontal mass convergence scheme, with interactive pressure variations, can help clarify whether the fully active column can be triggered even in the absence of a saturated troposphere, and with the proper time scales. The use of a finer vertical grid could provide for a better description of the vertical structure of the transitions. The author intends to pursue each one of these areas of research, as well as to look for a validation or rejection of the hypothesized mechanisms for stationary

enhancement of intraseasonal variability with current atmospheric measurements datasets, to improve his understanding of tropical climate variability.

References

This list of references includes those that are specifically mentioned in the text, as well as some others that served to clarify ideas and the interpretation of the results, although not explicitly refered to.

Albright, M.D.; D.R. Mock; E.E. Recker; R.J. Reed, 1981: A Diagnostic Study of the Diurnal Rainfall Variation in the GATE B-Scale Area. *J.Atmos.Sci.,* **38** 1429–45.

Albright, M.D.; E.E. Recker; R.J. Reed; R. Dang, 1985: The Diurnal Variation of Deep Convection and Inferred Precipitation in the Central Tropical Pacific During January-February 1979. *Mon.Wea.Rev.,* **113** 1663–80.

Anderson, John R.; Duane E. Stevens, 1987: The Response of the Tropical Atmosphere to Low Frequency Thermal Forcing. *J.Atmos.Sci.,* **44** 676–86.

Anthes, R.A., 1977: A Cumulus Parameterization Scheme Utilizing a One-Dimensional Cloud Model. *Mon.Wea.Rev.,* **105** 270–86.

Arakawa, Akio, 1966: Computational Design for Long-Term Numerical Integration of the Equations of Fluid Motion: Two Dimensional Incompressible Flow (Part I). *J. of Comp. Phys.,* **1** 119–43.

Arakawa, A.; A. Katayama; Y. Mintz, 1969: Numerical Simulation of the General Circulation of the Atmosphere. *Proceedings of the WMO/IUGG Symposium on Numerical Weather Prediction in Tokyo, Nov. 26–Dec. 4,1968* (edited by J.M.A.). Tokyo: Japan Meteorological Agency, IV 7.

Arakawa, A., 1972: *Design of the UCLA GCM: Numerical Simulation of Weather and Climate* . Dept. of Meteorology, UCLA, Los Angeles, CA: Tech. Rep. No. 7, 116pp.

Arakawa, Akio; Wayne H. Schubert, 1974: Interaction of a Cumulus Cloud Ensemble with the Large-Scale Environment, Part I. *J.Atmos.Sci.,* **31** 674–701.

Arakawa, A.; Vivian R. Lamb, 1977: Computational Aspects of Numerical Models for Weather Prediction and Climate Simulation. *Methods in Computational Physics, Vol. 17* (edited by Julius Chang). New York: Academic Press, 173–265.

Arakawa, A.; M.J. Suarez, 1983: Vertical Differencing of the Primitive Equations in Sigma Coordinates. *Mon.Wea.Rev.*, **111** 34–55.

Arakawa, A.; Jeng-Ming Chen, 1986: Closure Assumptions in the Cumulus Parameterization Problem. *Collection of Papers Presented at the WMO/IUGG Symposium on Numerical Weather Prediction in Tokyo, August 4–8,1986* (edited by J.M.A.). Tokyo: Japan Meteorological Agency, 107–31.

Bath, L.M.; M.A. Dias; D.L. Williamson; G.S. Williamson; R.J. Wolski, 1987: *Documentation of NCAR CCM1 Program Modules* . Boulder, Colorado: NCAR Tech. Note TN-287+IA, 307pp.

Baumgartner, Albert; Eberhard Reichel, 1975: *The World Water Balance: Mean Annual Global, Continental and Maritime Precipitation, Evaporation and Run-off* . New York: Elsevier Scientific Publishing Co., 179pp.

Bjerknes, J., 1969: Atmospheric Teleconnections from the Equatorial Pacific. *Mon.Wea.Rev.*, **97** 163–72.

Carlson, G.C.; S. Hastenrath, 1970: Diurnal Variation of Wind, Pressure, and Temperature in the Troposphere and Stratosphere over Eniwetok. *Mon.Wea.Rev.*, **98** 408–16.

Cheng, M.-D., 1989a: Effects of downdrafts and mesoscale convective organization on the heat and moisture budgets of tropical cloud clusters. Part I: A diagnostic cumulus ensemble model. *J.Atmos.Sci.*, **46** 1517–38.

Cheng, M.-D., 1989b: Effects of downdrafts and mesoscale convective organization on the heat and moisture budgets of tropical cloud clusters. Part II: Effects of convective-scale downdrafts. *J.Atmos.Sci.*, **46** 1540–64.

Chou, Ming-Dah; Albert Arking, 1980: Computation of Infrared Cooling Rates in the Water Vapor Bands. *J.Atmos.Sci.*, **37** 855-67.

Chou, M.-D., 1984: Broadband Water Vapor Transmission Functions for Atmospheric IR FLux Computations. *J.Atmos.Sci.*, **41** 1775–78.

Chu, P.C.; R.W. Garwood; P. Muller, 1990: Unstable and damped modes in coupled ocean mixed layer and cloud models. *J.Marine Systems*, **1** 1–11.

Cullen, M.J.P., 1983: Current Progress and Prospects in Numerical Techniques for Weather Prediction Models. *J. of Comp. Phys.*, **50** 1–37.

Dahlquist, G.; A. Bjorck, 1974: *Numerical Methods* . Englewood Cliffs, NJ: Prentice-Hall, 589pp.

Davies, R., 1982: *Documentation of the solar radiation parameterization in the GLAS climate model* . NASA Tech. Memo 83961, 57pp.

Deardorff, J.W., 1972: Parameterization of the Planetary Boundary Layer for Use in a GCM. *Mon.Wea.Rev.*, **100** 93–106.

DelGenio, A.A.; A.A. Lacis; R.A. Ruedy, 1991: Simulations of the effect of a warmer climate on atmospheric humidity. *Nature,* **351** 382–4.

Fingerhut, W.A., 1978: A Numerical Model of a Diurnally Varying Tropical Cloud Cluster Disturbance. *Mon.Wea.Rev.,* **106** 255–67.

Foltz, G.S.; W.M. Gray, 1979: Diurnal Variation in the Troposphere's Energy Balance . *J.Atmos.Sci.,* **36** 1450–66.

Gage, K.S.; G.C. Reid, 1982: Coherent Annual and Interannual Variations in Temperature and Height Fields in the Tropical Troposphere and Lower Stratosphere. *Geophys.Res.Lett.,* **9** 1199–201.

Geisler, J.E.; E.J. Pitcher, 1988: On the Representation of the 40–50 Day Oscillation in Terms of Velocity Potential and Streamfunction. *J.Atmos.Sci.,* **45** 1850–4.

Gentle, James; William Sallas (statistics designers), 1991: Time Series Analysis and Forecasting. *User's Manual: FORTRAN subroutines for statistical analysis, Version 2.0* (edited by David Wilson). IMSL, Inc., Customer Relations, 2500 Permian Tower, 2500 City West Boulevard, Houston, Texas 77042–3020, Ch. 8, pages 661–838.

Gray, W.M.; R.W. Jacobson, 1977: Diurnal Variation of Deep Cumulus Convection . *Mon.Wea.Rev.,* **105** 1171–88.

Gruber, A., 1976: An Estimate of the Daily Variation of Cloudiness Over the GATE A/B Area. *Mon.Wea.Rev.,* **104** 1036–9.

Haltiner, G.J.; R.T. Williams, 1980: *Numerical Prediction and Dynamic Meteorology, 2nd edition* . N.Y.: John Wiley & Sons, 477pp.

Harris, M.F.; F.G. Finger; S. Teweles, 1962: Diurnal Variation of Wind, Pressure, and Temperature in the Troposphere and Stratosphere over the Azores. *J.Atmos.Sci.,* **19** 136–49.

Harshvardhan; T.G. Corsetti, 1984: *Longwave radiation parameterization for the UCLA/GLAS GCM* . NASA Tech. Memo 86072, 51pp.

Harshvardhan; D.A. Randall, 1985: Comments on "The Parameterization of Radiation for Numerical Weather Prediction and Climate Models". *Mon.Wea.Rev.,* **113** 1832–33.

Harshvardhan; R. Davies; D.A. Randall; T.G. Corsetti, 1987: A Fast Radiation Parameterization for Atmospheric Circulation Models. *J.Geophys.Res.-D,* **92** 1009–16.

Hastenrath, S., 1972: Daily wind, pressure and temperature variation up to 30 Km over the tropical western Pacific. *Quart.J.Roy.Meteor.Soc.,* **98** 48–59.

Hastenrath, S.; P.J. Lamb, 1979: *Climatic Atlas of the Indian Ocean, Part 2: The Oceanic Heat Budget* . Madison, WI: The University of Wisconsin Press, 1-2.

Hastenrath, 1991: *Climate Dynamics of the Tropics* . Vol. 8 of the Atm. Sc. Lib., 488pp.

Hayashi, Y.; D.G. Golder, 1986: Tropical Intraseasonal Oscillations Appearing in a GFDL General Circulation Model and FGGE Data. Part I: Phase Propagation. *J.Atmos.Sci.*, **43** 3058–67.

Helfand, H.M., 1985: A new scheme for the parameterization of the turbulent planetary boundary layer in the GLAS Fourth Order GCM. *7th Conference on Numerical Weather Prediction, June 17–20, 1985, Montreal, Canada* (edited by A.M.S.). Boston, MA: American Meteorological Society, 348–54.

Helfand, H.M.; J.C. Labraga, 1988: Design of a Nonsingular Level 2.5 Second Order Closure Model for the Prediction of Atmospheric Turbulence. *J.Atmos.Sci.*, **45** 113–32.

Hendon, Harry H., 1986: Streamfunction and Velocity Potential Representation of Equatorially Trapped Waves. *J.Atmos.Sci.*, **43** 3038–42.

Hendon, H.H.; Brant Liebmann, 1990: The Intraseasonal (30–50 day) Oscillation of the Australian Summer Monsoon. *J.Atmos.Sci.*, **47** 2909–23.

Heymsfield, A.J.; L.M. Miloshevich, 1991: Limit to greenhouse warming?. *Nature*, **351** 14–5.

Hildebrand, F.B., 1974, 2nd edition: *Introduction to Numerical Analysis* . New York: McGraw-Hill Book Company, 669pp.

Hildebrand, F.B., 1968: *Finite Difference Equations and Simulations* . Englewood Cliffs, NJ: Prentice-Hall, 335pp.

Holton, J.R.; R.S. Lindzen, 1968: A Note on "Kelvin" Waves in the Atmosphere. *Mon.Wea.Rev.*, **96** 385–6.

Hsu, H.H.; B.J. Hoskins; F.F. Jin, 1990: The 1985/86 Intraseasonal Oscillation and the Role of the Extratropics. *J.Atmos.Sci.*, **47** 823–39.

Hu, Qi; D.A. Randall, 1991a: Low Frequency Oscillations in Radiative-Convective Models. *19th Conference on Hurricanes and Tropical Meteorology, May 6–10, 1991, Miami, Florida* (edited by A.M.S.). Boston, MA: American Meteorological Society, 33–35.

Hu, Qi; D.A. Randall, 1991b: Low Frequency Oscillations in Radiative-Convective Models. *Fifth Conference on Climate Variations, Oct. 14–18, 1991* (edited by A.M.S.). Boston, MA: American Meteorological Society, 218–25.

Iribarne, J.V.; W.L. Godson, 1981: *Atmospheric Thermodynamics, 2nd edition* . Dordrecht, Holland: D.Reidel Publ. Co., 222pp.

Itoh, Hisanori; Michael Ghil, 1988: The Generation Mechanism of Mixed Rossby-Gravity Waves in the Equatorial Troposphere. *J.Atmos.Sci.*, **45** 585–604.

Johnson, D.H., 1955: Tidal oscillations in the lower stratosphere. *Quart.J.Roy.Meteor.Soc.*, **81** 1–8.

Kasahara, A., 1977: Computational Aspects of Numerical Models for Weather Prediction and Climate Simulation. *Methods in Computational Physics, Vol. 17* (edited by Julius Chang). New York: Academic Press, 2–66.

King, Michael D.; Harshvardhan, 1986: Comparative Accuracy of Selected Multiple Scattering Approximations. *J.Atmos.Sci.,* **43** 784–801.

Knuth, Donald E., 1990: *The TeXbook* . Reading, MA: Addison-Wesley Publ. Co., 483pp.

Knutson, Thomas R.; Klaus M. Weickmann, 1987: 30–60 Day Atmospheric Oscillations: Composite Life Cycles of Convection and Circulation Anomalies. *Mon.Wea.Rev.,* **115** 1407–36.

Kuo, H.L., 1965: On Formation and Intensification of Tropical Cyclones Through Latent Heat Release by Cumulus Convection. *J.Atmos.Sci.,* **22** 40–63.

Lacis, Andrew A.; James E. Hansen, 1974: A Parameterization for the Absorption of Solar Radiation in the Earth's Atmosphere. *J.Atmos.Sci.,* **31** 118–33.

Lau, K.-M.; P.H. Chan, 1985: Aspects of the 40–50 Day Oscillation during the Northern Winter as Inferred from Outgoing Longwave Radiation. *Mon.Wea.Rev.,* **113** 1889–909.

Lau, K.-M.; P.H. Chan, 1986: Aspects of the 40–50 Day Oscillation during the Northern Summer as Inferred from Outgoing Longwave Radiation. *Mon.Wea.Rev.,* **114** 1354–67.

Lau, K.-M.; L.Peng, 1987: Origin of Low-Frequency (Intraseasonal) Oscillations in the Tropical Atmosphere, Part I: Basic Theory. *J.Atmos.Sci.,* **44** 950–72.

Lau, K.-M.; S. Shen, 1988: On the Dynamics of Intraseasonal Oscillations and ENSO. *J.Atmos.Sci.,* **45** 1781–97.

Lau, K.-M.; L. Peng, 1990: Origin of Low Frequency (Intraseasonal) Oscillations in the Tropical Atmosphere. Part III: Monsoon Dynamics. *J.Atmos.Sci.,* **47** 1443–62.

Lau, K.-M.; T. Nakazawa; C.H. Sui, 1991: Observations of Cloud Cluster Hierarchies Over the Tropical Western Pacific. *J.Geophys.Res.-D,* **96** 3197–208.

Levitus, Sydney, 1984: Annual Cycle of Temperature and Heat Storage in the World Ocean. *J.Phys.Oceanography,* **14** 727–46.

List, Robert J. (editor), 1984: *Smithsonian Meteorological Tables, 6th revision* . Washington, D.C.: Smithsonian Institution Press, pages 488–520.

Lord, S.J.; A. Arakawa, 1980: Interaction of a Cumulus Cloud Ensemble with the Large-Scale Environment, Part II. *J.Atmos.Sci.,* **37** 2677–92.

Lord, S.J., 1982: Interaction of a Cumulus Cloud Ensemble with the Large-Scale Environment. Part III: Semi-Prognostic Test of the Arakawa-Schubert Parameterization. *J.Atmos.Sci.,* **39** 88–103.

Lord, S.J.; W.C. Chao; A. Arakawa, 1982: The Interaction of a Cumulus Cloud Ensemble with the Large-Scale Environment, Part IV: The Discrete Model. *J.Atmos.Sci.*, **39** 104–13.

Lorenz, Edward N., 1965: On the Possible Reasons for Long-Period Fluctuations of the General Circulation. *WMO-IUGG Symposium on Research and Development Aspects of Long Range Weather Forecasting, Boulder, Colorado, 1964* (edited by W.M.O.). Geneva, Switzerland: World Meteorological Organization, Technical Note No. 66, 203–11.

Madden, R.A.; P.R. Julian, 1971: Detection of a 40–50 Day Oscillation in the Zonal Wind in the Tropical Pacific. *J.Atmos.Sci.*, **28** 702-8.

Madden, Roland A.; Paul R. Julian, 1972: Description of Global-Scale Circulation Cells in the Tropics with a 40–50 Day Period. *J.Atmos.Sci.*, **29** 1109–23.

Manabe, Syukuro; Joseph Smagorinsky; Robert F. Strickler, 1965: Simulated Climatology of a General Circulation Model with a Hydrologic Cycle. *Mon.Wea.Rev.*, **93** 769–98.

McBride, J.L.; W.M. Gray, 1980a: Mass divergence in tropical weather systems. Paper I: Diurnal variation. *Quart.J.Roy.Meteor.Soc.*, **106** 501–16.

McBride, J.L.; W.M. Gray, 1980b: Mass divergence in tropical weather systems. Paper II: Large-scale controls on convection. *Quart.J.Roy.Meteor.Soc.*, **106** 517–38.

McDonald, A.; J.R. Bates, 1989: Semi-Lagrangian Integration of a Gridpoint Shallow Water Model on the Sphere. *Mon.Wea.Rev.*, **117** 130–7.

McGarry, M.M.; R.J. Reed, 1978: Diurnal Variations in Convective Activity and Precipitation During Phases II and III of GATE. *Mon.Wea.Rev.*, **106** 101–13.

Mellor, G.L.; T. Yamada, 1974: A Hierarchy of Turbulence Closure Models for Planetary Boundary Layers. *J.Atmos.Sci.*, **31** 1791–806.

Mellor, G.L.; T. Yamada, 1982: Development of a turbulence closure model for geophysical fluid problems. *Rev.Geophys.Space Phys.*, **20** 851–75.

Mitchell, J.M.; B. Ozerdzeevskii; H. Floha; W.L. Hefmyer; H.H. Lamb; K.N. Rao; C.C. Wallén, 1966: The Power Spectrum and General Principles of its Application to the Evaluation of Non-randomness in Climatological Series. *Climate Change* (edited by W.M.O.). World Meteorological Organization, Tech. Note. No. 79, 33–75.

Mitchell, Todd P., 1990: *The Annual March of Convection, Sea Surface Temperature, and Surface Winds in the Tropics* . Ph.D. Thesis, Department of Atmospheric Sciences, University of Washington, Seattle, WA 98195, 59–68.

Neelin, J.D.; I.M. Held; K.H. Cook, 1987: Evaporation-Wind Feedback and Low-Frequency Variability in the Tropical Atmosphere. *J.Atmos.Sci.*, **44** 2341–48.

Neumann, G.; W. J. Pierson, Jr., 1966: *Principles of Physical Oceanography* . Englewood Cliffs, NJ: Prentice-Hall, Inc., 234–68, 422–78.

Niita, T.; S. Esbensen, 1974: Diurnal Variations in the Western Atlantic Trades during the BOMEX. *J.Meteor.Soc.Japan,* **52** 254–7.

Ooyama, K., 1971: A theory on parameterization of cumulus convection. *J.Meteor.Soc.Japan,* **39** 744–56.

Parker, Sybil P., 1988: *Meteorology Source Book* . New York: McGraw-Hill, 304pp.

Pedlosky, Joseph, 1987, 2nd ed.: *Geophysical Fluid Dynamics* . New York: Springer-Verlag, 710pp.

Peixoto, José P.; Abraham H. Oort, 1992: *Physics of Climate* . New York: American Institute of Physics, 176–206.

Press, W.H.; B.P. Flannery; S.A. Teukolsky; W.T. Vetterling, 1989: *Numerical Recipes: The Art of Scientific Computing* . Cambridge, MA: Cambridge Univ. Press, 839pp.

Ramanathan, V.; W. Collins, 1991: Thermodynamic regulation of ocean warming by cirrus clouds deduced from observations of the 1987 El Niño. *Nature,* **351** 27–32.

Rancic, M., 1988: Fourth Order Horizontal Advection Schemes on the Semi-Staggered Grid. *Mon.Wea.Rev.,* **116** 1274–88.

Randall, D.A.; J.A. Abeles; T.G. Corsetti, 1985: Seasonal Simulations of the Planetary Boundary Layer and the Boundary Layer Stratocumulus Clouds with a GCM. *J.Atmos.Sci.,* **42** 641–76.

Randall, D.A.; Harshvardhan; D.A. Dazlich, 1991: Diurnal Variability of the Hydrologic Cycle in a General Circulation Model. *J.Atmos.Sci.,* **48** 40–62.

Raval, A.; V. Ramanathan, 1989: Observational determination of the greenhouse effect. *Nature,* **342** 758–61.

Reed, R.J.; K.D. Jaffe, 1981: Diurnal Variation of Summer Convection Over West Africa and the Tropical Eastern Atlantic During 1974 and 1978. *Mon.Wea.Rev.,* **109** 2527–34.

Ridgway, W.L.; Harshvardhan; A. Arking, 1991: Computation of Atmospheric Cooling Rates by Exact and Approximate Methods. *J.Geophys.Res.-D,* **96** 8969–84.

Riehl, H., 1954: *Tropical Meteorology* . New York: McGraw-Hill Book Company, 392pp.

Ritchie, H., 1988: Application of the Semi-Lagrangian Method to a Spectral Model of the Shallow Water Equations. *Mon.Wea.Rev.,* **116** 1587–98.

Robert, A.; T.L. Yee; H. Ritchie, 1985: A Semi-Lagrangian and Semi-Implicit Numerical Integration Scheme for Multilevel Atmospheric Models. *Mon.Wea.Rev.,* **113** 388–94.

Ruprecht, E.; W.M. Gray, 1976a: Analysis of satellite-observed tropical cloud clusters: I. Wind and dynamic fields. *Tellus,* **28** 391–413.

Ruprecht, E.; W.M. Gray, 1976b: Analysis of satellite-observed tropical cloud clusters: II. Thermal, moisture and precipitation. *Tellus,* **28** 414–26.

Satoh, M.; Y.-Y. Hayashi, 1992: Simple Cumulus Models in One-Dimensional Radiative Convective Equilibrium Problems. *J.Atmos.Sci.,* **49** 1202–20.

Sommerville, R.C.J.; P.H. Stone; M. Halem; J.E. Hansen; J.S. Hogan; L.M. Druyan; G. Russell; A.A. Lacis; W.J. Quirk; J. Tenenbaum, 1974: The GISS Model of the Global Atmosphere. *J.Atmos.Sci.,* **31** 84–117.

Stephens, Graeme L.; T. J. Greenwald, 1991a: The Earth's Radiation Budget and Its Relation to Atmospheric Hydrology 1. Observations of the Clear Sky Greenhouse Effect. *J.Geophys.Res.-D,* **96** 15311–24.

Stephens, Graeme L.; T. J. Greenwald, 1991b: The Earth's Radiation Budget and Its Relation to Atmospheric Hydrology 2. Observations of Cloud Effects. *J.Geophys.Res.-D,* **96** 15325–40.

Sud, Y.; A. Molod, 1988: Cloud-Radiation Feedback Processes and the Influence of Recent Improvements in the Parameterization of Convection in the GLA GCM. *Mon.Wea.Rev.,* **116** 2366–87.

Sui, C.-H.; K.-M. Lau, 1989: Origin of Low-Frequency (Intraseasonal) Oscillations in the Tropical Atmosphere. Part II: Structure and Propagation of Mobile Wave-CISK Modes and Their Modification by Lower Boundary Forcings. *J.Atmos.Sci.,* **46** 37–56.

Swinbank, R.; T.N. Palmer; M.K. Davey, 1988: Numerical Simulations of the Madden and Julian Oscillation. *J.Atmos.Sci.,* **45** 774–88.

Wallace, J.M.; F.R. Hartranft, 1969: Diurnal Wind Variations, Surface to 30 kilometers . *Mon.Wea.Rev.,* **97** 446–55.

Weickmann, Klaus M.; Glenn R. Lussky; John E. Kutzbach, 1985: Intraseasonal (30–60 Day) Fluctuations of Outgoing Longwave Radiation and 250 mb Streamfunction during Northern Winter. *Mon.Wea.Rev.,* **113** 941–61.

Williamson, D.L.; J.T. Kiehl; V. Ramanathan; R.E. Dickinson; J.J. Hack, 1987: *Description of NCAR Community Climate Model (CCM1)* . Boulder, Colorado: NCAR Tech. Note TN-285+STR, 112pp.

Yamada, T., 1977: A numerical experiment in pollutant dispersion in a horizontally-homogeneous atmospheric boundary layer. *Atmos.Environ.,* **11** 1015–24.

Yanai, Michio; Steven Esbensen; Jan-Hwa Chu, 1973: Determination of Bulk Properties of Tropical Cloud Clusters from Large-Scale Heat and Moisture Budgets. *J.Atmos.Sci.,* **30** 611–27.

Yasunari, Tetsuzo, 1979: Cloudiness Fluctuations Associated with the Northern Hemisphere Summer Monsoon. *J.Meteor.Soc.Japan,* **57** 227–42.

Yasunari, T., 1980: A Quasi-Stationary Appearance of 30 to 40 Day Period in the Cloudiness Fluctuations during the Summer Monsoon over India. *J.Meteor.Soc.Japan,* **58** 225–9.

Yasunari, T., 1981: Structure of an Indian Summer Monsoon System with around 40-Day Period. *J.Meteor.Soc.Japan,* **59** 336–54.